Analysis of hydraulic fracture propagation in fractured reservoirs: an improved model for the interaction between induced and natural fractures

Analysis of hydraulic fracture propagation in fractured reservoirs: an improved model for the interaction between induced and natural fractures

by

Arash Dahi Taleghani, B.S.; M.S.

Dissertation

Presented to the Faculty of the Graduate School of
The University of Texas at Austin
in Partial Fulfillment
of the Requirements
for the Degree of

Doctor of Philosophy

The University of Texas at Austin
May 2009

Dedication

To my devoted parents for their endless love and support

ACKNOWLEDGEMENTS

Analysis of hydraulic fracture propagation in fractured reservoirs: an improved model for the interaction between induced and natural fractures

Publication No._____

Arash Dahi Taleghani, PhD

The University of Texas at Austin, 2009

Supervisor: Jon E. Olson

Large volumes of natural gas exist in tight fissured reservoirs. Hydraulic fracturing is one of the main stimulating techniques to enhance recovery from these fractured reservoirs. Although hydraulic fracturing has been used for decades for the stimulation of tight gas reservoirs, a thorough understanding of the interaction between induced hydraulic fractures and natural fractures is still lacking. Recent examples of hydraulic fracture diagnostic data suggest complex, multi-stranded hydraulic fracture

geometry is a common occurrence. The interaction between pre-existing natural fractures and the advancing hydraulic fracture is a key condition leading to complex fracture patterns. Large populations of natural fractures that exist in formations such as the Barnett shale are sealed by precipitated cements which could be quartz, calcite, etc. Even though there is no porosity in the sealed fractures, they may still serve as weak paths for fracture initiation and/or for diverting the path of the growing hydraulic fractures. Performing hydraulic fracture design calculations under these complex conditions requires modeling of fracture intersections and tracking fluid fronts in the network of reactivated fissures. In this dissertation, the effect of the cohesiveness of the sealed natural fractures and the intact rock toughness in hydraulic fracturing are studied. Accordingly, the role of the pre-existing fracture geometry is also investigated. The results provide some explanations for significant differences in hydraulic fracturing in naturally fractured reservoirs from non-fractured reservoirs. For the purpose of this research, an extended finite element method (XFEM) code is developed to simulate fracture propagation, initiation and intersection. The motivation behind applying XFEM are the desire to avoid remeshing in each step of the fracture propagation, being able to consider arbitrary varying geometry of natural fractures and the insensitivity of fracture propagation to mesh geometry. New modifications are introduced into XFEM to improve stress intensity factor calculations, including fracture intersection criteria into the model and improving accuracy of the solution in near crack tip regions.

The presented coupled fluid flow-fracture mechanics simulations extend available modeling efforts and provide a unified framework for evaluating fracture design

parameters and their consequences. Results demonstrate that fracture pattern complexity is strongly controlled by the magnitude of in situ stress anisotropy, the rock toughness, the natural fracture cement strength, and the approach angle of the hydraulic fracture to the natural fracture. Previous studies (mostly based on frictional fault stability analysis) have concentrated on predicting the onset of natural fracture failure. However, the use of fracture mechanics and XFEM makes it possible to evaluate the progression of fracture growth over time as fluid is diverted into the natural fractures.

Analysis shows that the growing hydraulic fracture may exert enough tensile and/or shear stresses on cemented natural fractures that they may be opened or slip in advance of hydraulic fracture tip arrival, while under some conditions, natural fractures will be unaffected by the hydraulic fracture. A threshold is defined for the fracture energy of cements where, for cases below this threshold, hydraulic fractures divert into the natural fractures. The value of this threshold is calculated for different fracture set orientations. Finally, detailed pressure profile and aperture distributions at the intersection between fracture segments show the potential for difficulty in proppant transport under complex fracture propagation conditions.

Whether a hydraulic fracture crosses or is arrested by a pre-existing natural fracture is controlled by shear strength and potential slippage at the fracture intersections, as well as potential debonding of sealed cracks in the near-tip region of a propagating hydraulic fracture. We introduce a new more general criterion for fracture propagation at the intersections. We present a complex hydraulic fracture pattern propagation model

based on the Extended Finite Element Method as a design tool that can be used to

optimize treatment parameters under complex propagation conditions.

Table of Contents

Chapter 4. Hydraulic Fracturing Propagation   114

Chapter 5. Conclusions and Recommendations   163

List of Tables

List of Figures

xviii

Chapter 1. Introduction

1.1. Hydraulic Fracturing

Hydraulic fracturing began in the oil and gas industry during the 1930s when Dow Chemical Company discovered that by applying a large enough downhole fluid pressure, it was possible to deform and fracture the rock formation to have a more effective acid stimulation (Grebe et al. 1935). The first non-acid hydraulic fracturing treatment for well stimulation was introduced in Kansas in 1947 on a gas well in Hugoton field in order to compare the new technique with the available acidization technology (Veatch et al. 1989). At the present time, hydraulic fracturing is extensively used to improve oil and gas wells' productivity. Of the production wells drilled in North America since the 1950s, about 70% of gas wells and 50% of oil wells have been hydraulically fractured (Valko and Economides, 1995). Thousands of treatments are implemented each year in a wide range of geological formations which may vary from low permeability gas fields, weakly consolidated offshore sediments such as those in the Gulf of Mexico, soft coal beds for methane extraction, naturally fractured reservoirs, and geometrically complex structures such as lenticular formations (Adachi et al. 2007).

1

Hydraulic fracturing is a common technique not just for enhancing hydrocarbon production but also geothermal energy extraction (Sasaki, 1998; Berumen et al., 2000). It is widely used for other purposes like hazardous solid waste disposal (Hunt et al., 1994; Hainey et al. 1999), measurement of in-situ stresses (Hayashi et al., 1997; Raaen et al., 2001), fault reactivation in mining (Board et al. 1992) and remediation of soil and ground water aquifers (Murdoch and Slack 2002). Hydraulic fractures which are naturally induced by pressurized fluid in the host rock are also observed in outcrops as joints (Pollard and Aydin, 1988; Lacazette and Engelder, 1992) and veins (Sirivastava and Engelder, 1991), as well as magma-driven dikes (Pollard, 1987; Rubin, 1995). Primary oil migration may also happen through buoyancy-driven fracture propagation through a phenomenon very similar to hydraulic fracturing (Jin and Johnson, 2008).

A hydraulic fracture is induced in two phases (Weijers, 1995). It starts with perforating the casing and creating finger-like holes or weak points in the formation. Then a viscous fluid called a "pad" is pumped into the well. When the downhole pressure goes beyond "breakdown pressure," a fracture initiates from the perforated interval and grows into the surrounding rock (reservoir). In the second phase, a slurry of fluid mixed with sorted sand (proppant) is injected. This slurry extends the initiated fracture and transports the proppant deep into the fracture. After the materials are pumped in, the fluid chemically breaks back to a lower viscosity mixture and flows back out of the well, leaving a highly conductive propped path for the flow of oil/gas to the wellbore (Veatch et al., 1989). This high permeability pathway is narrow, but can be extremely long. Typical widths of a hydraulic fracture are on the order of 0.25 in. (or less), while the

effective length may be 3000 feet tip to tip (Economides et al., 1993). The whole treatment may take place on a time-scale of tens of minutes to a few hours, depending upon the designed fracture size and volume of proppant to be placed. A successful treatment may increase the production up to 10s of times, making the technique economically attractive. A hydraulic fracture will grow in the direction normal to the smallest of the three principal stresses as it tends to open in the direction of least resistance. For most reservoir depths of interest in the petroleum industry, the smallest principal stress is in the horizontal plane, which restricts fractures to the vertical plane. Therefore, one may map fractures on the horizontal plane. However, an ideal model should include the three-dimensional aspects of the problem, the available techniques in the literature for three-dimensional analysis of fractures (for instance Rungamornrat et al., 2005) are computationally so expensive that current computers can only handle one or two fractures. Therefore to save the computational efforts and avoid further complexities, the investigation was limited to the two-dimensional analysis on the horizontal plane. However, two dimensional model will provide a framework for further developments to three dimensional analysis.

The geometry of the induced fracture is dominated by the rock's mechanical properties, in-situ stresses, the rheological properties of the fracturing fluid and local heterogeneities such as natural fractures and weak bedding planes. In the case of an isotropic and homogeneous medium, the in-situ stress state is the controlling factor on fracture development (Weijers, 1995). Since in most cases, reservoirs do not satisfy these ideal conditions, it is worthwhile to understand the effect of other factors on hydraulic

3

fractures. In this dissertation, the effect of natural discontinuities on hydraulic fracture development will be investigated.

1.2. Hydraulic Fracturing in Naturally Fractured Reservoirs

Large volumes of natural gas are stored in low-permeability fractured reservoirs around the world. Tight gas sandstones are part of what is known as unconventional gas, which also includes coal bed methane, shale gas and natural gas hydrates. Based on the U.S. Gas Policy Act of 1978, if the in-situ gas permeability of a reservoir is equal to or less than 0.1 md, it is designated as a tight gas formation. Independent of this definition, natural fractures are extremely important to unconventional gas reservoirs (Aguilera, 2008) because without fractures, it is not possible to recover hydrocarbons from these reservoirs. Some examples of unconventional gas reservoirs are the Barnett Shale formation (with an estimated 2.5 trillion cubic feet exploitable gas reserved), the Mesa Verde formation in the Piceance basin, the Devonian carbonates in West Texas (Britt et al. 1994), the Devonian shale in the Antrim formation (Hopkins et al. 1998) and clay-carbonate reservoirs in China (Jiang et al. 2006). Because of the low permeability of these formations and the low conductivity of the natural fracture networks, stimulation techniques such as hydraulic fracturing are necessary to make economic production possible. The low conductivity of the natural fracture system could be caused by occluding cements that precipitated during the diagenesis process (Laubach 2003, Gale et al. 2007). All the cores recovered from the Forth Worth basin in the Barnett Shale contain

cemented natural fractures (Gale et al. 2007). In the Delaware basin, few partially cemented fractures are identified in the cores, and the rest of the fractures are sealed by cements (Ali et al. 2008).

The fact that natural fractures might be sealed by cements does not mean that they can be ignored while designing well completion processes. Cemented natural fractures can still act as weak paths for fracture growth. However, the presence of pre-existing natural fractures is not always advantageous.

One common observation in naturally fractured reservoirs is a high leakoff rate during the hydraulic fracturing. In some cases, fluid leakoff in these reservoirs are reported to be as high as fifty times larger than the fluid leakoff in non-fractured reservoirs. This issue becomes more interesting with the knowledge that in non-fractured reservoirs the leakoff rate is dependent on formation permeability, net treatment pressure and fracture fluid parameters (Valkó and Economides, 1995), whereas field observation during hydraulic fracturing in fractured reservoirs shows that, surprisingly, leakoff in these reservoirs primarily depends on net treatment pressure and fracture fluid parameters but not formation permeability (Barree 1998, Britt et al. 1994). Historically, attempts to fracture wells in naturally fractured reservoirs have been unsuccessful due to high leakoff rates and gel damage (Palmer et al. 1991). There is a threshold for net pressure above which natural fractures are open. If net pressure stays below this threshold, fractures remain closed and do not contribute to leakoff. This mechanism makes the leakoff rate in naturally fractured reservoirs strongly pressure dependent.

A typical approach to control high leakoff rate in fractured reservoirs has been to pump larger pad volumes, but the washout process has not been very successful. Fractures may close in a different order that they were opened, so gels could be entrapped in the fracture networks. The remaining gels could cause damage to the reservoir permeability.

New diagnostic tools developed during the last decade strongly demonstrate the existence of multiple fracture propagation or multi-stranded hydraulic fractures in naturally fractured reservoirs. Dynamic fracture mechanics indicates that only in cases where fracture propagation speed is comparable to the seismic velocity (more precisely, the Rayleigh wave speed) of the material, crack tip branching (shown in Figure 1.1) will occur (Freund 1990). However, field data demonstrate that hydraulic fractures propagate at much less speeds than seismic wave speeds (Valkó and Economides, 1995), so multi-branched fracturing should not exist in a homogeneous, isotropic, intact rock mass.
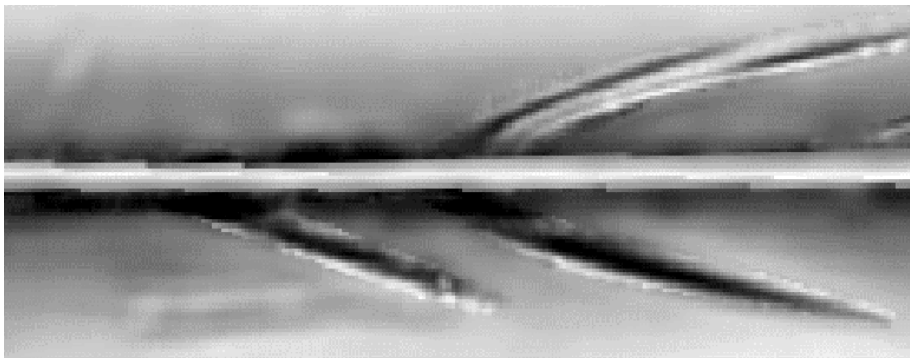
Figure 1.1: A typical view of branches as observed in Polymethyl methacrylate (PMMA). The main crack has propagated from left to right along the center of the photograph. The fracture propagation speed is about half of the Rayleigh wave speed of PMMA (from Fineberg and Marder 1999).

There is strong evidence from field data that supports the existence of multi-segmented induced fractures. One of North America's largest hydraulic fracturing operations during the 80s was conducted at Fenton Hill, New Mexico, to stimulate geothermal energy reservoirs. In the largest operation, 21,000 m^3 of water was injected into jointed granitic rock at a depth of 3.5 km (Murphy and Fehler 1986). Micro-earthquakes induced during this job were recorded with geophones placed in the wells that were drilled into the reservoir, as well as surface seismometers. The recorded micro-seismic events demonstrated a pattern for the hydraulic fracture propagation. However, this pattern was inconsistent with conventional fracturing theories. The conventional theories predict failure toward the orientation that is normal to the least compressive in-situ stresses, but in this case, the cloud of seismic events broadened in the direction of the minimum compressive stress. Murphy et al. (1986) argued that shear slippage along pre-existing joints is more easily activated than conventional tensile failure, particularly when the difference between minimum and maximum earth stresses is large and the joints are aligned along the direction of the principal earth stresses, and a low viscosity fluid such as slickwater is injected. They concluded that "shear slippage results in local redistribution of stresses, which allows a branching, or dendritic stimulation pattern to evolve, in agreement with the patterns of micro-seismic locations (Murphy et al. 1986).

The present day in-situ tectonic stress direction can be rotated from the time of the formation of natural fractures (Laubach et al. 2004). So, natural fractures are not necessarily aligned with the present day direction of maximum compressive stress. Thus, natural fractures may not be parallel with the hydraulic fracture and might be intersected

7

by the hydraulic fracture. Intersection with geological discontinuities such as joints, bedding planes, faults and flaws in reservoirs might render fractures non-planar and multi-branch.

Fracture branching and segmentation are frequently observed phenomena in outcrops (Pollard et al. 1975; Delaney and Pollard 1981). Therefore, studying fracture branching and segmentation are not only important in production engineering, but these studies also broaden the knowledge about the formation mechanisms of complex natural fracture systems. Olson (2004) considered the issue of multiple growing fractures in the characterization of fractured reservoirs. However for practical purposes, complex non-planar multi-stranded hydraulic fractures are generally modeled as single planar fractures. This simplification may overestimate net pressure in the fracture network, overestimate the propped length and width of an individual fracture and consequently increase the potential for early screen-outs and underestimation of fluid leak-off. In practice, such inaccurate conclusions may lead to a poor design of hydrofrac jobs and loss of productivity (Hallam and Last, 1991).

Fracture offset (fracture diversion) and fracture branching result in a reduction, at least locally, of fracture width. Local fracture width reduction may cause proppant bridging and pre-mature screen-out. For instance, hydraulic fracturing in the Minami-Nagoka gas field encountered premature screen-out (Sato et al., 1998). Based on their report, only 20% of the designed volume of proppant was placed in the reservoir. Fracturing pressure analysis typically attributes screens-outs to either excessive fluid leakoff or insufficient fracture width. However, Sato et al. did not observe excessive fluid

8

leakoff. Additionally, the extremely high net pressure (4000 psi) would imply a relatively wide fracture if only a single-stranded hydraulic fracture is assumed. With further pressure analysis, they were able to show the existence of multi-stranded fractures.

Hopkins et al. (1998) analyzed the performance of hydraulic fracturing in the fractured Antrim shale in Michigan. Their microseismic imaging results described a cloud of fracturing events within approximately 50ft of the presumed hydraulic fracture tip. These measurements were validated with eight hydraulic fractures recovered in cores from two deviated wellbores drilled across the hydraulic fracture trend. Despite the high differential stresses, they concluded that complex fracture paths are primarily controlled by Antrim Shale natural fractures geometry. This conclusion was in contrast with Blanton's theory (Blanton, 1982), which limits natural fracture dilation to locations with low differential stresses.

On the other hand, Warpinski and Teufel (1987) recognized the difference between the in-situ stresses as the governing factor for fracture cross-over or fracture diversion in mineback experiments (Figure 1.2). However, mineback experiments have several major differences from hydraulic fracturing, such as shallow depth and low confining stresses. On the other hand, it is not feasible to monitor hydraulic fractures in the subsurface with great precision, because of the limited access to the subsurface. Tiltmeters and microseismic monitoring do not have a sufficient resolution to identify small scale fracture complexity. However, it is possible to gather some qualitative data about far-field fracture complexity from fracture pressure analyses (Cipolla et al. 2008) and core studies.

Warpinski et al. (1993) analyzed the characteristic of the core acquired from the Williams Fork formation of Mesaverde group in the Piceance basin, Colorado six years after the hydraulic fracturing treatment. They identified two sets of propped multiple-fracture zones, which were offset by 75ft. Cores recovered from Antrim Shale of the Michigan Basin also contained multiple fracture zones containing sand (Hopkins et al. 1995). These direct observations provide stronger evidence to challenge the concept of the conventional two planar symmetric wing models.

Figure 1.2: Part of the hydraulic fracture (red line) exposed by mining at Northparkes. Note offset as the fracture interacts with a cemented natural fracture (by Rob Jeffrey from CSIRO website). The hydraulic fracture propagated from right to the left. Offset (diversion) point is demonstrated by an arrow.

Efforts to understand this problem are not limited to field observations and mathematical modeling. Lab experiments were also performed to reproduce field data and examine mathematical models. Lamont and Jessen (1963) performed 70 hydraulic fracturing experiments in six different rock types, using triaxial compression (up to 1140 psi) with different approach angles to understand the fracture crossing phenomenon. The size of their samples was less than a meter. Hydraulic fractures appeared to crossover closed pre-existing fractures at all intersection angles. However, Lamont and Jessen noted that the fracture propagation speeds in their lab models were considerably greater than the field tests, making their results less reliable.

Daneshy (1974), based on his experiments, argued that the hydraulic fractures appeared to be arrested when the natural fractures were open at the intersection point and appeared to cross the natural fractures when they were closed. Later, Anderson (1982) showed the importance of friction on hydraulic fracture growth near unbonded interfaces in rock. These tests were performed in Nugget sandstone and Indiana Limestone under uniaxial loading. The results lead to the concept of a threshold of normal stress below which hydraulic fracture growth is arrested by a natural fracture. They found that this normal stress is inversely proportional to friction between surfaces of the natural fracture.

Blanton (1982 and 1986) performed similar experiments to generalize Anderson's (1982) results for different intersection angles. He used blocks of Devonian Shale (12×12×15 inches) cast in hydrostone to show that a hydraulic fracture crosses over the pre-existing fracture only under high differential stresses and high angles of approach. He noted that in most cases fractures were either diverted or arrested by pre-existing

11

fractures, but he did not provide any threshold for the approach angle to predict fracture arrest or fracture diversion. Cleary et al. (1991) argued that fracture energy (due to its pressure) is high enough to open any fracture in any orientation, but they did not give any clear scheme or analysis for their claim.

The complex propagation paths discussed by Warpinski (1993) lead to higher pressure drops, causing the drainage radius of the induced fracture become less than that predicted by theories for non-fractured reservoirs. However in some reservoirs, fracture pattern complexity is more favorable as it leads to more recovery from very low permeability reservoirs (Cipolla et al. 2008).

In some papers, abnormally high net pressure has been accredited to simultaneously propagating multiple strands (for instance Stadulis 1995), because the sub-parallel pressurized fractures are trying to close each other. Cleary et al. (1994) considered a number of field examples in which multiple far-field fractures played a key role. They concluded that the pressure fall-off after the treatment is closer to the behavior of fall-off from multiple fractures, and a single fracture alone cannot match the data.

A schematic illustration of the fracture intersection with a geological discontinuity is depicted in Figure 1.3. Due to a high stress anisotropy, the hydraulic fracture may not be able to re-open the natural fracture, but the shear slippage along the natural fracture will initiate new fractures that do not have a hydraulic connection with the main fracture strand and grow in the direction normal to minimum horizontal stress. Thus the effect of fractures on proppant transport could be severe. The new propped fracture could be kept

open by the friction force of the joint surfaces only. Generally, the non-planarity of the fracture system hinders proppant transport through the network (Warpinski 1987).

Adverse effects of hydraulic fracturing are not limited to the high pressure drop or hindering proppants transport. Induced stresses by propped hydraulic fractures may close or reduce the aperture of open natural fractures (Palmer 1993) as schematically show in Figure 1.4. Induced hydraulic fractures facilitate fluid production and corresponding pressure drawdown, reduction of pore pressure increases effective stresses, which will decrease natural fractures' openings and consequently fracture permeability (Buchsteiner et al. 1993). Therefore in case of pressure sensitive reservoirs, the overall permeability of the reservoir may decrease by hydraulic fracturing. Damage to the reservoir permeability could also be caused by gel remnants trapped in natural fractures (Branagan 1987, Palmer et al. 1991).
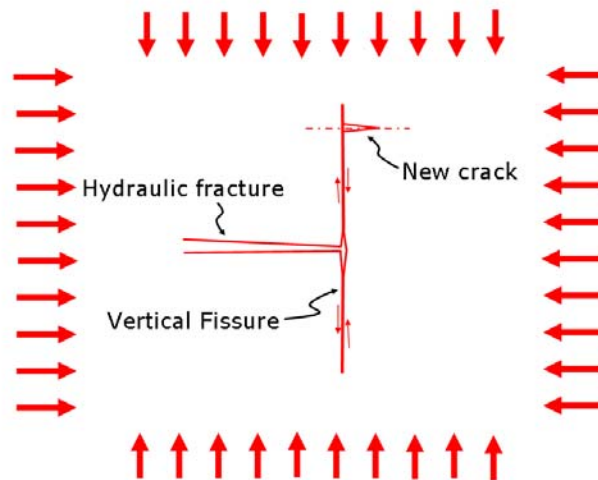
Figure 1.3: An example of a complex hydraulic fracture pattern growth by slippage along a fissure due to a high stress anisotropy.

Rodgerson (2000) focused more on damage mechanisms and cleanup problems as major challenges for hydraulic fracturing treatment in naturally fractured reservoirs. He recognized three major types of damages: proppant pack damage, damage to matrix permeability and plugging of natural fractures. However, his work does not contain any clear analysis or explanation of these damage mechanisms. His analysis only considered post-frac fall-off pressure. He suggests using improved breaker systems and low-molecular weight polymers to avoid plugging natural fractures.
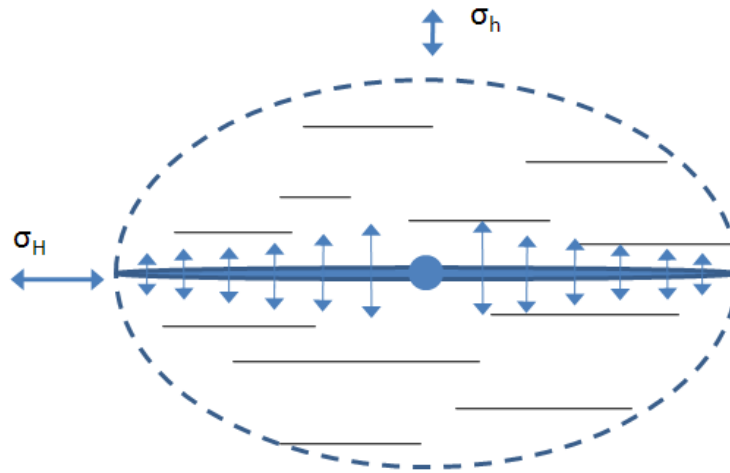
Figure 1.4: The hydraulic fracture, surrounded by parallel natural fractures, is located in the middle of this schematic picture. Some natural fractures may close under the pressure of the induced hydraulic fracture. σ_H and σ_h are minimum and maximum horizontal stresses, respectively.

Considering the detrimental effects of natural fractures on hydraulic fracturing, in many cases hydraulic fractures were designed to reduce the fracture complexity by

adding some particulates to plug the small natural fractures (Britt et al. 1994, Batendburg and Hellman 2002). No matter how successful this approach could be, it leads to the neglect of the inherent advantage of these reservoirs, i.e. the presence of fractures as high permeability fluid conduits.

Following the approach mentioned in the previous paragraph, the results of the hydraulic fracturing treatment could have a negative outcome in fractured reservoirs. To avoid such situations, it is necessary to review long-held assumptions such as a single planar fracture in classical approaches to this problem. Nolte (1987) stated that the next meaningful advance in hydraulic fracturing "must address the case of multiple fractures and slippage at joints".

To handle the conceptual transition from a classical planar fracture to a more complex fracture network and propagating multiple hydraulic fractures, it is needed to develop better models and theories. These models should explain the physics behind the interaction between the hydraulic fracture and natural fractures and incorporate other sides of the problem such as competition between multiple fracture tips.

Understanding the geometry, the growth process and the interaction with natural fractures is important for designing, monitoring and assessing the induced fractures and their effects on the wellbore production. Here, the efforts were aimed at developing models to explain and predict these observations.

1.3. Hydraulic Fracturing Models

Even in the most basic form, hydraulic fracturing is a complex process, not just because of the heterogeneity of the earth structure, and indeterminate in-situ stresses or rock behavior, but also because of the physical complexities of the problem. It involves coupling three processes: (i) mechanical deformation of the formation caused by the pressure inside the fracture, (ii) fluid flow within the fracture networks and (iii) fracture propagation. Rock deformation is usually modeled with the theory of linear elasticity. The fluid flow inside the fracture is usually simplified to flow along a channel by using lubrication theory, which is represented by a nonlinear partial differential equation that relates the fluid flow velocity with the fracture width and pressure gradient along the fracture. The fracture propagation process is usually considered in the framework of linear elastic fracture mechanics (LEFM) theory.

When ambiguities such as the effect of pre-existing fractures or the effect of the multi-layers are added to these issues, they bring up more uncertainty and complexity to the problem. This problem needs more investigation concerning the effects on each of the processes described in the previous paragraph.

There have been some efforts to model fully three-dimensional hydraulic fractures (e.g. Sousa et al, 1993 and Rungamornrat et al. 2005). But these efforts were limited to a few numbers of fractures due to the computational complexities of 3D problems. Consequently, this investigation is limited to the modeling of two-dimensional configurations.

The first simplified theoretical models for hydraulic fracturing were developed in the 1950s (Crittendon 1950, Harrison et al. 1954 and Hubbert and Willis 1957). The methods of fracture mechanics were first applied to this problem by Barenblatt (1956 and 1962). One of the pioneering works in this era was a paper by Perkins and Kern (1961) who adapted the classic Sneddon (1946) elasticity plane-strain crack solution to establish the so-called PK model shown in Figure 1.5. Nordgren (1972) modified the PK model to devise the PKN model, which included the effects of fluid loss to the formation. Nordgren's formulation was based on substituting the elliptic fracture opening relation into the lubrication equation. Khristianovic and Zheltov (1955), and Geertsma and de Klerk (1969) independently developed the so-called KGD (plane strain) model depicted in Figure 1.6. Estimates of the fracture growth rate based on simple elastic models and the approximate integration of Reynolds' equation have been reviewed extensively by Geertsma and Haafkens (1979). Daneshy (1973) extended the KGD model for the case of power-law fluids, and Spence and Sharp (1985) introduced fracture toughness into the model.

The PKN and KGD models differ in one major assumption: the way in which they convert a three-dimensional solid and fracture mechanics problem to a two-dimensional plane strain model. Khristianovic and Zheltov assumed plane strain in the horizontal direction i.e. all horizontal cross sections act independently or equivalently, which is equivalent to assuming that the fracture width changes much more slowly vertically along the fracture surface from any point on the fracture surface than it does horizontally. In practice it is true if the fracture height is much greater than the length or if free slip

17

occurs at the boundaries of pay zone. Perkins and Kern, on the other hand, assumed that each vertical cross section acts independently (Figure 1.5), which is equivalent to assuming that the pressure at any section is dominated by the height of the section rather than the length of the fracture. This is true if the length is much greater than the height. This difference in one basic assumption has lead to two different ways of solving the problem. In the case of the PKN model, the effect of the fracture tip is not considered; the concentration is on the effect of fluid flow and the corresponding pressure gradients. In the KGD model, however, the tip region plays a much more important role.
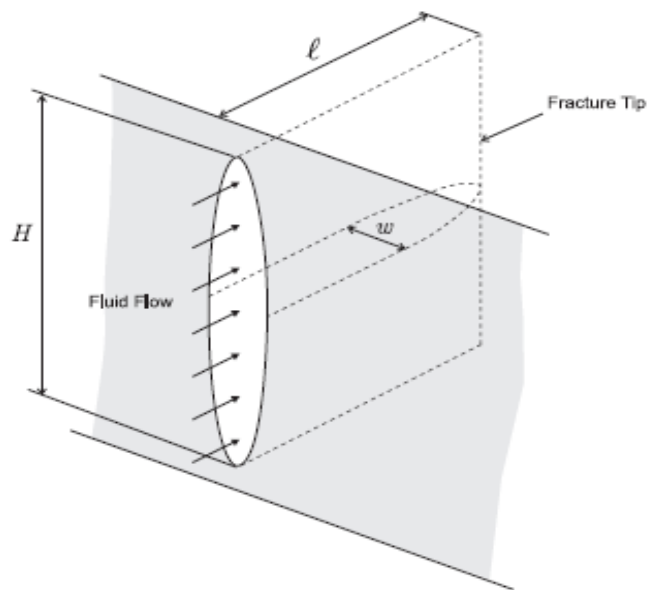
Figure 1.5: Schematic illustration of PKN fracture model (borrowed from Adachi et al. 2007).The parameters l, H and w are fracture height, length and width, respectively.
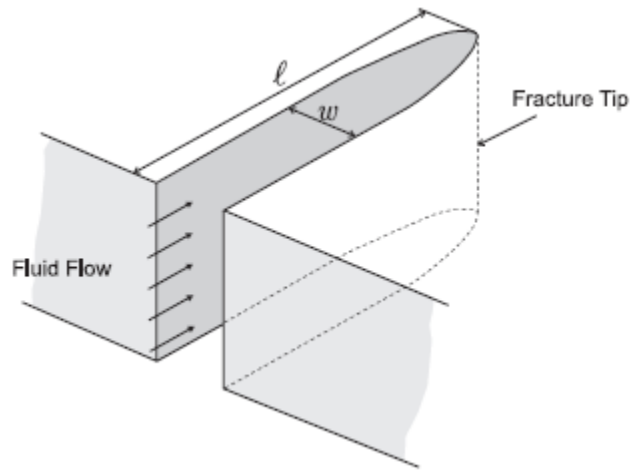
Figure 1.6: Schematic picture of KGD model (borrowed from Adachi et al. 2007). The parameters *l, H* and *w* are fracture height, length and width, respectively.

Several different approaches have been used to solve these problems. In recent years, there has been a return to analytical solutions to achieve a better understanding of different regimes of fracture propagation. Analytical solutions are limited to very simple planar geometries in a homogeneous isotropic medium, but they provide insight about the asymptotic behavior of the pressure distribution near the fracture tips. Additionally, the type of singularities verified in analytical solutions can be used for selecting the most appropriate test functions to obtain an optimal convergence rate in numerical solutions. A significant amount of research has been carried out to obtain analytical solutions for several cases: the zero-toughness, impermeable case (Desroches et al. 1994); the zero-toughness, leak-off dominated case (Lenoach 1995); and the development of previous cases for toughness- dominated regimes (Detournay and Garagash 2003).

These studies have shown that hydraulic fractures can be understood within a parametric space defined by dimensionless numbers, whose extremes are controlled by

19

toughness, viscosity, or leak-off dominated regimes. The hydraulic fracture evolves in this parametric space over time (Detournay 2004, Adachi and Detournay 2007). So, researchers were able to categorize hydraulic fracturing using the dimensionless groups that control different competitive processes.

The first similarity solution for the hydraulic fracturing problem was presented by Spence and Sharp (1985). This solution has become a reference point for studying numerical solutions. The method involves self-similar (power-law) relations between the fracture pressure and the fracture opening itself. An object is said to be self-similar if it looks "roughly" the same on any scale. They expanded the solution for fracture opening in a Chebyshev series with unknown coefficients. Using insights from fracture mechanics, they presumed square-root tip asymptotics for the fracture opening. The pressure was then determined by integrating the elasticity equation. They utilized the stress intensity factor to control the propagation of the fracture.

Following this approach, Adachi and Detournay (2002) investigated the self-similar solution of a plane-strain hydraulic fracture problem. Their methodology was based on Spence and Sharp's (1985) paper, but with some differences. Toughness was neglected in their solution. They assumed that there was no lag between the fluid and the fracture tip during fracture propagation.

Simultaneously, some efforts were put into developing similar solutions and concepts for penny-shaped fractures. Since this geometry was not considered in this research, this part of the literature was not covered. Further information can be found in Adachi et al. (2007).

More comprehensive reviews of analytical solutions in the literature can be found in Advani et al. (1997), and Adachi et al. (2007). As noted earlier, the analytical solutions do not only provide useful benchmarks for numerical simulations. They also determine the type of the asymptotic behavior of the fluid pressure near the fracture tips, which can be used in the framework of partition unity methods(will be discussed in chapter 2) to solve more general problems.

Several numerical solutions for the fluid flow-driven fracture problem have been proposed in the past three decades. There are essentially two main choices for discretizing the elasticity equations to solve the equations numerically: 1) an integral equation formulation such as the displacement discontinuity method (Olson 1995, Yew and Liu 1993); or 2) discretization of the partial differential equations via the finite element or finite difference methods.

Cleary and Wong (1985) presented a boundary-element based numerical approach for solving the penny-shaped model. They used ring dislocations distribution to approximate the fracture width. Then, the resultant elasticity equation was solved by using Gauss-Chebyshev quadrature method, and the fluid component was solved using the finite difference method.

Advani and Lee (1992) used finite element methods to discretize Nordgren's one-dimensional formulation. This methodology was unable to incorporate fracture interactions or even non-planar fracture growth. Desroches and Thiercelin (1993) developed a numerical model based on variational methods and on the integral equations approach for the elasticity equation, relating the gradient of the fracture's width to the net

fluid pressure in the fracture. This method was also limited to planar fractures. Later, Olson (1995) used boundary element methods to simulate non-planar hydraulic fracture growth from highly deviated wells.

Siebrits and Peirce (2000) presented a fully coupled method for modeling planar three-dimensional fluid-driven fractures in a layered medium. They used a Fourier-based displacement discontinuity method to generate the layer dependent influence coefficients matrix from the elasticity equations. In this model, the fluid equations were solved using a standard finite difference method. Most of the methods discussed in this section failed to deal with intersecting fractures or even multi-fracture systems. In order to apply their methods to naturally fractured reservoirs, some modifications are necessary.

1.4. Modelling Hydraulic Fracturing in Fractured Reservoirs

Models for hydraulic fracturing in fractured reservoirs should be established on the pre-existing set of fractures. It is essential to start with a realistic model for the geometry of natural fractures in order to produce a reasonable and realistic realization for hydraulic fracturing in these reservoirs. Natural fractures may be characterized through core and log analysis. Advanced logging techniques such as FMI (Fullbore Formation Micro-Imager) and EMI (Electro Micro-Imaging) may be employed to facilitate the determination of the existence and estimation of the average properties of natural fracture sets (Daveies et al. 1992, Schoenberg and Sayers, 1995). Furthermore, using techniques such as enhancements in pressure fall-off analysis and pre-job injection diagnostics

(Johnson et al., 1998), it is possible to estimate the potential impacts of natural fractures prior to starting a frac job.

In the literature, fracture patterns are usually generated by random methods (e.g. Zhang 2002), but in nature, fracture patterns are not the product of purely random phenomena. For this reason, some efforts were made toward applying fracture mechanics to generate more realistic fracture patterns. This approach attempted to reproduce the same fracture spacing, length and aperture distributions (Olson, 1993). Young's modulus of elasticity, subcritical crack index, mechanical bed thickness, and tectonic strains (and/or pore pressure) are the input parameters of the mechanical model. Olson (2004) has shown that fracture patterns (particularly with respect to clustering) are dependent on the subcritical index (SCI) for a constant strain, mechanical bed thickness, and elastic properties of rock. He showed that high subcritical crack indices cause fractures to grow as clusters where the median fracture length is low and the overall fracture intensity is also low. Intermediate values of SCI lead to fairly regular spacing with larger median lengths; very low indices lead to larger fracture lengths. After establishing a realistic model for natural fractures in subsurface, the next step is modeling the interaction between the hydraulic fracture and surrounding natural fractures.

Jeffrey et al. (1987) used two dimensional displacement discontinuity methods for investigating the interaction between natural fractures and the hydraulic fracture. They were able to model slippage along the hydraulic fracture due to the presence of natural fractures.

Akulich and Zvyagin (2008) investigated the interaction between a growing hydraulic fracture and a fault in an infinite impermeable elastic medium under plane strain conditions. They considered incompressible Newtonian fluid for the fracturing fluid and the Mohr-Coulomb criterion for fault failure. For fluid flow inside the hydraulic fracture, they assumed zero net pressure at the front as the boundary condition. Their modeling did not include fracture intersections, but it gives an idea about the slippage along the fault and how it affects the stress intensity factors at the tip of the growing hydraulic fractures.

De Pater and Beugelsdijk (2005) used the Distinct Element Method to couple fluid flow in fractures and deformation of the formation. It is possible to handle multiple fracture propagation using this method, but the fracture network geometry depends on the shape of the elements. Very fine elements are needed to reduce the sensitivity of the results to the size and shape of the elements. The elements are assumed as rigid bodies but the contact between elements is elastic. Determining consistent values for elastic contact parameters introduces further complexities into the problem.

Lam and Cleary (1984) attempted to solve a similar problem. They modeled the effect of frictional interfaces (bedding planes) on hydraulic fracture growth under plane strain conditions, so slippage (not opening) along the natural fracture played the main role in this scenario (Figure 1.7). They used boundary element methods (the displacement discontinuity method) to address this problem. However, they assumed a constant fluid pressure inside the fracture. Zhang et al. (2007) incorporated fluid flow into this problem and solved the resultant coupled equations.
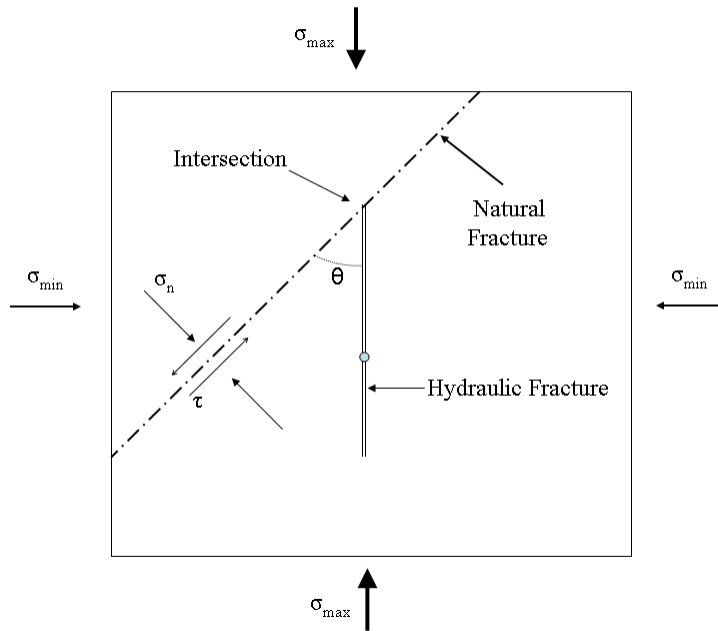
Figure 1.7: Schematic plan view of the hydraulic fracture approaching and intersecting a natural fracture is depicted.

More recently, Lecampion (2008) attempted to use the Extended Finite Element Methods (XFEM) to solve this problem. He sought the elasticity solution via XFEM for a given fracture geometry with either specified pressure distribution or opening profile. Modeling was limited to fractures located along the element edges; the fracture propagation and coupling process were not addressed in Lecampion (2008). The main advantage of XFEM was neglected by assuming that the fractures were required to be aligned with the element edge.

This area of hydraulic fracture modeling in naturally fractured reservoirs is new, not many researchers have worked on this subject so far. Therefore, there are few resources on this problem in the literature.

1.5. Outline of the Dissertation

The main objective of this dissertation is to understand and predict the interaction of a hydraulic fracture with pre-existing natural fractures. Natural fractures can be partially or completely sealed by cements. The main interest of this study is the investigation of dominant factors that governing the diversion or offset of hydraulic fractures in the presence of natural fractures. A new mechanism for remote reactivation of fractures will be introduced. This study attempts to address some questions about the probable effects of natural fractures on the formation of multi-stranded fractures and the existence of the scattered seismics during hydraulic fracturing treatments.

On the basis of this dissertation, it can be briefly stated that the goal is to characterize hydraulic fracture growth as a function of stress field, rock and cement properties and natural fractures present to be able to predict the size and orientation of induced hydraulic fractures. Due to the computational complexity of three dimensional analysis of fractures, all the analyses will be limited to the two dimensional geometries. The result will yield a methodology for a better understanding to map hydraulic fracture placed into naturally fractured rock and the mean to predict and avoid difficulties in the hydraulic fracturing process.

Chapter two of this dissertation introduces the governing equations for fracture mechanics analysis and explains the basics of the numerical tool applied to this problem; the extended finite element methods (XFEM). The chapter terminates with examples to verify model accuracy. Chapter three will apply this methodology to treat the effect of natural fractures on the growing hydraulic fractures. Preliminary results for uniform

pressure distribution are presented. Chapter four introduces fluid flow calculation to the model developed in Chapter 3. Complexities involved in coupling fracture mechanics and fluid flow simulations will be discussed in detail. In the second part of this chapter, the model will be adapted to perform fluid flow calculation in the case of hydraulic fracture diversion into natural fractures.

The last chapter will outline results achieved by using this model and will suggest further steps to develop the presented methodology. Some applications of this research finding will be discussed in more detail. Immediate future works to extend this project will be presented.

Chapter 2. The Numerical Method

In this chapter, the theoretical foundation of the problems solved in the next chapters will be introduced. The numerical tool to simulate these problems will be explained in detail. Subsequently, the advantages of these methods that persuaded us to choose them for the purpose of this research will be discussed.

The governing equations for quasi-static crack propagation in the strong form and the weak form will be presented. Based on these forms, the Extended Finite Element Method (XFEM) formulation will be derived. The post-processing methods for crack propagation calculations, especially for stress intensity factors calculations, will be discussed. Some important aspects were incorporated in the model to address issues such as crack coalescence, crack branching and complex geometry issues that arise during the hydraulic fracturing treatments.

2.1 Introduction

The investigation is limited to two dimensional methods here. The key simplification is that the plane strain model assumes that the fracture is infinite in extent in one direction. This is not necessarily a good assumption, but the presented model is a preliminary model testing an entirely new method, and for computational simplicity, it

was chosen to sacrifice the three dimensional aspects of the problem. A more complete model must ultimately add those three dimensional aspects back in the calculation.

Various techniques have been proposed in the literature for dealing with the crack growth problem. As an example, discrete element methods (like the spring-network model, Curtin and Scher 1990) are very intuitive and somewhat easier to implement in comparison to other available methods. However, elastic homogeneity and grid-independent crack propagation cannot be achieved in those types of models. Boundary element methods (e.g. Aliabadi and Brebbia, 1993) have also been used widely in the fracture mechanics literature, but incorporating inhomogeneities into these techniques is cumbersome. Furthermore, boundary element methods generate full matrices, which require large amounts of memory to store, and require greater computational effort to solve the associated system of equations. This issue worsens in larger problems with many fractures.

In the finite element framework, modeling of crack growth has been carried out applying various remeshing strategies in the literature (for example Martha et al. (1993), Carter et al. (1997), Bouchard et al. (2000) and Patzak and Jirásek (2004)), but remeshing is computationally burdensome, involving the transfer of data between the different meshes. To address this inefficiency, the extended finite element method (XFEM) was developed (Moës et al. 1999). In this approach, discontinuities like fractures are allowed to propagate independently of the mesh configuration by permitting the discontinuity to cross the elements. For this purpose, finite element space will be enriched by additional functions which are inspired from the analytical or asymptotic solution of the problem.

For instance, it makes it possible to embed discontinuities in the solution space. The enrichment is performed from node to node in a mesh by activating extra degrees of freedom when needed.

XFEM has been utilized for two dimensional static and quasi-static problems. Strouboulis et al. (2000) used local enrichment to model holes and corners. Belytschko and Black (1999) applied the partition of unity enrichment for crack displacement discontinuity and near tip fields. The partition of unity principle provides a mathematical framework to enrich a finite element space with a global function while keeping the sparsity of the stiffness matrix (Melenk and Babuŝka, 1996). Daux et al. (2000) developed this method for modeling holes and intersected or branched cracks. The application of this technique for three dimensional cracks has been carried out by Sukumar et al. (2000) and Moës et al. (2002). Recent applications of this method include dynamic crack propagation (Réthoré, 2005) and shear band propagation (Song et al., 2006), cohesive fracture (Asferg et al., 2007), polycrystals and grain boundaries (Simone et al., 2006), and dislocations (Ventura et al., 2005; Gracie et al., 2007).

Numerical techniques such as the generalized finite element method (Strouboulis et al., 2001) and the element partition method (Duarte et al., 2001) are also based on the partition of unity principle. The partition of unity generalizes the standard Galerkin finite element approximation by providing a technique to embed local solutions of boundary value problems (or at least asymptotic behavior of discontinuities) into the finite element method. In XFEM, the framework of the partition of unity is used to enrich the classical displacement-based finite element approximation with discontinuous functions such as

the Heaviside function and Westergaard functions. Some of the advantages of the XFEM are: the symmetry and sparsity of the stiffness matrix is preserved; the crack geometry can be completely arbitrary with respect to the mesh; and automatic enforcement of continuity.

The extended finite element (XFEM) approximation is based on the decomposition of the displacement field into two parts as

$$u = u^C + u^E,$$ (2.1)

where u^C is the continuous displacement field and u^E is the discontinuous (or the enriched) part. The continuous component is approximated by the classic finite element shape function,

$$u^C = \sum_{I \in S} N_I(x) u_I,$$ (2.2)

where S is the set of all nodes in the domain, N_I are the shape functions and u_I are the nodal unknowns. The enrichment part is given as

$$u^E = \sum_{\tau=1}^{n_{enr}} \sum_{J \in S^\tau} \tilde{N}_J(x) \Psi^\tau(x) a_J^\tau,$$ (2.3)

where n_{enr} is the number of types of enrichments. For instance for crack tip enrichment, n_{enr} is four (equations 2.15-2.18). Ψ^τ are enrichment functions, S^τ is the set of nodes enriched by Ψ^τ, and a_J^τ are the unknowns associated with node J for enrichment function τ.

31

The shape functions for the enrichment, $\widetilde{N}_J$, are not necessarily the same as the shape functions for the continuous part of displacement approximation, N_I. In this work linear shape functions have been used for the enrichment. Linear and quadratic functions are utilized for the continuous part of the displacement. For the sake of numerical efficiency and simplicity, equation (2.3) can be rewritten as

$$u^E = \sum_{\tau=1}^{n_{enr}} \sum_{J \in \mathbf{S}^\tau} \widetilde{N}_J(x)\left(\Psi^\tau(x) - \Psi_I^\tau(x)\right)a_J^\tau. \tag{2.4}$$

Note that the enrichment function is shifted by its nodal value Ψ_I^τ so that the displacement enrichment vanishes at nodal points. To treat displacement discontinuities, interpolation shape functions in equation (2.4) do not need to be the same order as continuous part of displacement. For example, for the 6 node triangular elements, their midpoints are not used for the displacement enrichment. The details of Ψ_I^τ functions will be given in the next sections.

2.2 Governing equations

Although many techniques presented here are applicable to non-linear, inelastic, large deformation problems, but only small linear elastic deformations are considered. Let Ω be a regular body bounded by a smooth curve Γ. The boundary Γ of the body Ω can be divided into Γ_u and Γ_t, depending on whether the boundary conditions at a given location on the boundary are displacement (Dirichlet) boundary conditions (Γ_u) or

32

tractions (Γ_t). Let u and ε be the displacement and strain field respectively. Strain is defined as

$$\varepsilon = \nabla_s u, \tag{2.5}$$

where ∇_s indicates the symmetric part of the gradient.

For traction-free cracks, the strong form of the initial boundary value problem has the following form

$$\sigma_{ij,j} + b_i = 0 \qquad \text{in } \Omega,$$

$$u = \bar{u} \qquad \text{on } \Gamma_u,$$

$$\sigma \cdot n = \bar{t} \qquad \text{on } \Gamma_t, \tag{2.6}$$

$$\sigma \cdot n = 0 \qquad \text{on } \Gamma_{cr},$$

where σ is the Cauchy stress tensor, b the body force per unit volume, n the outward unit normal vector to the boundary, $\bar{u}$ prescribed displacement and the $\bar{t}$ prescribed traction. The stress and strain are related by the linear elastic constitutive law

$$\sigma_{ij} = C_{ijkl}\varepsilon_{kl}, \tag{2.7}$$

where C_{ijkl} are the components of the elasticity tensor.

2.3 Weak Form Formulation

Let u be the solution for the boundary value problem (2.6), with $\sigma(u)$ the corresponding Cauchy stress tensor. In the absence of inertial forces, the elements of the stress tensor must satisfy the elastic equilibrium equation for the static case, given by

33

$$\sigma_{ij,j} + b_i = 0 \quad in \ \Omega. \tag{2.8}$$

This equilibrium equation is the set of two coupled second-order elliptical partial differential equations for the two dimensional problem.

To build a variational solution, it is required that the trial functions u satisfy all displacement boundary conditions and usual smoothness (C^0),

$$u \in U, U = \left\{ u | u \in C^0 \text{ except on } \Gamma_{cr}, u = \bar{u} \text{ on } \Gamma_u \right\}. \tag{2.9}$$

The test functions δv are defined by

$$\delta v \in U_0, U_0 = \left\{ \delta v | \delta v \in U_0 \text{ except on } \Gamma_{cr}, \delta v = 0 \text{ on } \Gamma_u \right\}. \tag{2.10}$$

The weak form of the equilibrium equation and traction boundary condition is

$$\int_\Omega \sigma(u) : \varepsilon(\delta v) d\Omega = \int_\Omega b.\delta v d\Omega + \int_{\Gamma_t} \bar{t}.\delta v d\Gamma \qquad \forall \delta v \in U_0, \tag{2.11}$$

where : represents tensor products (Gonzalez and Stuart, 2008). In the case of linear elastic material, one can obtain the following weak form from equation (2.11),

$$\int_\Omega \varepsilon(u) : C : \varepsilon(v) d\Omega = \int_\Omega b.v d\Omega + \int_{\Gamma_t} \bar{t}.v d\Gamma \qquad \forall \delta v \in U_0. \tag{2.12}$$

2.4 Extended finite element approximation

An important feature of crack deformation is that stress varies as the inverse of the square root of distance from the crack tip ($1/\sqrt{r}$, where r is the radial distance from the crack tip), and it is desirable to include this asymptotic solution in the enrichment for elements adjacent to a crack tip. In standard FEM using 6-node isoparametric triangular elements, crack-tip singularity is approximated by moving the mid-side node to the

34

quarter point, but the results are not very accurate. XFEM incorporates the asymptotic terms explicitly for a much more accurate solution at lesser computational cost.

When solving crack problems using XFEM, the nodes are divided into three different node sets:

N : the set of all nodes in the discretized model;

N_{TIP} : the set of nodes of all elements containing the crack tip;

N_{cr} : the set of nodes of all elements containing cracks but not crack tips.

Therefore, in developing extended finite element for the crack growth problem, it is necessary to distinguish between elements in the vicinity of the fracture tip and elements that surround the remainder of the crack (see Figure 2.1) from other elements in the model.

Now the solutions are set up for each node set, the displacement approximation for any point in Ω can be written as follows

$$
u^h(x) = \sum_{I \in N} N_I(x) u_I + \sum_{I \in N^{cr}} \tilde{N}_I(x)(H(x) - H(x_I)) a_I +
$$
$$
\sum_{I \in N^{TIP}} \tilde{N}_I(x) \sum_{k=1}^{4} (F^k(r,\theta) - F^k(x_I)) b_I^k
\qquad , \qquad (2.13)
$$

where x is the position vector, u_I is the nodal displacements, N_I and $\tilde{N}_I$ are the shape functions for non-enriched and enriched nodes, respectively. $H(x)$ is a modified Heaviside step function given by
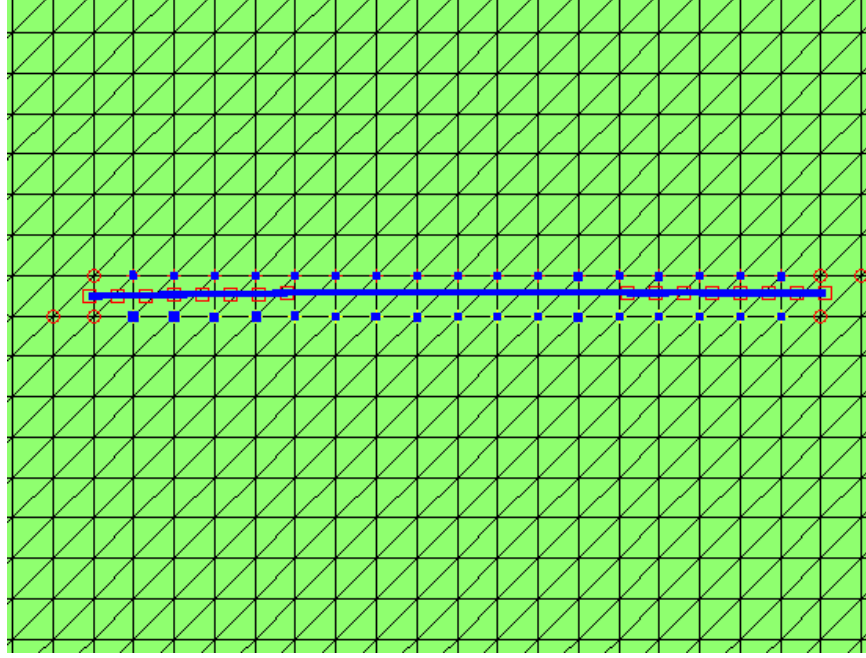
Figure 2.1: Nodal enrichment for a single crack inserted in a large elastic medium. Nodes with tip-enrichment are indiacted by red circles. Nodes with step function enrichment are shown by solid blue squares. Red squares show the location of crack tip in previous time-steps.

$$H(x) = \begin{cases} -1 & \text{if } x < 0 \\ +1 & \text{if } x > 0. \end{cases} \tag{2.14}$$

$H(x_I)$ in equation (2.13) is the value of the Heaviside function at node I.

The F-enrichment terms, $F^I(r,\theta)$, in equation (2.13) are the bases for the Westergaard field for the crack tip. The F-enrichment terms are defined in Fleming et al. (1997) as

$$F^1(r,\theta) = \sqrt{r} \sin\frac{\theta}{2}, \tag{2.15}$$

$$F^2(r,\theta) = \sqrt{r} \cos\frac{\theta}{2}, \tag{2.16}$$

$$F^3(r,\theta) = \sqrt{r}\sin\frac{\theta}{2}\sin\theta\,,$$

(2.17)

$$F^4(r,\theta) = \sqrt{r}\cos\frac{\theta}{2}\sin\theta\,,$$

(2.18)

where r and θ are local polar coordinate system at the crack tip. In the case that a crack tip is coincident with a finite element edge, it is needed to avoid linear dependencies between basis functions by limiting the enrichment to nodes located on the crack.

By substituting the displacement approximation into the strain definition (equation 2.5); the following formula is obtained

$$\varepsilon^h = \overline{B}u\,,$$

(2.19)

where

$$\overline{B} = [B_I^u \quad B_J^a \quad B_K^{b1} \quad B_K^{b2} \quad B_K^{b3} \quad B_K^{b4}]\,.$$

(2.20)

Noticing that indices in the equation (2.20) are varying as $I = 1,...,N$, $J = 1,...,N^{cr}$ and $K = 1,...,N^{TIP}$. The components of the strain displacement matrix have the following forms (Budyn et al., 2004)

$$B_I^u = \begin{bmatrix} N_{I,x} & 0 \\ 0 & N_{I,y} \\ N_{I,y} & N_{I,x} \end{bmatrix}\,,$$

(2.21)

$$B_J^a = \begin{bmatrix} \left(\tilde{N}_J\left(H - H(x_J)\right)\right)_{,x} & 0 \\ 0 & \left(\tilde{N}_J\left(H - H(x_J)\right)\right)_{,y} \\ \left(\tilde{N}_J\left(H - H(x_J)\right)\right)_{,y} & \left(\tilde{N}_J\left(H - H(x_J)\right)\right)_{,x} \end{bmatrix}$$

(2.22)

and

$$B_K^{bl}\Big|_{l=1,2,3,4} = \begin{bmatrix} \left(\tilde{N}_K\left(F_K^l - F_K^l(x_K)\right)\right)_{,x} & 0 \\ 0 & \left(\tilde{N}_K\left(F_K^l - F_K^l(x_K)\right)\right)_{,y} \\ \left(\tilde{N}_K\left(F_K^l - F_K^l(x_K)\right)\right)_{,y} & \left(\tilde{N}_K\left(F_K^l - F_K^l(x_K)\right)\right)_{,x} \end{bmatrix}. \tag{2.23}$$

By substituting the defined displacement and the strain approximation into the weak form solution (2.12), the standard discrete system of equations will be obtained

$$Kd = f^{ext}, \tag{2.24}$$

Where d is the array of nodal displacements, and K is the global stiffness matrix, defined as

$$K = \int_{\Omega^h} \overline{B}^T C \overline{B} \, d\Omega, \tag{2.25}$$

where C is the elasticity tensor (equation 2.7).

The expression for external forces, which includes cohesive forces and inside crack forces, is

$$f_I^{ext} = \{f_I^u; f_J^a; f_K^{b1}; f_K^{b2}; f_K^{b3}; f_K^{b4}\}, \tag{2.26}$$

where

$$f_I^u = \int_{\Gamma_t} N_I \bar{t} \, d\Gamma + \int_\Omega N_I b \, d\Omega, \tag{2.27}$$

$$f_J^a = \int_{\Gamma_t} \tilde{N}_J\left(H - H(x_J)\right)\bar{t} \, d\Gamma + \int_\Omega \tilde{N}_J\left(H - H(x_J)\right)b \, d\Omega, \text{ and} \tag{2.28}$$

$$f_K^{bl}\Big|_{l=1,2,3,4} = \int_{\Gamma_t} \tilde{N}_K\left(F^l - F^l(x_K)\right)\bar{t} \, d\Gamma + \int_\Omega \tilde{N}_K\left(F^l - F^l(x_K)\right)b \, d\Omega. \tag{2.29}$$

The essential boundary conditions can be enforced directly on the vector d in a similar manner to classic FEM. Additionally, the geometry of the crack system is represented by explicit discretization. Since cracks geometry is updated every time step

this process needs to be repeated. This methodology is similar to the modified level set method used by Sukumar et al. (2001).

2.5 Element Integration

F-enriched nodes around the crack tips are enriched with non-linear, singular terms (equations 2.15-2.18), and this can lead to inaccuracies in results. To remedy this issue, two strategies were used: 1) element partitioning to increase numerical integration accuracy, 2) adding extra F-enriched nodes beyond the immediate tip element.

In XFEM, element partitioning is implemented exclusively for the sake of numerical integration, no additional degrees of freedom are introduced into the system/discrete space. Because nonlinear F-enriched terms are located in areas of high displacement gradient, they require higher order precision for numerical integration in order to prevent numerical inaccuracies. For this purpose, the elements cut by cracks are partitioned into sub-elements, and numerical integration is done separately within each of these sub-domains (Figure 2.2). Additionally, higher numbers of Gaussian quadrature points for numerical integration were tried to achieve an acceptable accuracy within economic computational effort. Finally, 19 Gauss quadrature points were chosen for the numerical integration scheme.
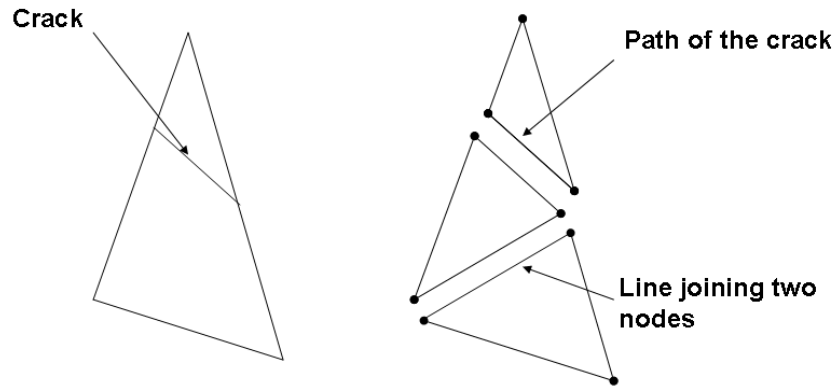
Figure 2.2: Triangular partitioning of elements cut by crack for numerical integrations.

As noted, the nodes of the elements containing the fracture tip are enriched with Westergaard functions, but this enrichment is not enough to obtain high numerical accuracy for displacement and displacement gradients (stresses) near the crack tip. It may lead to drastic numerical errors in partially F-enriched elements. A Partially F-enriched element is one for which only some nodes are F-enriched. These partially F-enriched elements surround the crack tip. Accuracy of results in the near-tip elements is of significant importance as they are used in contour integral methods to calculate the stress intensity factor at the crack tips that will be discussed in the next section.

Partially F-enriched elements do not satisfy the partition of unity principle, on which X-FEM is built. This problem may lead to degraded convergence rate. To avoid this problem, tip enrichment (F-enrichment) is not only used for crack-tip elements but

also for all the nodes within a certain radius, r_f from the crack tip. This effect is more prominent in cases where the crack faces are not traction free. Since the hydraulic fracturing problem involves loading on crack faces, this issue is of great importance for the problems studied in this research. By considering the extra tip enrichment, more precise values for the stresses near the tips and tractions at the crack surfaces are achieved. There are other different approaches to avoid this issue, such as the discontinuous Galerkin method or assumed strain method (Gracie et al. 2008).

Figure 2.3 shows how a large number of enriched nodes are introduced around the crack tip to remove the jump in the transient elements, and thus reducing the error in near tip calculations. The physical interpretation of this phenomena is that the nonlinear behavior of displacement and displacement gradients are not just limited to the crack tip element but extend to a distance from the crack tip.
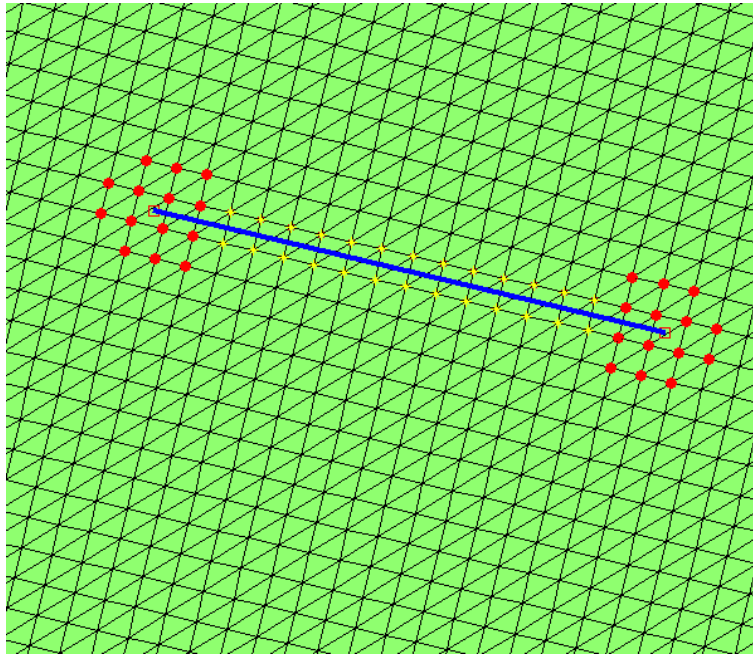
Figure 2.3: Using larger number of enriched nodes around the crack tip removes the jump in the transient elements and thus reduces the error in near tip calculations.

2.6 Stress Intensity Factor Calculations

Crack propagation analysis requires the evaluation of the parameters such as the energy release rate and stress intensity factors (SIF) to determine the length, velocity and orientation of the crack propagation. The stress intensity factor is used in fracture mechanics to more accurately predict the stress state ("stress intensity") near the tip of a crack caused by loads. In other words, the stress intensity factor is the magnitude of stress singularity at the crack tip (Anderson 1994). The magnitude of stress intensity factor depends on sample geometry, the size and location of the crack, and the magnitude and the modal distribution of loads on the material. The energy release rate for crack growth

or strain energy release rate is the change in elastic strain energy per unit area of crack growth.

The well-known criteria for crack propagation are maximum circumferential (hoop) stress (Erdogan and Sih 1963), maximum energy release rate (Nuismer 1975), and maximum strain energy density criterion (Sih 1974). All these criteria predict both the direction of propagation and the stress at which propagation would occur. They forecast slightly different angles for the initial kink, but they all predict kink initiation. Because of the abrupt change in tangent direction at the kink points, the direction that locally releases the maximum energy or satisfies some other mixed mode criterion, do not necessarily coincide with $K_{II} = 0$ for the incipient kink (Cotterell and Rice 1980). Cotterell and Rice showed that Erdogan and Sih (1963) criterion is a more realistic criterion at the incipient kinks. Therefore, here the Erdogan and Sih (1963) criterion was used to determine crack growth orientation,

$$\theta = 2 \arctan\left(\frac{1}{4} \left(K_I/K_{II} \pm \sqrt{(K_I/K_{II})^2 + 8} \right) \right),$$ (2.30)

where θ is the crack growth angle in the crack-tip local coordinate system. The formula (2.30) gives two directions for crack propagation; the one with positive (tensile) hoop stress is acceptable.

Several techniques have been proposed in the literature to extract stress intensity factors using numerical results such as obtained using finite element or boundary element methods. Many of these methods are based on the J-integral (Rice, 1968) or one of its variations such as the M-integral or the domain equivalent integral (Moran and shih,

43

1987; Li et al. 1985). The interaction integral is a popular approach for the extraction of stress intensity factors. This method is derived from J-integral by considering auxiliary fields. Both methods are discussed in detail in the next subsection. In addition to these methods, two other methods for stress intensity factor calculations were introduced for the first time in the framework of extended fintie element methods.

The Contour Integral Method (CIM) and the Cutoff Function Method (CFM) are superconvergent techniques proposed by Szabo and Babuska (1988) for the calculation of the stress intensity factors. These methods were originally introduced in the context of the p-version of the finite element method (a version of the finite element methods that tries to optimize numerical accuracy by increasing the order of test functions), but they can be adapted to the partition of unity methods as well. The CIM and the CFM are called superconvergent methods because the associated results converge to exact values of stress intensity factors as fast as the strain energy converges to its exact value. These methods are based on the computation of a functional from the finite element solution and the so-called extraction function. In the CIM, only the numerical solution for displacements is utilized for the related functional computations. For this reason, the CIM is in general more accurate than similar methods. On the other hand, CFM does not require any information on the derivative of displacements, and in this sense its implementation time is shorter than for other methods. These advantages make CFM and CIM good candidates for the purpose of SIF calculations especially in cases, where there is a loading on fracture surfaces such as a fluid pressure, because they involve less computations.

2.6.1. The Interaction Energy Integral Method

The most common way to obtain stress intensity factors is by using the J-integral and its variations. In linear elasticity, the general form of the J-contour integral for a crack in the presence of tractions on the crack faces is given by:

$$J = \int_{\Gamma \cup \Gamma_{c^+} \cup \Gamma_{c^-}} (\frac{1}{2}\sigma_{ik}\varepsilon_{ik}\delta_{1j} - \sigma_{ij}u_{i,1})n_j ds .$$ (2.31)

The coordinate system is centered on the crack tip with the x_1 axis tangent to the crack at the tip (as shown in Figure 2.4a). n_j is the jth component of the outward normal vector to the closed contour $\Gamma \cup \Gamma_{c^+} \cup \Gamma_{c^-}$, and δ_{ij} is the Kronecker delta which is one when $i = j$ and otherwise is zero. $u_{i,1}$ is the derivative of the displacements at node i with respect to x_1-axis. The J-integral is path independent and due to the singularity at the crack tip, integral (2.31) is not trivial and measures the strength of the singularity at the crack tip. Irwin showed that for a linear elastic material, the quantity J is equal to strain energy release rate

$$J = \frac{K_I^2}{E^*} + \frac{K_{II}^2}{E^*} ,$$ (2.32)

where $E^* = E$ for plane stress (E is Young's modulus) and $E^* = E/(1-v^2)$ for plane strain (where v is the Poisson's ratio).

Using the divergence theorem, the equation (2.31) may be converted to a domain integral (Rice, 1968) as

45

$$J = \int_A (\sigma_{ij} u_{i,1} - \frac{1}{2} \sigma_{ik} \varepsilon_{ik} \delta_{1j}) q_{,j} dA + \int_{\Gamma_{c^+} \cup \Gamma_{c^-}} (\frac{1}{2} \sigma_{ik} \varepsilon_{ik} \delta_{1j} - \sigma_{ij} u_{i,1}) q n_j ds, \qquad (2.33)$$

where $q_{,i}$ is the derivative of the weight function, q (shown in Figure 2.4) with respect to local x_i-axis. Using weight function limits area integration (first integral in equation 2.33)to the contour elements (shown in Figure 2.4) that makes this method more convenient for FEM purposes. It is not possible to decompose the value of J into the explicit stress intensity factors K_I and K_{II} as shown in equation 2.32 in situations of mixed mode loading (i.e., both K_I and K_{II} are non-zero). However, it is possible to separately extract the stress intensity factors by using auxiliary states. Consider state 1 $(\sigma_{ij}^{(1)}, \varepsilon_{ij}^{(1)}, u_i^{(1)})$ to correspond to the given state of the stress and state 2 $(\sigma_{ij}^{(2)}, \varepsilon_{ij}^{(2)}, u_i^{(2)})$ to be the auxiliary state. This auxiliary state is generated based on the asymptotic field for pure mode I or pure mode II. Using superposition, the J-integral for the sum of the two states can be written as

$$J^{(1,2)} = (\frac{(K_I^{(1)} + K_I^{(2)})^2}{E^*} + \frac{(K_{II}^{(1)} + K_{II}^{(2)})^2}{E^*}). \qquad (2.34)$$

On the other hand, one may decompose $J^{(1,2)}$ to states (1) and (2),

$$\begin{aligned} J^{(1,2)} &= J^1 + J^2 + I^{1,2} \\ &= (\frac{(K_I^{(1)})^2}{E^*} + \frac{(K_{II}^{(1)})^2}{E^*}) + (\frac{(K_I^{(2)})^2}{E^*} + \frac{(K_{II}^{(2)})^2}{E^*}) + \frac{2}{E^*}(K_I^{(1)} K_I^{(2)} + K_{II}^{(1)} K_{II}^{(2)}). \end{aligned} \qquad (2.35)$$

The interaction integral is defined as

$$I^{1,2} = \frac{2}{E^*}(K_I^{(1)} K_I^{(2)} + K_{II}^{(1)} K_{II}^{(2)}). \qquad (2.36)$$
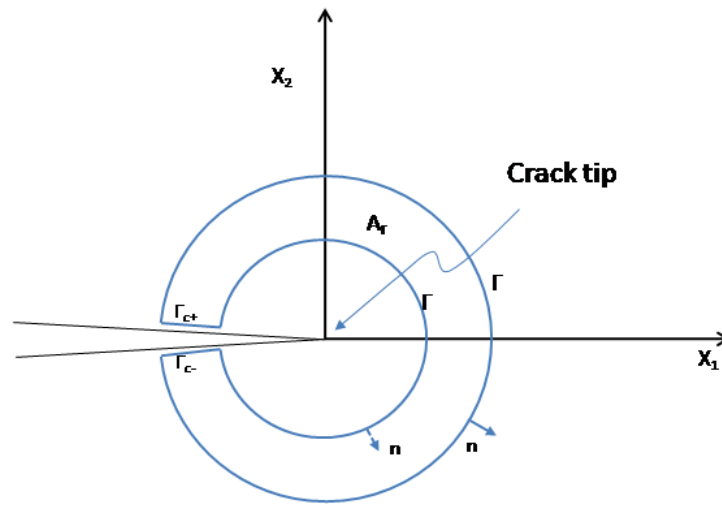
(a)
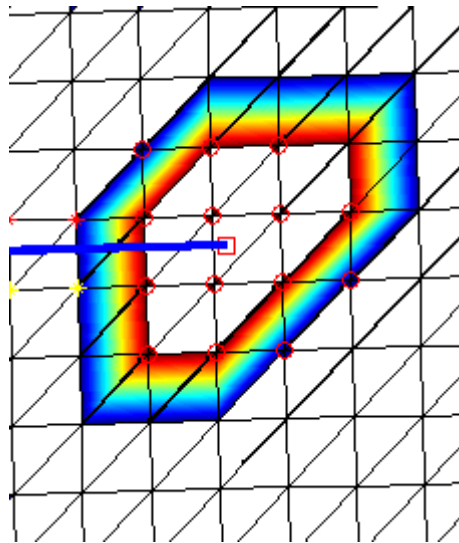
(b)

Figure 2.4: (a) The contour and domain to compute the J-integral and interaction integral. (b) The contour around a crack tip for the contour integral calculations in the presented model for triangular elements. The color shows the values of the weight function which varies from zero (blue) to one (red).

Inserting the J-integral sum (2.35) into the J-integral formula (2.33) and using the definition (2.36) for the interaction integral results in

$$I^{1,2} = \int_A (\sigma_{ij}^{(1)} u_{i,1}^{(2)} + \sigma_{ij}^{(2)} u_{i,1}^{(1)} - \sigma_{ik}^{(1)} \varepsilon_{ik}^{(2)} \delta_{1j}) q_{,j} dA +$$
$$\int_{\Gamma_{c^+} \cup \Gamma_{c^-}} (\sigma_{ik}^{(1)} \varepsilon_{ik}^{(2)} \delta_{1j} - \sigma_{ij}^{(1)} u_{i,1}^{(2)} - \sigma_{ij}^{(2)} u_{i,1}^{(1)}) q n_j ds. \tag{2.37}$$

Choosing the auxiliary state as the pure mode I asymptotic field (i.e., $K_I^{(2)} = 1, K_{II}^{(2)} = 0$), K_I can be extracted as

$$K_I^{(1)} = \frac{E^*}{2} I^{(1, Mode\, I)}. \tag{2.38}$$

Using the pure mode II state (i.e., $K_I^{(2)} = 0, K_{II}^{(2)} = 1$), $K_{II}^{(1)}$ can be similarly extracted. This method requires the calculation of both displacement gradients and stresses, which makes the process lengthy and time-consuming.

2.6.2. Displacement Interpolation Method

A simpler and computationally less expensive way to calculate stress intensity factors is to compare the crack tip stress or displacement field with the asymptotic forms. The displacements on a line ahead of the crack tip ($\theta = \pi$) are given by (Anderson, 1994)

$$
\begin{bmatrix} u_1(r,\pi) \\ u_2(r,\pi) \\ u_3(r,\pi) \end{bmatrix} = \sqrt{\frac{r}{2\pi}} \begin{bmatrix} -\dfrac{4K_{II}}{E^*} \\ \dfrac{4K_I}{E^*} \\ -\dfrac{K_{III}}{G} \end{bmatrix},
\tag{2.39}
$$

which implies that displacements near the crack tip depend on SIF.

The crack opening displacement (COD) can be extracted directly from equation (2.13) by subtracting displacements of the fracture surfaces from each other

$$
[u^h] = 2\sum_{I \in W} a_I \widetilde{N}_I + 2\sqrt{r}\sum_{I \in W} b_I \widetilde{N}_I.
\tag{2.40}
$$

The above equation gives COD for both linear and quadratic elements. The accuracy problem of this method deteriorates in the case of multiple fracture tip interaction, and led us to neglect this method and resort to other available methods.

Later, formula (2.40) is used to calculate fracture width for solving fluid flow equation in Chapter 4.

2.6.3. The Cutoff function Method (CFM)

The same extracion functions are used in the cutoff function method and contour integral methods. The so-called extraction functions for mode I and mode II are defined respectively as (Szabo and Babuska, 1991)

$$
\mathbf{v^{-I}} = \frac{B^{-I}}{2G\sqrt{2\pi}}\frac{1}{\sqrt{r}} \begin{bmatrix} (k-\dfrac{3}{2})\cos\dfrac{\theta}{2} + \dfrac{1}{2}\cos\dfrac{5\theta}{2} \\ -(k+\dfrac{3}{2})\sin\dfrac{\theta}{2} + \dfrac{1}{2}\sin\dfrac{5\theta}{2} \end{bmatrix}
\tag{2.41}
$$

49

and

$$\mathbf{v}^{-\mathbf{II}} = \frac{B^{-II}}{2G\sqrt{2\pi}} \frac{1}{\sqrt{r}} \begin{bmatrix} -(k+\frac{1}{2})\sin\frac{\theta}{2} - \frac{1}{2}\sin\frac{5\theta}{2} \\ -(k-\frac{1}{2})\cos\frac{\theta}{2} + \frac{1}{2}\cos\frac{5\theta}{2} \end{bmatrix}, \tag{2.42}$$

where $B^{-I} = B^{-II} = -2G/(1+k)$, G being the elastic shear modulus and k is $3-4v$ for the plane strain condtion and $(3-v)/(1+v)$ for the plane stress condition. The extraction function for each mode is defined as the negative of the eigenvalue of the asymptotic expansion of the stress field associated with that mode. Derivation of these equations can be found in Szabo and Babuska (1991). These functions do not have finite strain energy in any arbitrary domain Ω containing the crack tip (shown in Figure 2.5). However, they have finite strain energy in donut-shape subdomains, Ω^*, which does not contain the fracture tip (Figure 5). The local character of the extraction function is preserved around the crack tip hence $\phi(r)$ is equal to 1 inside the inner ring (Figure 5) and is zero out of the exterior ring,

$$\begin{aligned} w^{-I}(r,\theta) &= \Phi(r)v^{-I}(r,\theta) \\ w^{-II}(r,\theta) &= \Phi(r)v^{-II}(r,\theta) \end{aligned}. \tag{2.43}$$

The cutoff function is defined by (Szabo and Babuška, 1991)

$$\Phi(r) \equiv \begin{cases} 1 & r \le \rho_1 \\ 1-3\left(\frac{r-\rho_1}{\rho_2-\rho_1}\right)^2 + 2\left(\frac{r-\rho_1}{\rho_2-\rho_1}\right)^3 & \rho_1 \le r \le \rho_2 \\ 0 & \rho_2 \le r \end{cases}. \tag{2.44}$$

50
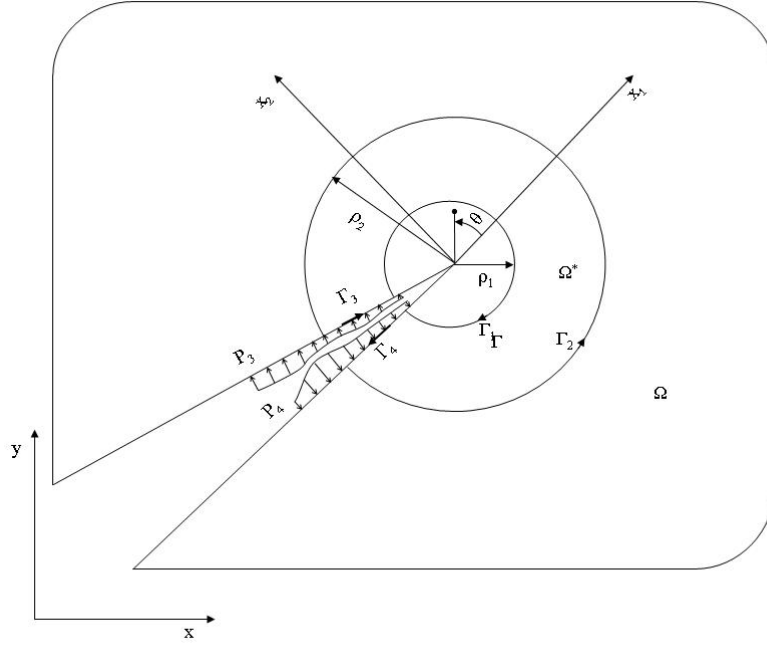
Figure 2.5: Coordinate systems and integration contours for superconvergent extraction methods.

The function $\Phi(r)$ varies smoothly from 1 to 0 between ρ_1 and ρ_2, and its derivative is zero at these points.

By applying boundary conditions on the corresponding tractions, it is possible to describe the stress intensity factors as

$$
\begin{aligned}
K_I = \quad & \int_{\Omega^*} \sigma_{kl,l}^{(w^{-I})} u_k d\Omega + \int_{\Gamma_3} p_i^3 w_i^{-I} d\Gamma + \int_{\Gamma_4} p_i^4 w_i^{-I} d\Gamma \\
& - \int_{\Gamma_3} T_k^{(w^{-I})} u_k d\Gamma - \int_{\Gamma_4} T_k^{(w^{-I})} u_k d\Gamma
\end{aligned}
\tag{2.45}
$$

and

$$
\begin{aligned}
K_{II} = \quad & \int_{\Omega^*} \sigma_{kl,l}^{(w^{-II})} u_k d\Omega + \int_{\Gamma_3} p_i^3 w_i^{-II} d\Gamma + \int_{\Gamma_4} p_i^4 w_i^{-II} d\Gamma \\
& - \int_{\Gamma_3} T_k^{(w^{-II})} u_k d\Gamma - \int_{\Gamma_4} T_k^{(w^{-II})} u_k d\Gamma
\end{aligned} \quad ,
\tag{2.46}
$$

where p_i^3 and p_i^3 are prescribed tractions on crack faces Γ_3 and Γ_4 (shown in Figure 2.5), respectively. It is important to note that $\boldsymbol{P^3}$ and $\boldsymbol{P^4}$ are vectors with both normal and shear components. In the above equations, $T_k^{(w)}$ is the k-th component of the traction vector corresponding to displacement w and defined by

$$T_i^{(u)} = \sigma_{ij}^{(u)} n_j. \tag{2.47}$$

It can be seen that equations (2.45) and (2.46) unlike equation (2.37) do not require calculating stresses or displacement derivatives. That means fewer computations and faster calculation of stress intensity factors.

2.6.4. The Contour Integral Method (CIM)

The Contour Integral Method (CIM) is another superconvergent extraction method used in this research. This class of methods is based on developing and computing a functional from finite element solutions. The functional can be a stress at a point or a stress intensity factor. These methods were originally developed by Babuŝka and Miller (1984) based on the extraction functions introduced in (2.41) and (2.42). The derivation process is simillar to CFM, but no filter functions, such as $\varPhi$, will be introduced. The details for derivation can be found in Pereira and Duarte (2006). The final formulae are

$$\begin{aligned} K_I = \quad & \int_{\Gamma_3} p_i^3 v_i^{-I} d\Gamma + \int_{\Gamma_4} p_i^4 v_i^{-I} d\Gamma \\ & + \int_{\Gamma_2} T_i^{(u)} v^{-I} d\Gamma - \int_{\Gamma_2} T_k^{(v^{-I})} u_k d\Gamma \end{aligned} \tag{2.48}$$

$$K_{II} = \int_{\Gamma_3} p_i^3 v_i^{-II} d\Gamma + \int_{\Gamma_4} p_i^4 v_i^{-II} d\Gamma$$
$$+ \int_{\Gamma_2} T_i^{(u)} v^{-II} d\Gamma - \int_{\Gamma_2} T_k^{(v^{-II})} u_k d\Gamma. \tag{2.49}$$

CIM have the same advantages that CFM have over J-integral methods. It means that it does not require computing displacement derivatives or calculating stresses. What makes CIM more attractive than CFM is the fact that it is only necessary to calculate a contour integral rather than area integrals. This difference can save CPU time without loosing accuracy, as the two methods produce results with comparable accuracy.

2.7. Fracture Coalescence

Crack coalescence can introduce difficulties in the numerical implementation of the presented model, and thus some special conditions or procedures need to be defined for approaching and intersecting crack tips (Figure 2.6). When the distance between a growing crack tip and a piece of another crack is less than the minimum admissible crack length increment, the cracks are considered to be intersected. The tip enrichment must be removed from the element containing the intersection point but there is still a need for a step function enrichment representing the crack body. Consequently, a new modified step function enrichment must be added to the elements at crack intersections.

When two cracks are joined, the crack tip enrichment of the approaching tip is removed. By using the sign distance function (which is equal to +1 on one side of the fracture and -1 on the other side of the fracture) of the pre-existing fracture (master crack) $f_1(X)$ and approaching crack (minor crack) $f_2(X)$, the signed distance function (step

53

function) of the approaching crack is modified (see Figure 2.7). Three different

subdomains will be created: $(f_1 < 0, f_2 < 0)$, $(f_1 > 0, f_2 > 0)$ and $(f_1 > 0, f_2 < 0)$. The

signed distance function of the minor crack of a point X will be modified as:

$$\overline{J}(X) = \begin{cases} H(f_1(X)) - H(f_1(X_J)) & f_1(X_J).f_1(X) > 0 \\ H(f_2(X)) - H(f_2(X_J)) & f_1(X_J).f_1(X) < 0 \end{cases} \qquad (2.50)$$

where H_J is a point located on the side of the master crack on which the minor crack

does not exist. The function $J(X)$ models that the approaching crack 2 is arrested on the

other crack 1. The displacement in the element containing the intersection is
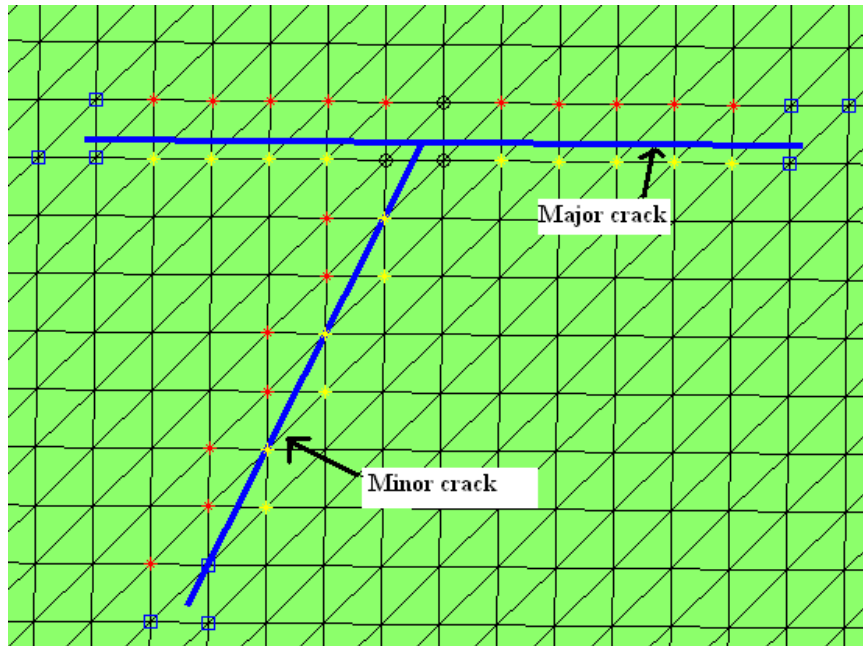
Figure 2.6: The junction of two cracks occurs when one crack approaches and eventually touches the other. The tip enrichment of the approaching crack is removed after the two cracks junction, and the connection of two cracks is modeled by a junction enrichment function J (black circle nodes). The enrichment for the nodes whose supports are cut by two or more discontinuities is explained in the text.

$$u^e(x) = \sum_{I \in J_e} N_I(x)u_I + \sum_{J \in J_e} \tilde{N}_J(x)a_J^m \overline{J}_J^m + \sum_{J \in J_e^M} \tilde{N}_J(x)a_J^M \overline{H}_J^M . \tag{2.51}$$

Since enrichment of the crack intersections requires higher nodal degrees of freedom, the finite element code's data structure should be adjustable to this issue. In addition, the preprocessing components should be able to identify crack intersections to be able to assign the appropriate type of enrichments.
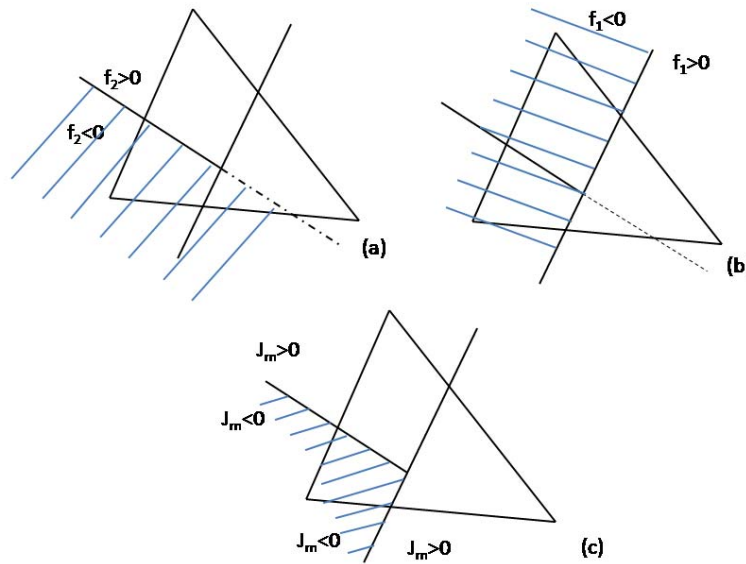
Figure 2.7: The signed distance functions for minor (Figure a) and major (Figure b) fractures. The minor fracture is the fracture joining an existing fracture. The new signed distance function for the intersection is shown in part c.

It is notable that it is required to avoid the creation of a rigid body mode by preventing cracks to intersect each other twice. If two cracks are already intersected or intersected to common cracks, they cannot be joined again because it will lead to

instability due to the loss of the constraint. In such cases, the approaching tip is deactivated for further growth. Figure 2.8 shows a potential case, which may lead to a double intersection in the next steps, unless one of the tips freezes.
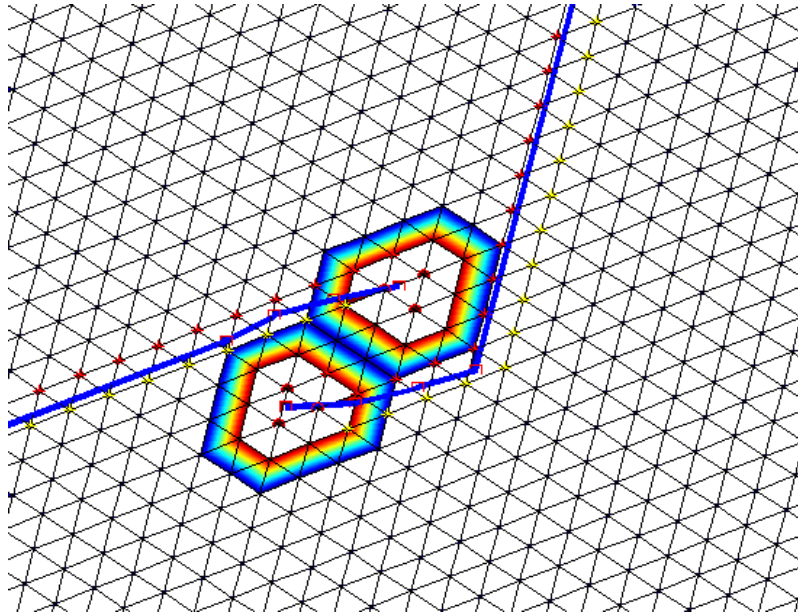
Figure 2.8: Two approaching cracks before intersection.

2.8. Convergence Test

The XFEM method described above has been implemented in Matlab-based code. The convergence and discretization error are tested by several examples. To check the solution convergence, a measure should be defined. This measure also indicates the magnitude of the discretization error. It is possible to use stress intensity factors as a measure for the solution convergence, but stress intensity factor calculations may involve

some additional inaccuracy, in addition to that, it provides information about near crack tip accuracy not the whole domain. For this purpose, the normalized energy error norm is used. The normalized energy error norm is computed by

$$\text{Energy error } = \frac{W(\varepsilon - \varepsilon^h)}{W(\varepsilon)},$$ (2.48)

where W is

$$W(\varepsilon) = \left(\frac{1}{2} \int_\Omega \varepsilon : \mathbf{C} : \varepsilon \, d\Omega \right)^{\frac{1}{2}},$$ (2.49)

Where $\mathbf{C}$ is the elasticity matrix, ε is the exact strain field and ε^h is the approximate strain field computed using the finite element solution. In case no analytical solution is available, it is possible to use total elastic energy to measure the convergence rate and posteriori error.

2.10. Numerical Examples

To validate the accuracy of the model, numerical results have been compared to examples of available analytical solutions in the literature. Additionally, using the methodology introduced in the previous section, the convergence of results for different cases are compared to each other. Crack opening displacements, the stress intensity factors and the energy error are calculated and compared with analytical or bench mark solutions available in the literature. The results of linear and quadratic XFEM are also

compared. Finally, results of different techniques for stress intensity factors are compared and discussed.

The first example is an infinite plane containing a crack with length 2a under uniform remote stress field, σ. This problem has a closed form stress solution (Westergaard 1939) of,

$$\begin{Bmatrix} \sigma_x \\ \sigma_y \\ \tau_{xy} \end{Bmatrix} = \begin{Bmatrix} ReZ_I - y\, ImZ_{I'} \\ ReZ_I + y\, ImZ_{I'} \\ -y\, ReZ_{I'} \end{Bmatrix} + \begin{Bmatrix} 2\, ImZ_{II} + y\, ReZ_{II}' \\ -y\, ReZ_{II}' \\ ReZ_{II} - y\, ImZ_{II}' \end{Bmatrix}, \tag{2.50}$$

where (Irwin 1957, 1958, Paris 1965 etc)

$$Z_I(z) = \frac{\sigma}{\sqrt{1-(a/z)^2}}, \tag{2.51}$$

$$Z_{II}(z) = -i\frac{\sigma}{2}, \tag{2.52}$$

and $z = x + iy$. The closed form displacement field is

$$2G\begin{Bmatrix} u \\ v \end{Bmatrix} = \begin{Bmatrix} (\beta-1)\, Re\overline{Z}_I - y\, ImZ_I \\ \beta\, Im\overline{Z}_I - y\, ReZ_I \end{Bmatrix} + \begin{Bmatrix} \beta\, Im\overline{Z}_{II} + y\, ReZ_{II} \\ -(\beta-1)\, Re\overline{Z}_{II} - y\, ImZ_{II} \end{Bmatrix}, \tag{2.53}$$

where β is defined as

$$\beta = \begin{cases} 2(1-v) & \text{planestrain} \\ 2/(1+v) & \text{planestress} \end{cases}. \tag{2.54}$$

Westergaard's solution is used to calculate displacements at the boundaries of the model, then the calculated displacements are applied as boundary conditions in order to generate results for an infinite plane. Using this strategy, the stress intensity factors (SIF)

calculated by the XFEM code should not depend on the size of the model and should be the same as SIF for the crack in an infinite plane.

The accuracy of displacement results for the XFEM implementation were examined using linear and quadratic elements in the mesh (Figure 2.9). For the quadratic element cases, the size of enrichment area was varied as well using $r_f = 1.5h$ and $r_f = 2.5h$, where h is the characteristic size of the elements (roughly, h is square root of element's area divided by two). This was done to evaluate the sensitivity of results with respect to the the size of enrichment area. The results show close agreement between all methods and the analytical results, but the quadratic elements with larger enrichment area ($r_f = 2.5h$) indicates the best agreement. Therefore, the rest of the tests were executed with the quadratic elements. Using quadratic elements improves the accuracy of the fracture opening profile, but there are still small purturbations in transient elements.

In Table 2.1, the effect of the radius of tip enrichment on the accuracy of resultant stress intensity factors were shown. The values shown for K_I are normalized with respect to the analytical solution. Larger enrichment radius leads to smooth displacement fields around the crack tip, thereby improving accuracy of stress intensity factors.

r_f	K_I
1.00 h	0.945102
1.50 h	0.977467
2.50 h	0.983202

Table 2.1: The effect of the radius of tip enrichment on the accuracy of the calculated stress intensity factors.
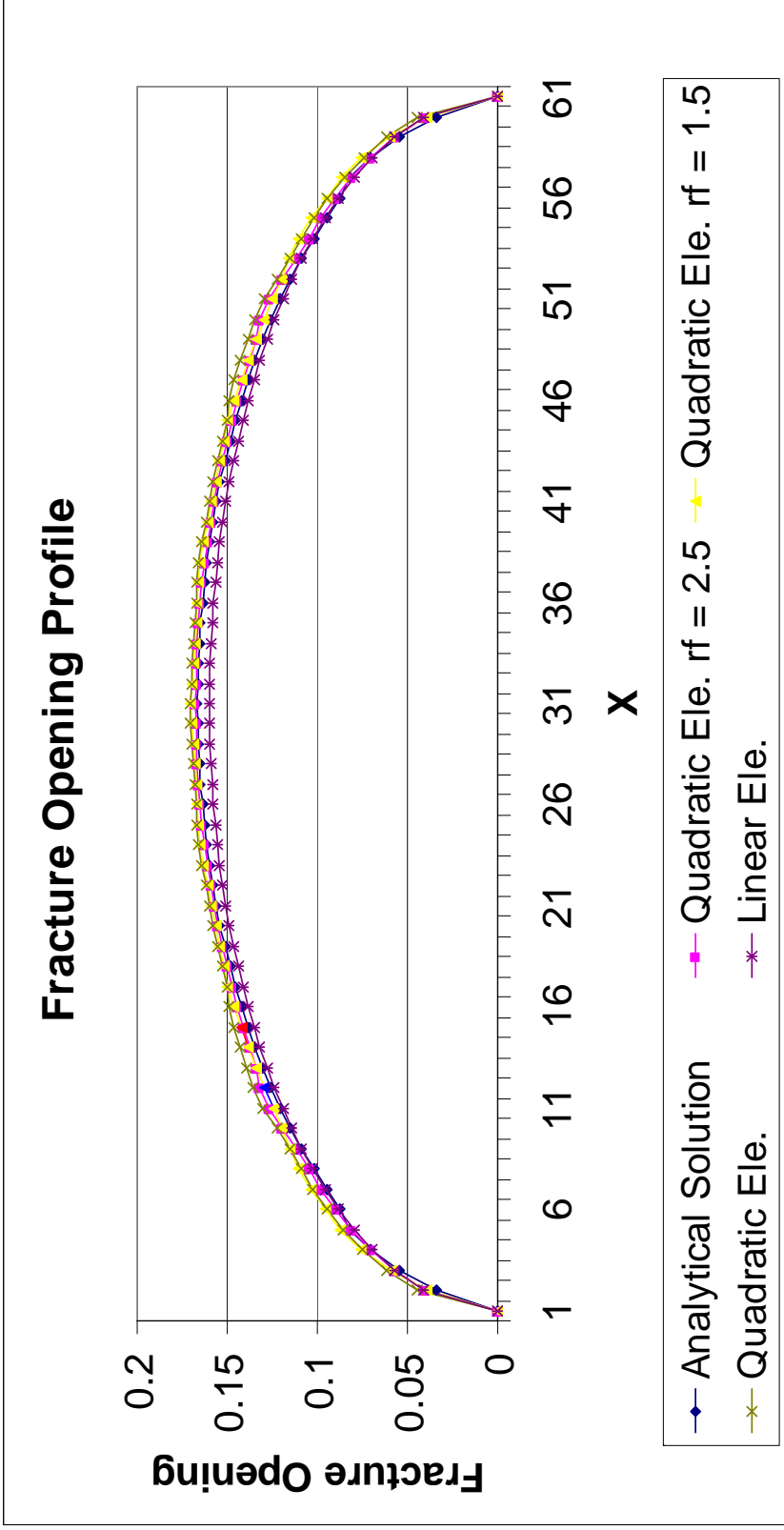
Figure 2.9: Fracture opening profile for different elements and different tip-enrichment radius. X is the coordinate axis along the fracture.

In Figure 2.10, different methods for stress intensity factor calculation are compared with each other. As noted, CIM and CFM have almost the same accuracy, but due to the computational simplicity of CIM, this method is chosen for most of the simulations presented in chapter 3 and chapter 4.

The error in energy (equation 2.48) is plotted for linear and quadratic XFEM in Figure 2.11. While the accuracy of quadratic elements is greater for crack opening displacements and J-integral values, the rate of the convergence is actually less than the case with the linear elements. This behavior, which is probably due to the singularity at the crack tip, has also been reported by Stazi et al. (2002). Figure 2.12 shows the convergence of the J-integral, which is proportional to the convergence of stress intensity factors at the tip. J-integral and stress intensity factors cannot be a good measure for convergence studies of the problem, because the methods for extracting these values add more error into the calculations. However, using CFM, more accurate results were obtained for stress intensity factors compared to the J-integral and inteaction integral method.

The case with multiple fractures growing under uniform far-field tension is shown in Figure 2.13. In the case where multiple fracture tips are propagating simultaneously, the crack tip with the greatest stress intensity factor will propagate for a distance equal to the pre-determined length increment. Other tips will propagate a distance proportional to the magnitude of their stress intensity factors.
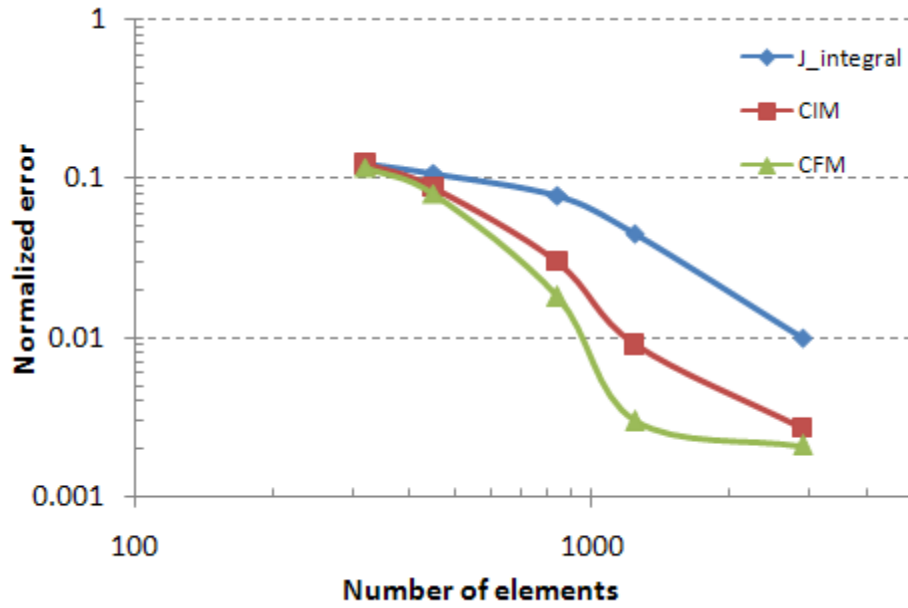
Figure 2.10: Different methods for stress intensity factor calculations are compared.
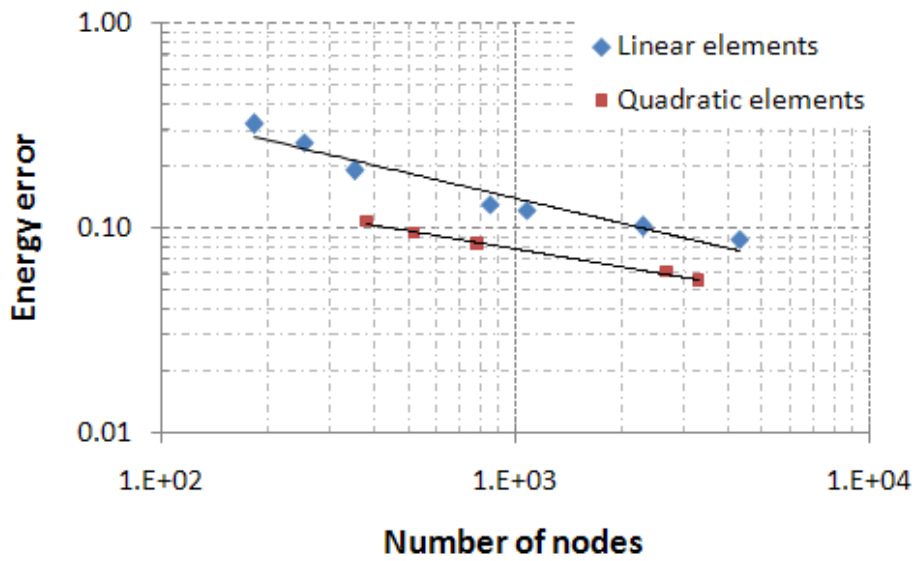
Figure 2.11: Energy error rates for linear and quadratic elements are shown.
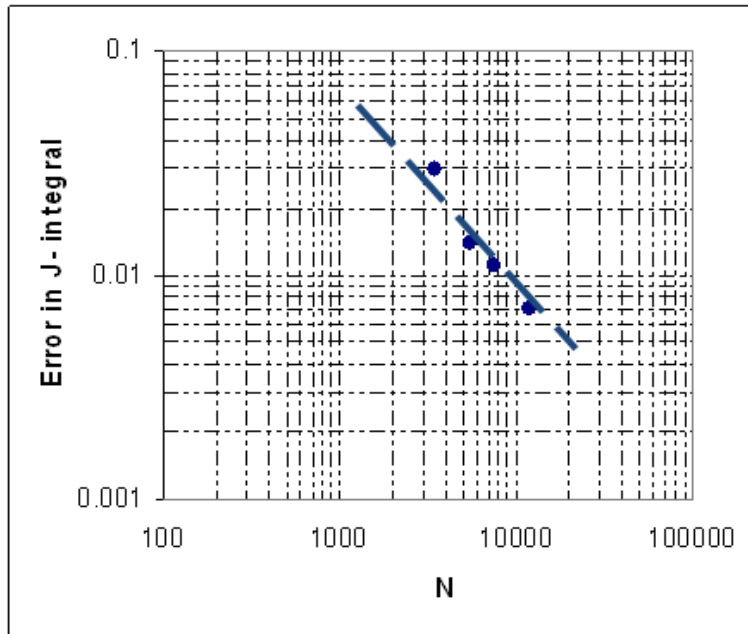
Figure 2.12: J-integral (energy release rate) error is plotted versus the number of nodes (*N*) for linear elements.
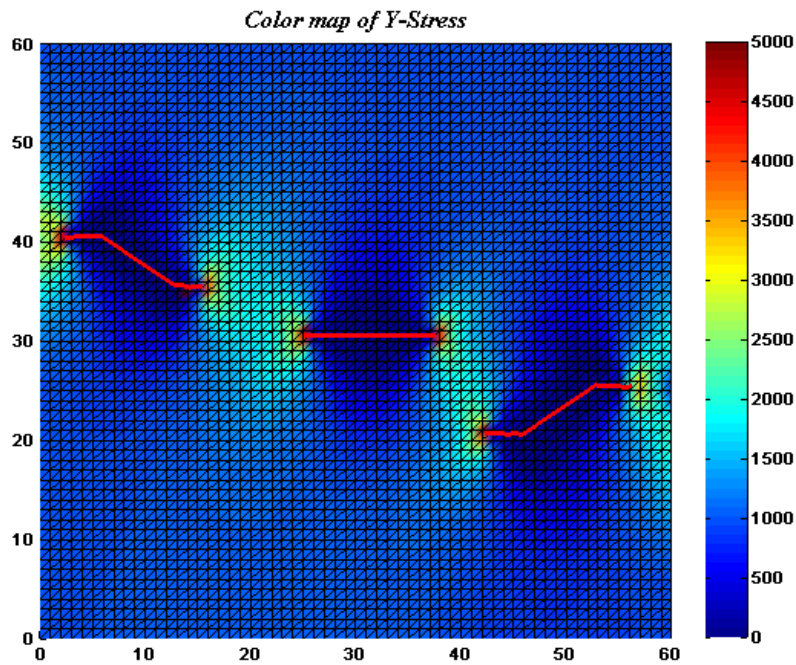
Figure 2.13: Modelling multiple crack propagation in XFEM. The specimen is under uniaxial tension in the vertical direction.

For the case of a pressurized crack in an infinite plane, the Westergaard functions are

$$
\begin{aligned}
Z_I(z) &= \frac{\sigma}{\sqrt{1-(a/z)^2}} - \sigma, \\
Z_{II}(z) &= 0.
\end{aligned}
\tag{2.55}
$$

Despite different stress fields, it can be shown by superposition that the values of stress intesity factors are the same as the last example.

In the hydraulic fracturing problem, fracturing fluid applies pressure as a distributed load on the fracture walls. It is of great importance to have accurate results for traction at the fracture walls. In the case that only tip elements are enriched with tip enrichment functions, it is not possible to honor the same traction at the fracture walls, where the traction is supposed to be equal to the applied pressure. In this situation, several jumps in traction may form along the fracture (Figure 2.14 and Figure 2.15). To avoid this problem, the radius of tip enrichment is increased to 2h (where h is the size of elements). But some small jumps may still exist that can be dissolved by mesh refinement in the vicinity of the fracture tip (Figure 2.16).
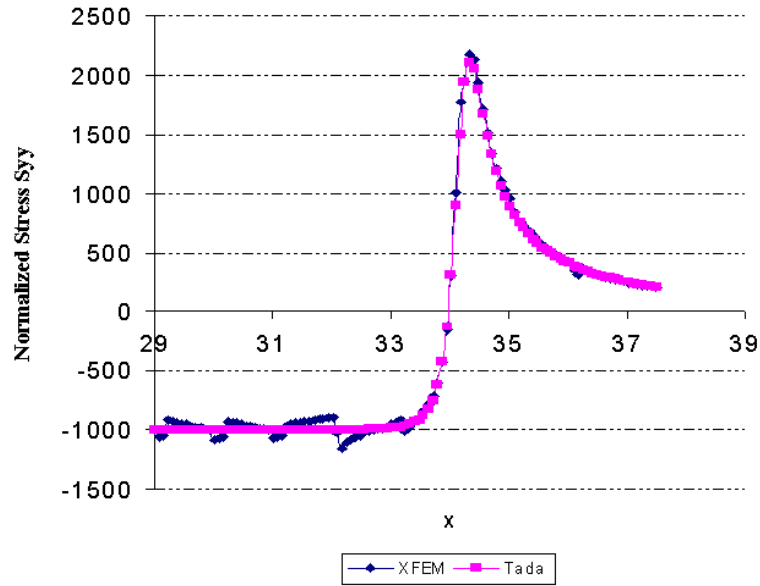
Figure 2.14: Stress discontinuities in transient element, due to the lack of satisfying partition of unity principles in these elements, is compared with analytical solution (in pink).Pressure inside the fracture is 1000, and there is no far field stress.
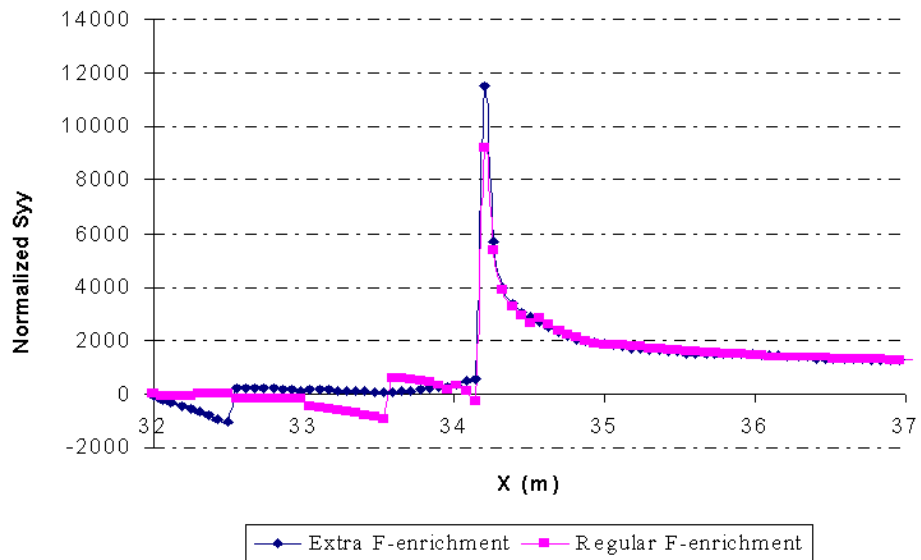
Figure 2.15: Effect of the radius of tip enrichment on the accuracy of traction and normal stress distribution.

65
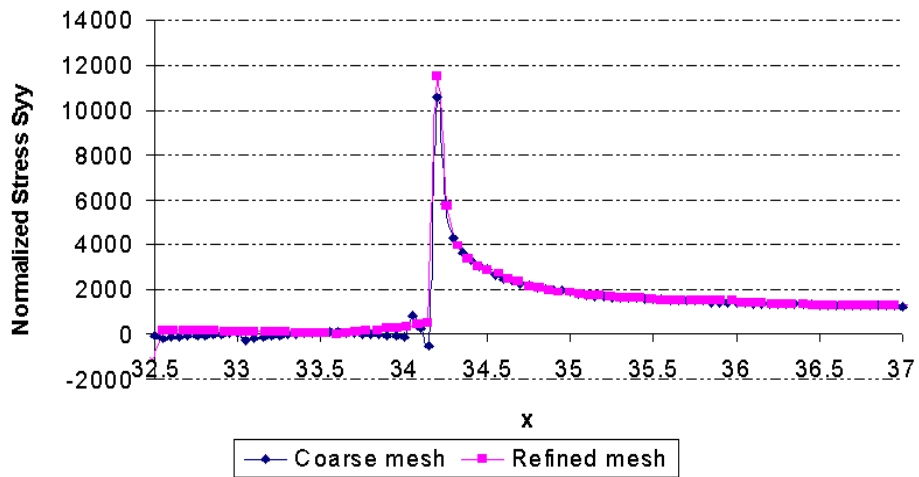
Figure 2.16: Effect of mesh refinement (in the presence of r-refinement) on the accuracy of traction and normal stress distribution.

Figure 2.17 shows the geometry of two intersected cracks. The crack opening profile for the minor crack is plotted in figure 2.18. There is a stress singularity at the intersection point; however, the order of this singularity, which will be discussed in chapter 3, is less than the fracture tip singularity. Therefore, the stress singularity at the intersections may cause some inaccuracy that will be decreased by decreasing the size of the elements near the intersection point. The effect of mesh refinement on the accuracy of the results is noticeable in this problem. Figure 2.19 shows a typical mesh refinement near the intersection points. The results were compared with results of ANSYS (commercial finite element package) to check the accuracy of results.

66
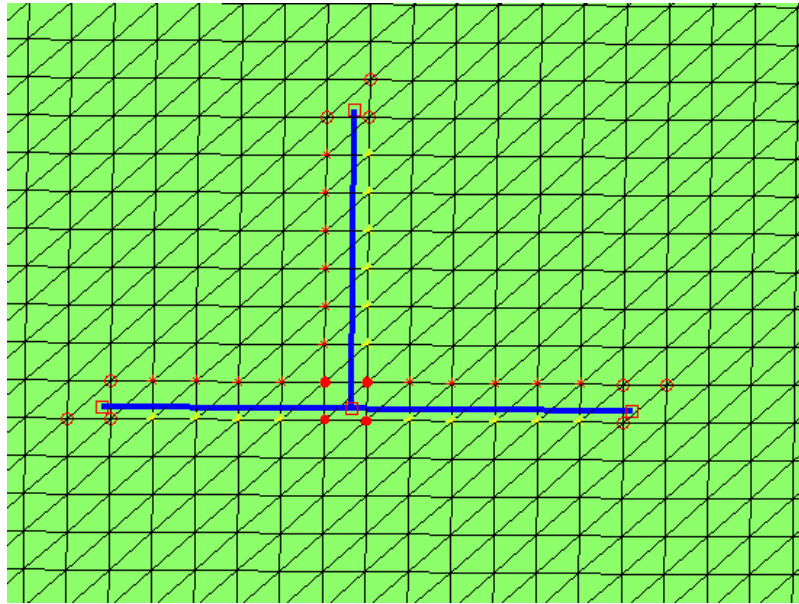
Figure 2.17: Nodal enrichment at a normal crack intersection. Four nodes (red solid circles) around the intersection point are enriched with the modified step function in equation (2.50).
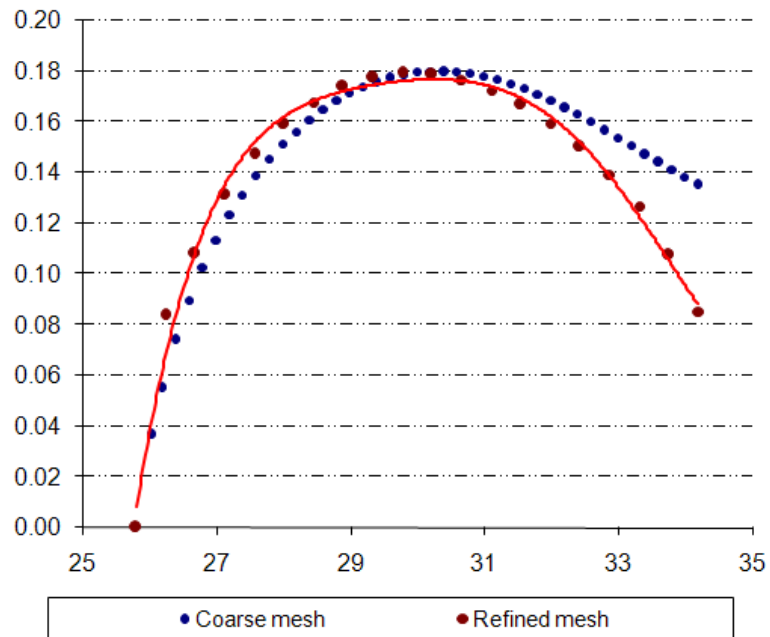
Figure 2.18: The crack opening profile for the minor crack of the intersected crack system shown in Figure 2.17. It can be seen that the results of the refined mesh shows a good agreement with ANSYS results (red continuous line).
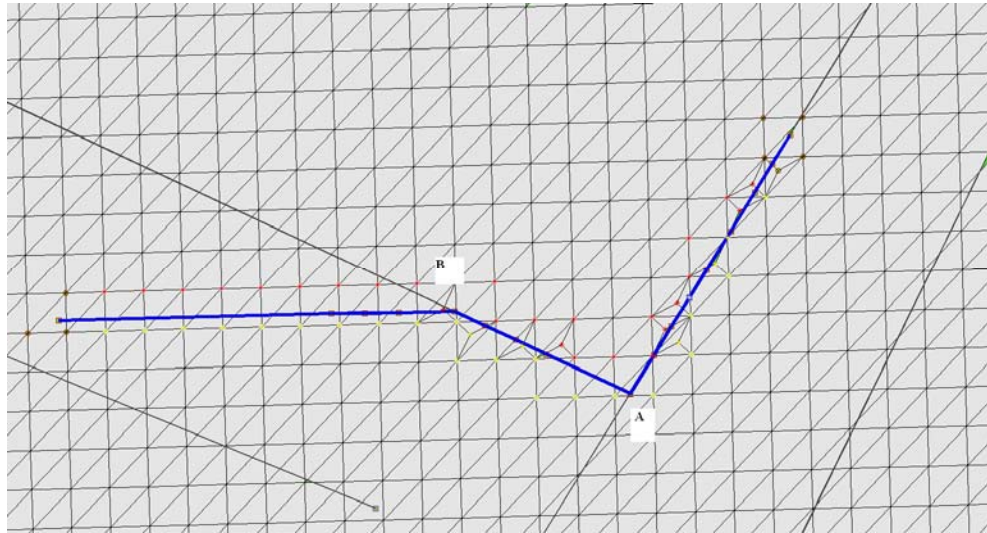
Figure 2.19: Example of mesh refinement near the points where fracture orientation makes abrupt changes at A and B.

The XFEM code is designed to handle multiple crack growth problems. For instance, Figure 2.20 shows the growth of two initially parallel fractures under the effect of remote tension, where two cracks evolve into an en-echelon geometry. In the case of multiple fractures, several fracture tips could be eligible to grow, but the length of the growth will be proportional to their associated stress intensity factors.
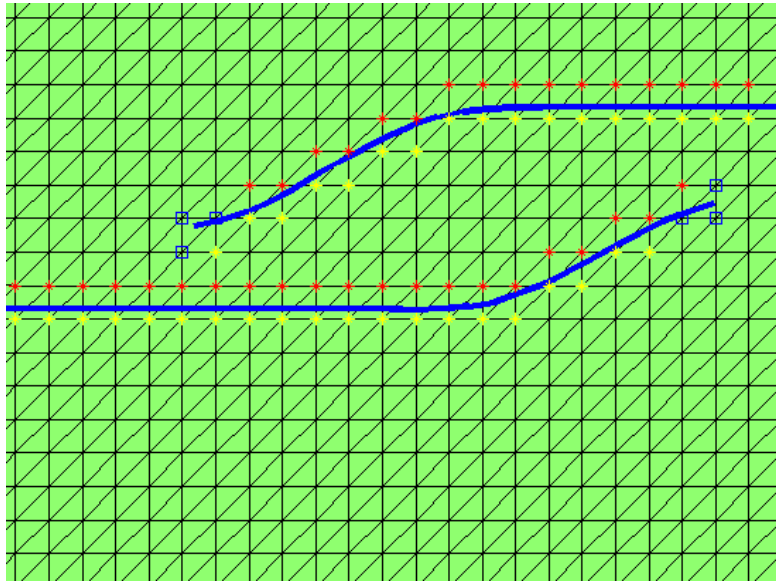
Figure 2.20: Two parallel fractures are growing under remote vertical tension.

2.11 Conclusion

In this chapter, the basis of the Extended Finite Element Methods (XFEM) for a general fracture propagation problem is explained. Methods for incorporating the near crack tip enrichment and the step function in the framework of extended finite element for linear and quadratic elements are described. The rate of convergence for these elements are compared to each other. The crack geometry is approximated by a signed distance function, which is a simplified version of the level set method. A new generalization for the signed distance function is introduced to incorporate fracture junctions. The new fracture junction function involves less degrees of freedom in comapre to the junction function introduced in Budyn et al. (2002). It was found that the effect of mesh size near the intersection point is crucial for the accuracy of results. So,

local mesh refinement capability is also added to the XFEM model to enhance numercial accuracy at the fracture junctions.

The CIM and CFM superconvergent methods are used for SIF calculations. It is the first time that these methods were applied in the XFEM framework. It was found that these methods give more accurate results in comparison to common techniques such as J-integral and interaction integrals. In addition, these methods are computationallt less expensive in compare to the other methods. To dissolve the inaccuracy caused by partially enriched elements, a larger radius for crack tip enrichment is used. This issue was crucial for accurate calculation of tractions and diplacement gradients near the fracture tip, because these items require more accuracy to achieve more precise results for SIF calculations.

Based on the concepts discussed, a computer code was developed that incorporates all the mentioned capabilities. Some modifications were also introduced to the XFEM model to facilitate handling the problems that will be discussed in the next chapters. The implementation was limited to six node triangle elements, but it can be developed to quadrilateral elements. At the end of the chapter, some numerical examples were implemented to demonstrate the robustness and accuracy of the model.

Chapter 3. Interaction Between Hydraulic Fractures and Natural Fractures

3.1. Introduction

Hydraulic fracturing is one of the main stimulating techniques to enhance recovery from tight naturally fractured reservoirs. In many regions, the orientation of current in-situ stresses has not changed from the time of the formation of the natural fractures (Laubach et al., 2004). Consequently, the hydraulic fracture is likely to be sub-parallel to the fractures with which it interacts. In other regions the natural fractures are a result of a totally different stress regime than the present day, so the natural fractures may be oblique or orthogonal to the hydraulic fracture path.

The Barnett Shale is an example of a naturally fractured gas formation that has recently generated great interest with regard to complex hydraulic fracture response. It is a laminated silicious mudrock with carbonate concretions (Loucks and Ruppel, 2007), where natural fractures are common. The fractures typically have narrow apertures (less than 0.05 millimeters) and are generally sealed by calcite (Gale et al. 2007) at least those found in cores. The origin of these opening-mode fractures could be tectonic paleostress, differential compaction, local effects of folding or major faults and sag features

associated with underlying karsts. Commercial production without stimulation has been achieved in a small fraction of shale wells that intercept natural fractures (Curtis, 2002). In most other cases, successful shale-gas production requires hydraulic fracturing to improve wellbore-to-natural fracture system communication, which eliminates the high near-wellbore pressure gradient. Additionally, coring has shown that hydraulic fractures have been diverted along and have propped pre-existing natural fractures (e.g. Hopkins et al., 1998 and Lancaster et al. 1992). Therefore, understanding the geometry and the growth process of hydraulic fractures and their interaction with natural fractures is important for designing, monitoring and assessing the induced fractures and their effects on the wellbore production.

Micro-seismic data collected during hydraulic fracture treatments for Barnett Shale wells reveals a complex geometry, where hydraulic fractures may propagate as multiple segments with different orientations influenced by pre-existing fractures, which lead to a cloud of epicenters. Although micro-seismic mapping provides insights on the interaction of hydraulic fracturing with natural fracture systems and stress regimes (Yingping et al. 1998), the phenomenon behind the scattered epicenters observed during fracture jobs are not fully explained (Rutledge and Phillips, 2003). Waters et al. (2006) provided a map (Figure 3.1) of the microseismic events generated during a staged hydraulic fracturing treatment. The microseismic does not show a narrow band perpendicular to the minimum horizontal stress, but there is a huge region of affected rock volume, extending hundreds to thousands of feet along the expected hydraulic fracture direction (parallel to the orientation of maximum horizontal stress). The cloud

also extends hundreds of feet in the orthogonal direction. Based on the evidence of complex fracture geometry, extended finite element method (XFEM) was used to investigate the mechanics of this process.
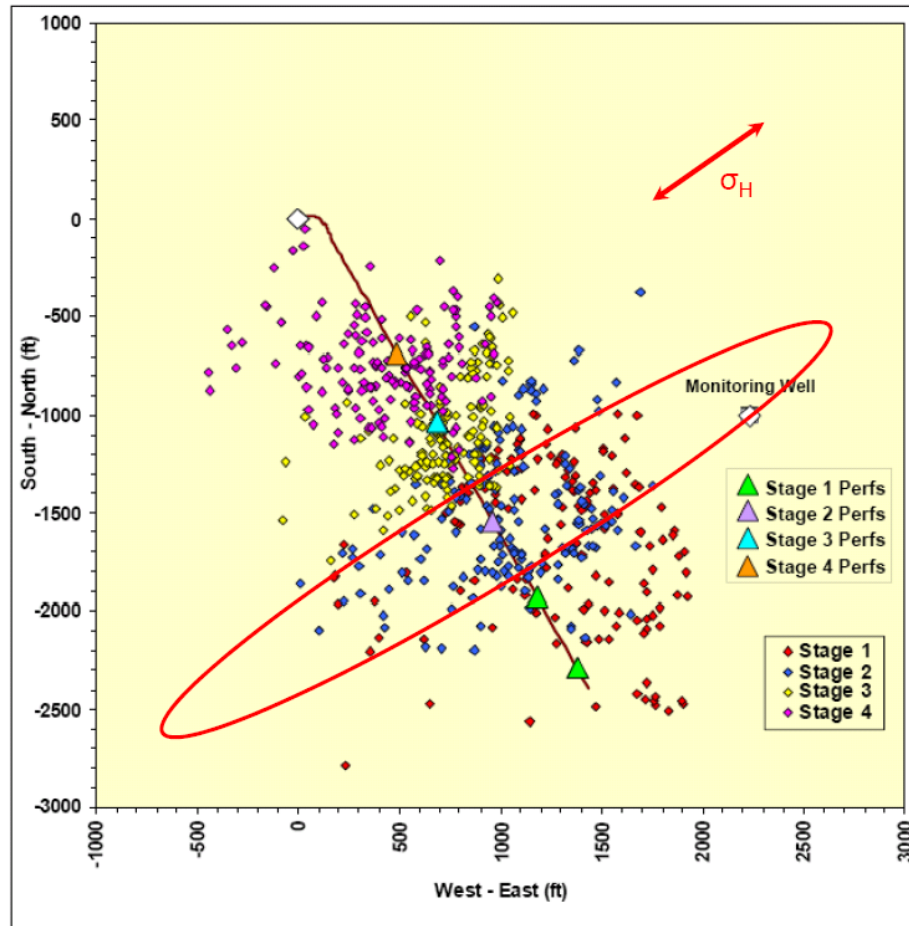
Figure 3.1: Map of the microseismic events generated during a staged hydraulic fracturing treatment, from Waters et al. (2006), shows the orientation of maximum in situ stress, σ_H and the orientation of expansion of microseismic shear events.

Additionally, the apparent toughness of the earth as seen by a hydraulic fracture can be higher than laboratory values because of the presence of natural fractures in the

near tip region. Delaney and Pollard (1981) considered a similar problem for the effect of pre-existing joints (or simply flaws) in the fracture process zone on apparent fracture toughness for en echelon dike propagation. Germanovich et al. (1998) followed the same analogy to model multi-segmented (or finger-like) hydraulic fractures. Olson and Pollard (1989, 1991) studied the interaction of propagating natural fractures and their cumulative effects on reservoir characterization. However, in most of these studies all fractures are open, already pressurized and actively propagating.

The reason for the existence of apparent toughness is the presence of the debonded naturally fractures, which causes near tip stress redistribution. This contribution is rather similar to plastic deformation at the crack tip of a metal. Although it looks counterintuitive, similar phenomena have been observed in single phase polycrystalline materials for which the fracture energy is many times that of a single crystal (Hutchinson, 1990). The configuration with highest resistance is the configuration that minimizes the maximum energy release rates at all the crack tips involved in the interaction. Obviously, the outcome of such a configuration provides insight to the maximum amount of toughness increase that can happen due to the presence of natural fractures.

Here, the goal is explaining these contradictory outcomes. The purpose of this chapter is to demonstrate how natural fractures in naturally fractured reservoirs could be influential on hydraulic fracturing treatment efficiency, and the resulting gas production.

Three possibilities might occur during the hydraulic fracturing of naturally fractured reservoirs (Figure 3.2). First, the natural fractures may have no influence and

the hydraulic fracture will propagate in a direction parallel to the maximum horizontal stress, as expected in the classic sense. This may be a result of high cement strength in the natural fractures (comparable to matrix strength), unfavorable natural fractures orientation, or a fracturing pressure that is not high enough to overcome the normal stress perpendicular to the natural fracture. In the second scenario, once the hydraulic fracture intersects the natural fracture, the hydraulic fracture is arrested and the fluid is completely diverted into the natural fracture system. The natural fractures will open if the energy of the growing hydraulic fracture is large enough to debond (re-open) fracture cements or if the shear stresses are large enough to overcome the friction between fracture surfaces. In the third scenario, both the newly formed hydraulic fracture and the natural fractures will interact and intersect in a complex manner. Debonding can also take place ahead of the primary crack before the fractures intersection (Figure 3.3). The growing fracture exerts large tensile and shear stresses ahead of and near the tip. These stresses can be large enough to debond or shear the sealed natural fractures. So in the first series of events (Figure 3.2), the hydraulic fracture propagates all the way into the natural fracture before the interaction occurs. In the other case, the natural fracture starts to open/shear or propagate before the hydraulic fracture arrives because of near-tip stress concentrations. If this happens, it may even divert the growing fractures into double-deflection in the natural fractures. In this scenario the natural fracture may stop (arrest) the growing hydraulic fracture in the case of high stress anisotropy.

The properties of fracture cements are distinct from those for intact rock. Depending on the cement material (and fracture) properties, the pre-existing fractures

may act as a weak path or a barrier for further crack propagation. This forms a competition between sealed pre-existing cracks and the intact matrix for fracturing (Figure 3.4).
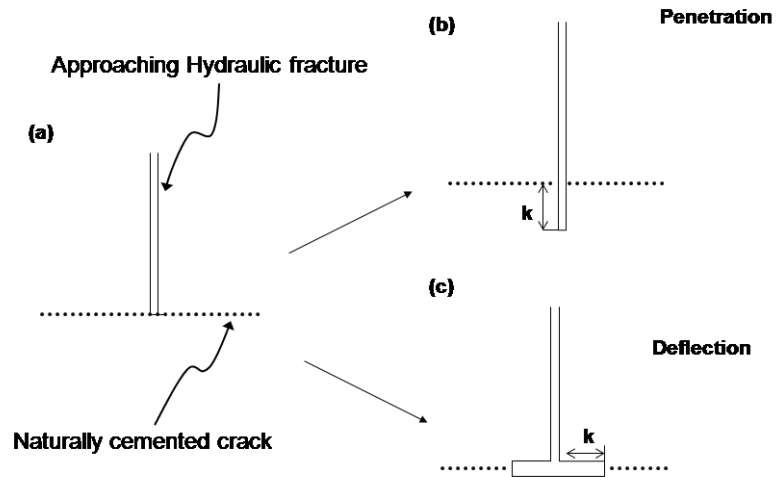
Figure 3.2: Possible scenarios at normal intersection of a hydraulic fracture and a natural fracture.

(a)   (b)
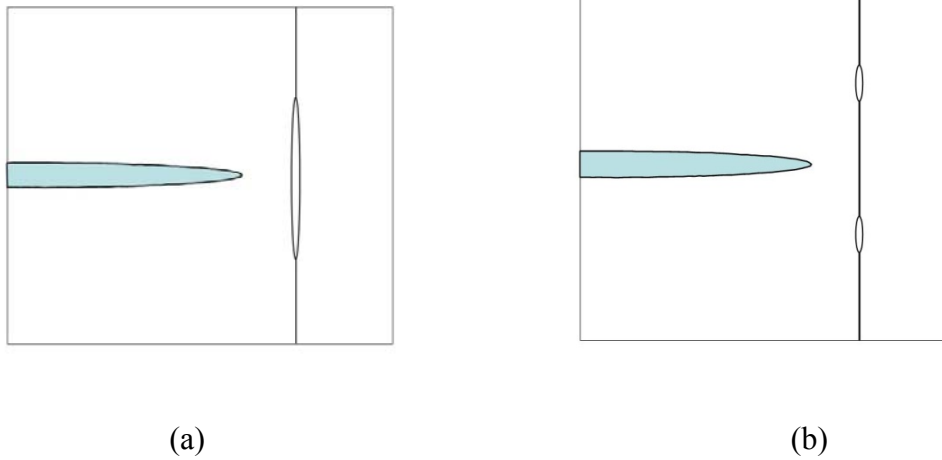
Figure 3.3: Schematic illustration for debonding induced by the approaching crack, (a) induced by tensile failure, and (b) induced by shear failure.
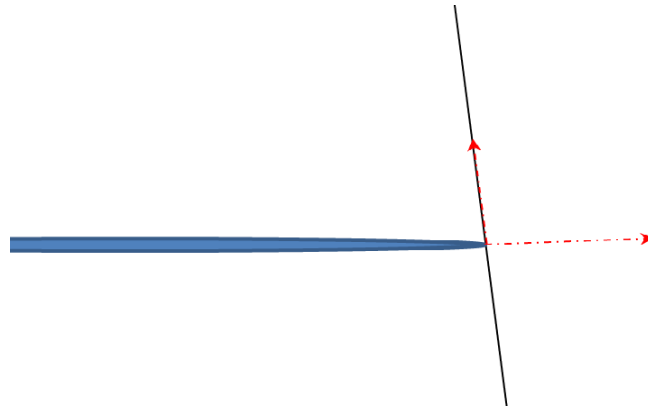
Figure 3.4: Intersection of Hydraulic fracture with closed cemented fracture. Two potential growth paths have been shown in red.

The methodology presented in this chapter does not incorporate the fluid flow part of the problem. The main concentration is on the fracture mechanics aspect of the problem. The fluid flow communication between hydraulic fracture and natural fracture is accomplished by extending the uniform pressure boundary conditions along the

77

hydraulic fracture to all intersected and reopened natural fractures. This is equivalent to assuming a zero-viscosity fluid as done in Olson (2008).

3.2. Analytical results

Attention here is mainly focused to the interaction between the hydraulic fracture and one or two natural fractures. A rational for limiting the investigation to one or two of the closest fractures is the work of Montagut and Kachanov (1988) on large arrays of interacting microcracks. Their calculations suggest that locations of the nearest microcracks largely determine whether shielding or anti-shielding happens and details of the distribution of microcracks outside the tip region is less important.

Fracture interaction was examined by looking at the analytical results for stress around the tip of a pressurized hydraulic fracture. The normal and shear stresses for a uniformly pressurized crack of length 2a are (Pollard and Segall, 1989)

$$\sigma_{xx} = \frac{P\sqrt{\pi a}}{\sqrt{2\pi r}}\cos\frac{\theta}{2}\left(1-\sin\frac{\theta}{2}\sin\frac{3\theta}{2}\right), \tag{3.1}$$

$$\sigma_{yy} = \frac{P\sqrt{\pi a}}{\sqrt{2\pi r}}\cos\frac{\theta}{2}\left(1+\sin\frac{\theta}{2}\sin\frac{3\theta}{2}\right)+P, \tag{3.2}$$

$$\sigma_{xy} = \frac{P\sqrt{\pi a}}{\sqrt{2\pi r}}\sin\frac{\theta}{2}\cos\frac{\theta}{2}\cos\frac{3\theta}{2}, \tag{3.3}$$

where r and θ are local polar coordinates at the crack tip (Figure 3.5), σ_{xx} and σ_{yy} are the normal stresses parallel and normal to the crack, respectively and σ_{xy} is the shear stress. P is the pressure inside the crack.
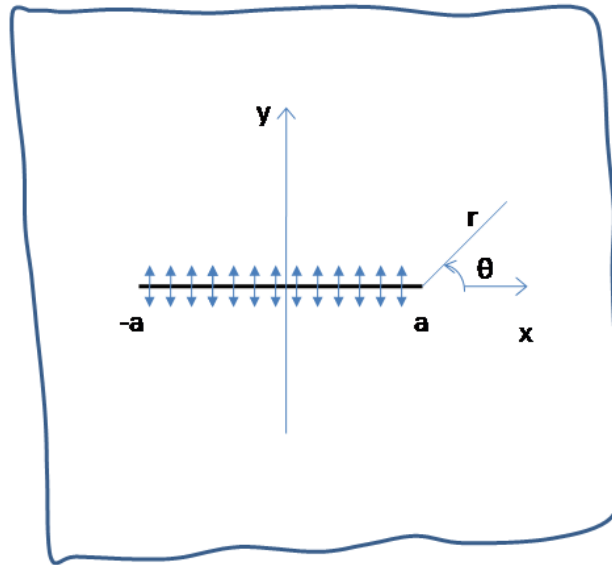
Figure 3.5: The geometry of a pressurized crack in an infinite plate.

The cemented natural fracture is not actually included in the analysis – the stresses along the location of a hypothetical crack are simply calculated. The shear and normal tractions induced on the cemented crack lying parallel to the hydraulic fracture is plotted in the Figure 3.6. Only the part of the natural fracture that is very close and ahead of the hydraulic fracture tip is under tensile stress (from -0.070 toward ahead, where the distance between fractures is 0.25), otherwise the hydraulic fracture exerts additional compression on the natural fracture (behind the hydraulic fracture tip). The shear traction peaks slightly behind the hydraulic fracture tip at -0.04 with a right lateral shear sense (positive), while ahead of the tip the shear sense is left-lateral but much smaller in magnitude. These results indicate that it is most likely to get opening mode fracture

growth initiated ahead and to either side of the tip of an approaching hydraulic fracture. Induced shear is more likely where shear stress magnitude peaks behind the tip, where the induced normal stress is slightly tensile. Both are conditions that would promote slip. The shear-induced slip may not result in additional fracture propagation, but it may generate microseismic events that can be used to map the passage of the hydraulic fracture tip through the rock mass.

For the case where the natural fractures are orthogonal to the hydraulic fracture path (the case for the Barnett Shale), the shear and normal tractions exerted on the sealed cemented crack lying normal to the hydraulic fracture is plotted in the Figure 3.7. The hydraulic fracture extends from west to east while the natural fracture runs from south to north. Only the part of the natural fracture that is within a specific radius from the hydraulic fracture tip is under tensile stress (in this example for the part (a), it is extended from -3.9 to 3.9), however, the length of tensile zone is much larger than the case of parallel fractures discussed in the previous example. This observation suggests more successful results of hydraulic fracturing in reservoirs that natural fractures are orthogonal rather than parallel to the orientation of maximum horizontal stress. The shear traction peaks is slightly offset with respect to the hydraulic fracture tip at x=2.0 with a right lateral shear sense (positive). These results indicate that it is most likely to get opening mode fracture growth initiated ahead of the tip of an approaching hydraulic fracture. Induced shear is more likely where shear stress magnitude peaks behind the tip, where the induced normal stress is slightly tensile. Both conditions would promote slip.
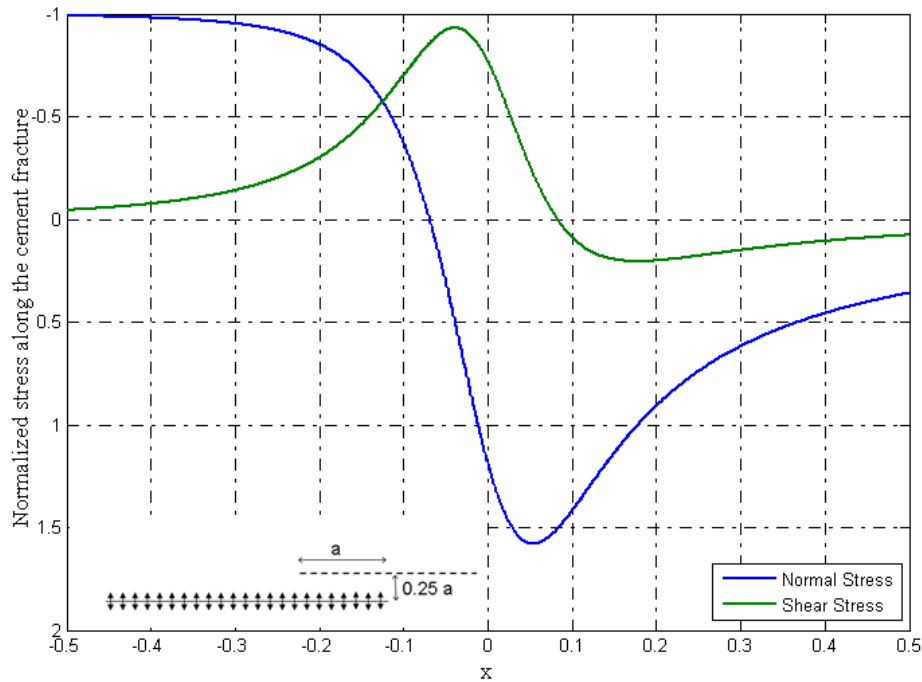
Figure 3.6: The shear and normal tractions (negative, if compression) exerted on the closed cemented fracture is plotted by blue and green lines. The origin for the x-axis is the closest point of the natural to the hydraulic fracture shown in the legend.

The next stages of fracture propagation after debonding are too complicated to be followed by analytical methods. This discussion is left here for later in the numerical results section.

To develop a better insight into this mechanism, the same analytical calculations were repeated for the case in which the hydraulic fracture is inclined rather than perpendicular to the natural fracture (Figure 3.8). The hydraulic fracture extends from west to east while the natural fracture runs from south-west to north-east (They make 45 degree angle with respect to each other). Only the part of the natural fracture that is very close and located in the south side (behind) of the hydraulic fracture tip is under tensile

81

stress (in this example for the plot in part (a), it is extended from -8.1 to -5.1), otherwise the hydraulic fracture exerts additional compression on the rest of the natural fracture (behind and ahead of the hydraulic fracture tip). It is notable that the length of the zone under tension is much shorter than in the previous case.

The shear traction peaks is shifted completely to one side of the hydraulic fracture tip at -3.2 with a right lateral shear sense (positive), while ahead of the tip the shear sense is left-lateral but much smaller in magnitude. As the hydraulic fracture grows farther toward the natural fracture, the shear peak point shifts toward the head of the hydraulic fracture tip. These results indicate that it is most likely to initiate shearing mode fracture growth behind the tip of an approaching hydraulic fracture. Induced shear is more likely where shear stress magnitude peaks behind the tip. The shear-induced slip may not provide porosity, but it breaks the natural fracture's seal and generates microseismic events (similar to the case of Figure 3.6) that can be used to record the passage of the hydraulic fracture tip through the rock mass.
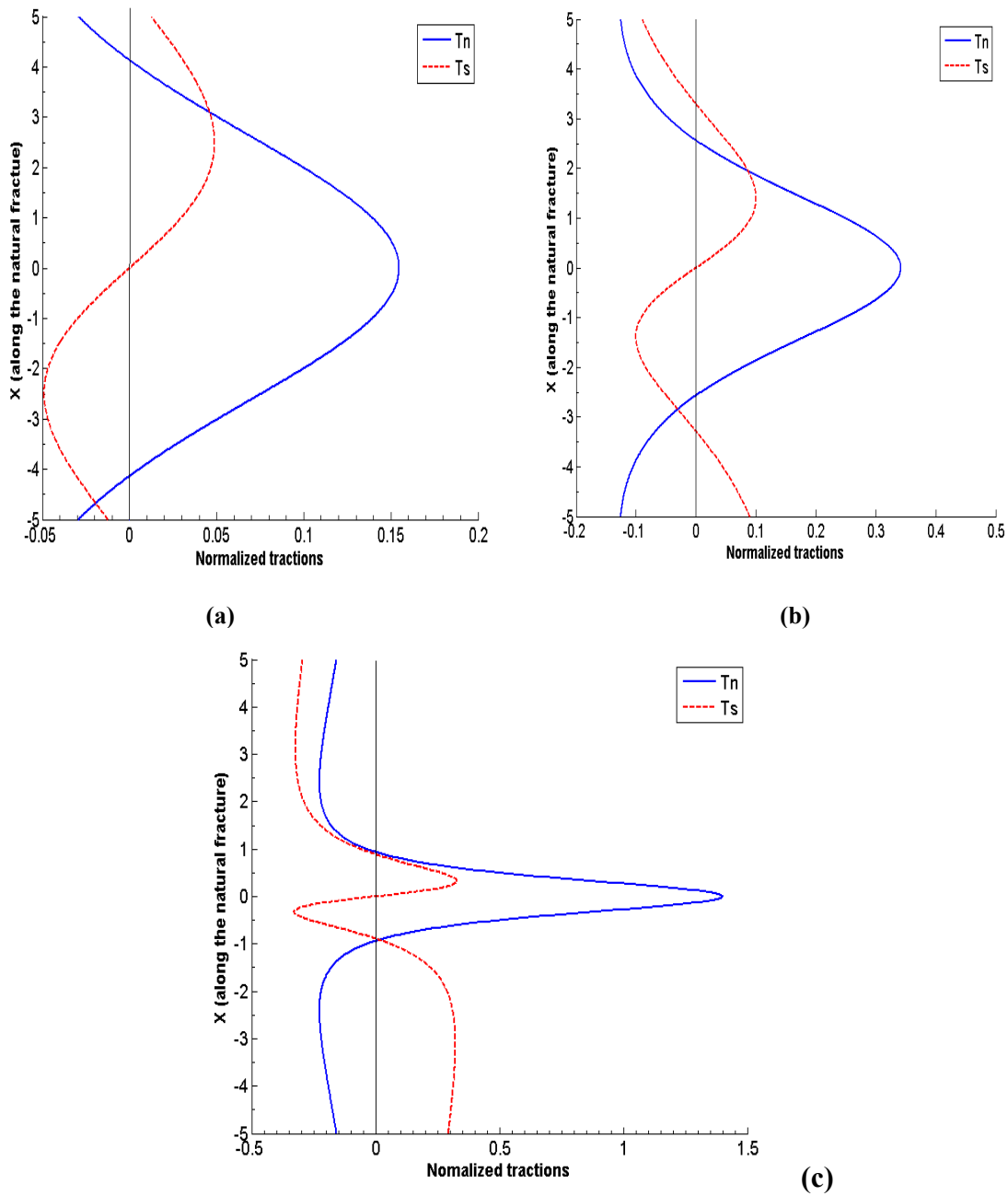
Figure 3.7: Normal and shear tractions ahead of the normal primary crack that are experienced by a sealed crack at distances of 1.0, 0.5 and 0.05 respectively (distances and tractions are normalized with respect to growing fracture length and pressure, respectively). These results are reproduced by XFEM results.
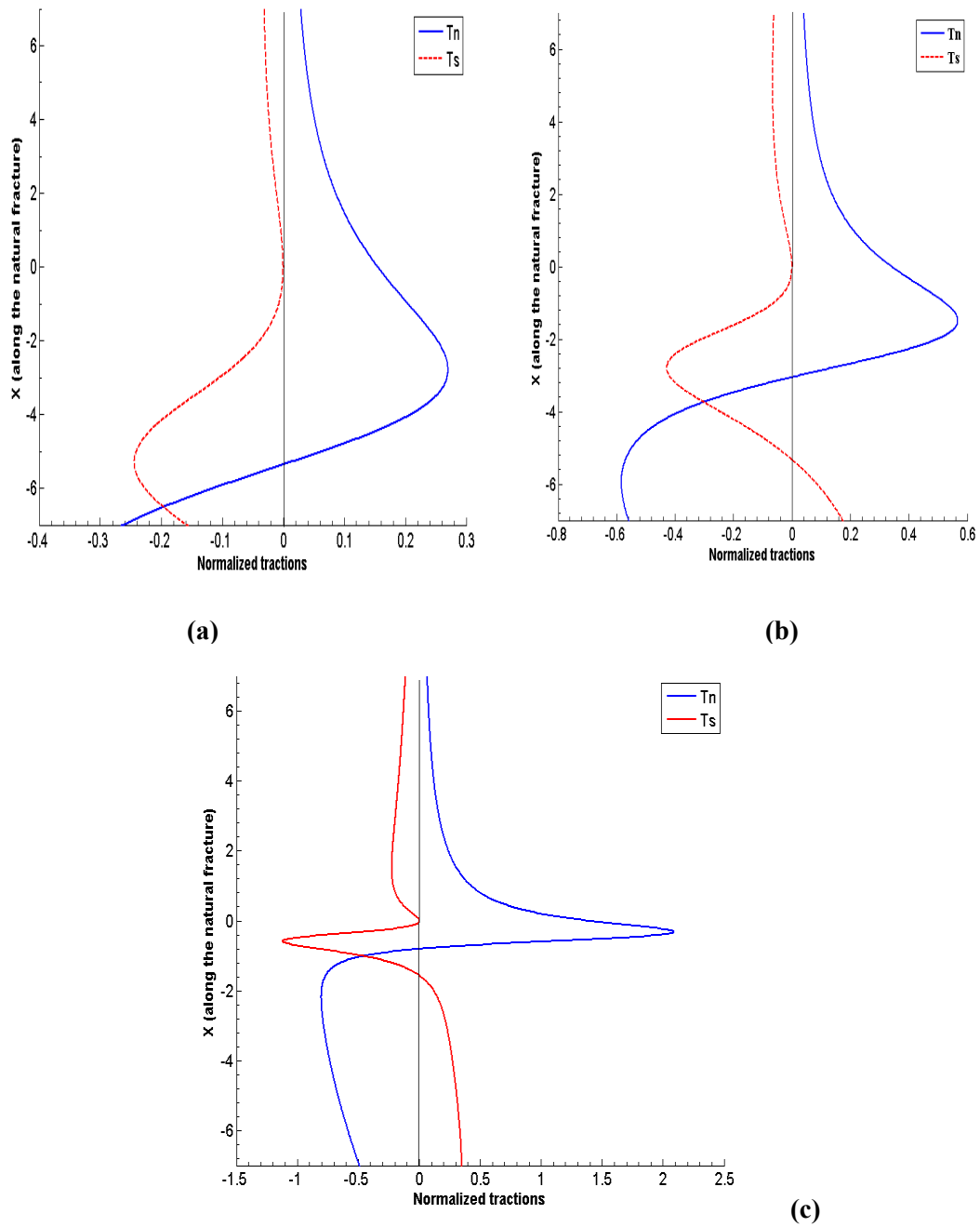
Figure 3.8: Normal and shear tractions ahead of the declined primary crack (45 degrees) that are experienced along the sealed crack at different distances to the middle of the seal crack: 1.0, 0.5 and 0.05 respectively (distances and tractions are normalized with respect to growing fracture length and pressure, respectively). These plots were compared with XFEM results.

84

The minimum potential energy principle implies that double-deflected cracks may not be produced by a simple intersection of the hydraulic fracture and sealed natural fractures, but the occurrence of debonding in the natural fractures located ahead of the primary hydraulic fracture may generate several progressive strands for the propagating fractures. This would explain the formation of the observed multi-stranded fractures. This phenomenon was first suggested for cracks in composite materials by Cook and Gordon (1964), but it took a longer time to be experimentally observed in some biomaterial systems (for instance Majumdar et al., 1998). Leguillon et al. (2000) tried to analyze the asymptotic behaviors of this mechanism.

3.3. Crack propagation criteria

The stress fields from the analytical, static results suggest a way in which fractures might interact and propagate. However, the actual propagation is calculated using criteria from linear elastic fracture mechanics (LEFM). Fracture propagation in LEFM is a function of opening and shearing mode stress intensity factors (K_I and K_{II}, respectively), which are measures of stress concentration at the tip of the crack (Lawn, 2004). The two stress intensity factors are combined in the energy release rate fracture propagation criterion used in this research. The energy release rate, G, is related to the stress intensity factors through Irwin's relation,

$$G = \frac{(K_I^2 + K_{II}^2)}{E^*} \quad , \tag{3.1}$$

where $E^* = E$ for plane stress (E is Young's modulus) and $E^* = E/(1-v^2)$ for plane strain (where v is the Poisson's ratio). If the energy release rate is greater than a critical value, G_c, the fracture will propagate critically. This is the propagation criterion in the absence of chemical weakening effects that can cause "sub-critical" crack growth (Atkinson, 1989). However, in subcritical crack growth, a similar criterion can be prescribed, but with a modified value of G_c. In linear elastic fracture mechanics, the energy release rate is equal to the value of J-integral (Rice, 1968).

The direction of the fracture growth is that which maximizes the energy release rate. If $\bar{G}$ is the energy release rate in a specific orientation, θ_0, Nuismer's (1975)

$$\bar{G} = \frac{\bar{k}_I^2}{E^*} + \frac{\bar{k}_{II}^2}{E^*} \ , \tag{3.2}$$

then

$$\bar{k}_I = \frac{1}{2}\cos(\frac{\theta_0}{2})\left[K_I(1+\cos\theta_0) - 3K_{II}\sin\theta_0\right] \tag{3.3}$$

and

$$\bar{k}_{II} = \frac{1}{2}\cos(\frac{\theta_0}{2})\left[K_I\sin\theta_0 + K_{II}(3\cos\theta_0 - 1)\right] \ . \tag{3.4}$$

Nuismer (1975) derived these equations from Westergaard's solution using perturbation techniques. The values for $\bar{k}_I$ and $\bar{k}_{II}$ at different orientations for pure mode I is plotted in Figure 3.9.
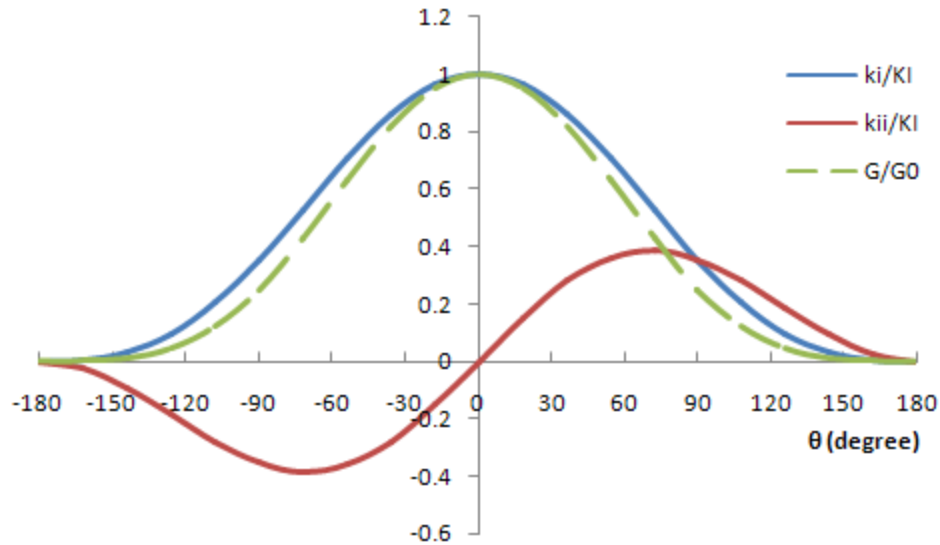
Figure 3.9: Values of $\bar{k}_I$ and $\bar{k}_{II}$ for a pure mode I case is plotted in this figure. The values are normalized with respect to the maximum stress intensity factor, K_I. The energy release rates in different directions are plotted (normalized with respect to its maximum value.).

In the case that sufficient energy is available for fracture propagation, and where a crack has more than one path to follow (Figure 3.4), the path most likely for it to utilize would be the path that has the maximum energy release rate, or the greater relative energy release rate (Freund and Suresh, 2003). The two paths can be compared by looking at the ratios G/G_c^{rock} and G/G_c^{frac} (Figure 3.10), where G_c^{rock} is the rock fracture energy (the energy release rate corresponding to fracture toughness) and G_c^{frac} is the energy required to open the unit length of the cemented fractures. Fracture re-opening may happen through the cement or through the cement-matrix interface. Thus, G_c^{frac} is associated with the smaller value between the cohesion of the cement and intact rock or the adhesion of cement grains to each other. If G/G_c^{frac} is greatest, the pre-existing

87

fracture will re-open. If G/G_c^{rock} is greatest, propagation will create new fracture surface

following a path of $K_{II} = 0$.

(a)   (b)
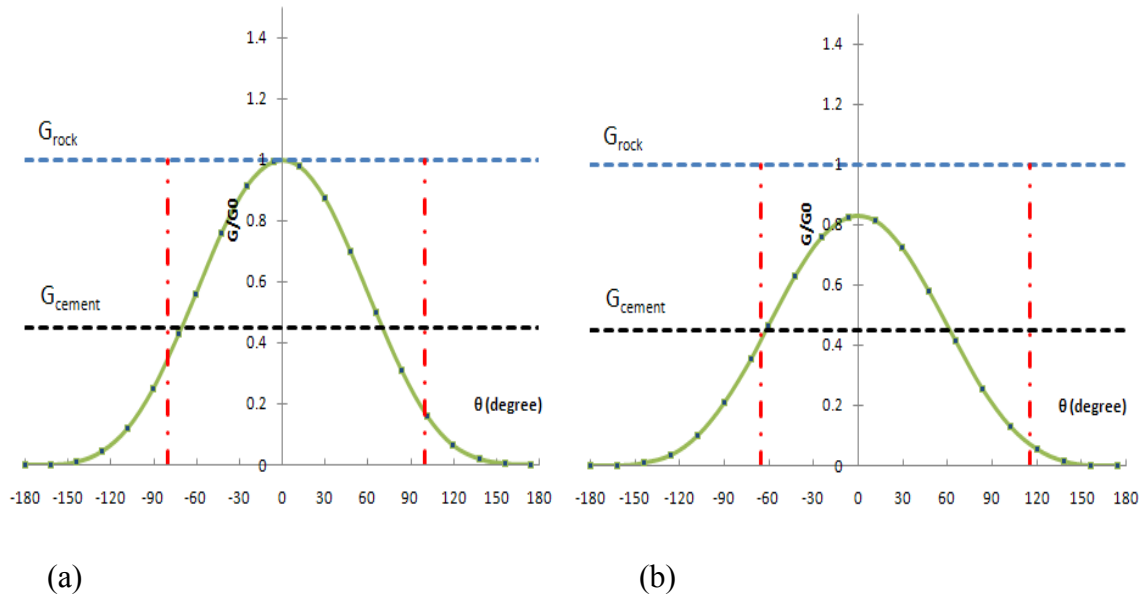
Figure 3.10: Part (a) shows an example where there is not sufficient energy release rate for fracture growth in the direction of the natural fracture shown in red line (-80 and 100 degrees), but there is sufficient energy to fracture the rock. Part (b) shows the case where the fracture will grow in one the fracture wings (oriented at -65 degree).

The crack deflection into one side of the sealed crack corresponds to higher

energy release rate compared to the deflection into both sides. For instance, it requires

about 30% extra energy to induce double-sided fracture for the normal incidence angle

case (He and Hutchinson, 1989). Therefore, the crack will generally deflect to one side

after intersecting the sealed fracture. Although the double branch could occur if the

toughness of the fracture cements depends strongly on the stress intensity factor phase

angle (He and Hutchinson, 1989). The stress intensity factor phase angle is the tangent of the ratio of mode I and mode II stress intensity factors ($\phi = \tan(K_I / K_{II})$).

Cemented fractures are presumed to have no effect on the stress distribution around the primary crack tip. This would be explicitly true if the two fracture surfaces were perfectly bonded together. Hence, the quality of this assumption depends on the degree of cementation and the relative strength of the cement material and the matrix to which it is bonded.

The growing hydraulic fracture exerts shear and tensile stresses on cemented cracks even before intersecting them. Depending on cemented fracture toughness, the shear and/or tensile components of stress may debond the cemented fractures before the incident crack reaches the cemented fracture as shown in Figure 3.3. This mechanism does not necessarily cause any opening, but debonded fractures can be reopened by the intersecting crack much easier than the bonded fractures.

3.4. Crack Initiation and Crack Kinking

When hydraulic fractures intersect oblique natural fractures, a kink is formed in the fracture path (Figure 3.11b). These kinks can be the locations of stress concentration although the order of stress singularity is not as high as for a crack tip. Additionally, cemented fractures are weak paths for fracture propagation. Suppose that the growing crack (Figure 3.11a) is deflected into a weak path and it advances through the cemented fracture for a while (Figure 3.11b). Due to the increase in fracture length, pressure-drop

along the induced fracture increases. Therefore, the treatment pressure has to be increased to overcome this resistance and to let the hydraulic fracture continue growing. This increase may provide sufficient pressure for the initiation of a new branch of crack from the kink point to the other-side of the sealed fracture. An example of a possible snap-back path is sketched in Figure 3.11c. However, this is a very special case that may happen in certain G_c^{frac}/G_c^{rock} ratios, loading conditions and incidence angle.

The order of stress singularity at the corner (kink) points depends on the angle between fractures that are making the wedged corner (angle α in Figure 3.11). The stress field near the kink point obeys the asymptotic elasticity solution (Szabo and Babuska 1991), which is the generalization of the solution for the stress around the crack tip

$$
\begin{aligned}
\sigma_{xx}^{(1)} &= \lambda r^{\lambda-1}[(2-Q^{(1)}(\lambda+1))\cos(\lambda-1)\theta-(\lambda-1)\cos(\lambda-3)\theta] \\
\sigma_{yy}^{(1)} &= \lambda r^{\lambda-1}[(2+Q^{(1)}(\lambda+1))\cos(\lambda-1)\theta+(\lambda-1)\cos(\lambda-3)\theta] \\
\tau_{xy}^{(1)} &= \lambda r^{\lambda-1}[(\lambda-1)\sin(\lambda-3)\theta+Q^{(1)}(\lambda+1)\sin(\lambda-1)\theta]
\end{aligned}
\tag{3.5}
$$

for the mode I and

$$
\begin{aligned}
\sigma_{xx}^{(2)} &= \lambda r^{\lambda-1}[(2-Q^{(2)}(\lambda+1))\sin(\lambda-1)\theta-(\lambda-1)\sin(\lambda-3)\theta] \\
\sigma_{yy}^{(2)} &= \lambda r^{\lambda-1}[(2+Q^{(2)}(\lambda+1))\sin(\lambda-1)\theta+(\lambda-1)\sin(\lambda-3)\theta] \\
\tau_{xy}^{(2)} &= -\lambda r^{\lambda-1}[(\lambda-1)\cos(\lambda-3)\theta+Q^{(2)}(\lambda+1)\cos(\lambda-1)\theta]
\end{aligned}
\tag{3.6}
$$

for the mode II. r and θ are local polar coordinates shown in Figure 3.12. λ is equal to $\dfrac{\pi}{2\alpha}$, where α is the kink (larger) angle (shown in Figure 3.12). The $Q^{(i)}$ s are defined as

$$
Q^{(1)} = -\frac{\cos(\lambda-1)\dfrac{\alpha}{2}}{\cos(\lambda+1)\dfrac{\alpha}{2}}
\tag{3.7}
$$

$$Q^{(2)} = -\frac{\sin(\lambda-1)\dfrac{\alpha}{2}}{\sin(\lambda+1)\dfrac{\alpha}{2}} \ . \tag{3.8}$$

The singularities at the corners are weaker than the crack tip singularity that makes corners play a role as secondary flaws or as a secondary choice for fracture propagation. In the case of large pressure drops along the fractures or presence of natural barriers against the growing tips, weak paths could be activated at these corners (Figure 3.11). If a corner is activated, the resultant shear slippage at the corner point generates a microseismic event. This scenario may be the cause of seismic activities from scattered locations around the hydraulic fracturing zone.
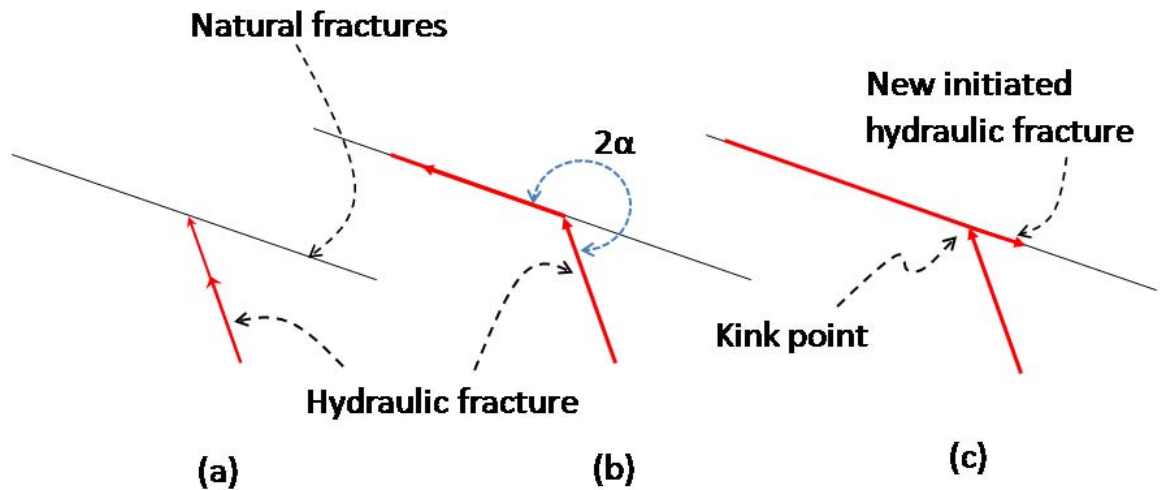
Figure 3.11: This figure shows the steps that leads possible paths for crack initiation at the corner. Part b shows what is called a kink (in the red path). However, it is not guaranteed that fracture propagates in the other wing as there is a competition between the host rock and cemented fracture.
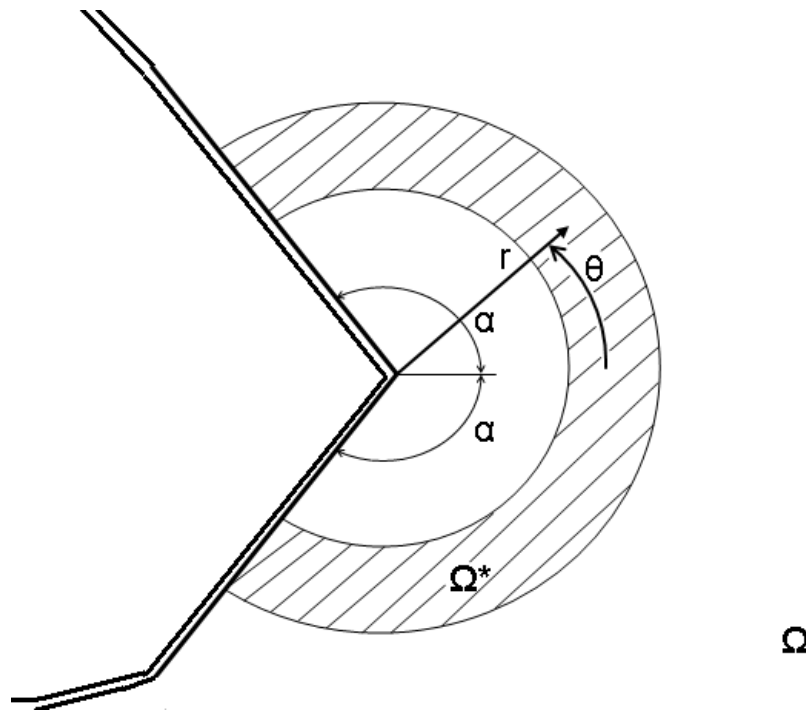
Figure 3.12: Local coordinate system at the crack kink.

3.6. Algorithm for Crack Propagation

The flowchart for the crack growth algorithm is displayed in Figure 3.13. The first step is to solve the governing elasticity equations for the fractured domain. These results are then used to compute the stress intensity factors, K_I and K_{II}, at the crack tips. The flowchart uses a flag parameter called "Debonding Flag". When this parameter is equal to 2, the algorithm checks for possible debonding in the cemented fractures. If the Debonding Flag is 1, it means that a debonded zone is already developed. The crack debonding process could be unstable. The debonded length may jump from an initial value to a certain final length. Therefore, the algorithm calculates the equilibrium fracture

92

length. The third step is to compute the propagation criteria to see which tips are propagating. The tips with energy release rates higher than fracture toughness of the surrounding material will propagate. In the next step, the relevant growth rate of the propagating tips and associated orientation will be determined. Then if any fracture tip propagates, intersection and coalescence with other fractures will be checked. When the distance between a hydraulic fracture tip with an open (or debonded) fracture is less than the minimum allowable length increment for fracture growth, fracture coalescence takes place. At the end of the cycle, all these steps may be repeated again to develop the fracture pattern further.

Further details are involved in the third step. If the current crack tip is within the intact matrix, it is then needed to determine the maximum energy release rate of the crack tip and compare that with its critical value G_c. If the maximum energy release rate (G) is greater than G_c, the crack will propagate in the direction of the maximum hoop stress. The growing crack-tip will move for the determined length increment or up to a sealed crack. If the crack has progressed through the sealed crack, then it is necessary to determine energy release rate (G) in the direction of maximum hoop stress as well as both directions along the sealed crack. The crack-tip will advance in the direction(s) that energy release rate (G) is greater than G_c^i (where i = rock, fracture) if any satisfy this condition. Based on that the crack tip will move forward for a determined length increment along the seal or along the direction of the maximum hoop stress (whatever applies).
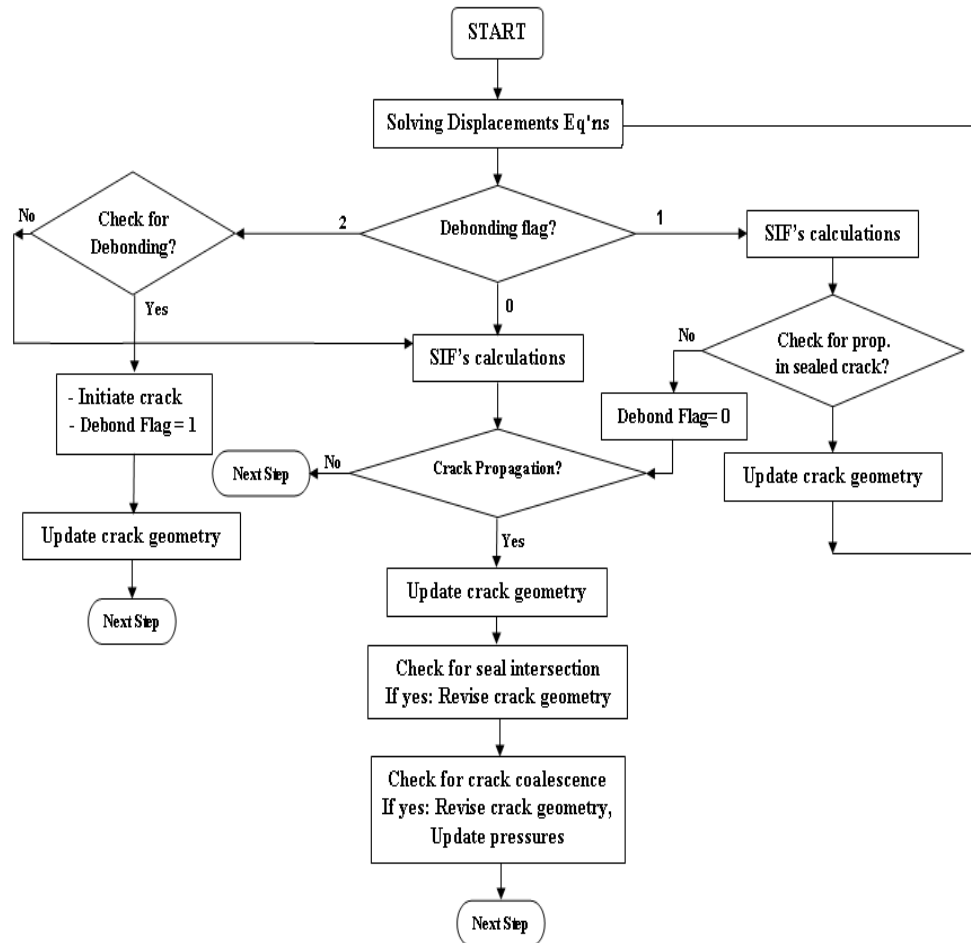
Figure 3.13: Flowchart of the algorithm for crack propagation/debonding.

3.7. Numerical Results

The treatment pressure, rock elastic properties, rock toughness, in-situ stresses, the geometry of natural (pre-existing) fractures and cohesiveness of the cements in the sealed fracture are the data necessary for the simulation. The maximum and minimum

horizontal stresses can be found from the inversion of borehole sonic data (Sinha et al. 2007) or from micro-fracturing or shut-in pressure from pressure-time curves. There are also techniques available in the literature to specify the subsurface fracture pattern characteristics based on the tectonic regime, rock properties and core data (Gale et al. 2004 or Olson et al. 2006). Assuming that all the required data is given, some explanatory examples are solved in this section.

Two distinct possibilities were considered for the interactions between the hydraulic fracture and natural fractures. In the first case, it is assumed that cracks are fully-sealed by cements and will not debond before intersection with the approaching crack. The threshold of the cement fracture toughness is verified. Below this threshold, the approaching cracks will be diverted by the natural fractures, while above that natural fractures will not affect fracture growth direction. For the case of normal intersection (Figure 3.14a), it is found that threshold for G_{frac}/G_{rock} is 0.25 for fracture to be diverted along the path of the existing crack. This value matches the analytical solution proposed by He and Hutchinson (1993) for interface cracks. The calculated threshold is independent of the rock elastic properties. This value is independent of the loading condition and matrix elastic properties. The results were examined for different size of elements and different size of the models. The threshold is strongly dependent on the angle of the intersection, because when natural fractures tilted about 6 degrees with respect to the normal of the primary hydraulic fracture the threshold for G_{frac}/G_{rock} increases to 0.32; and when the tilting angle becomes 30 degrees (Figure 3.14b), the

threshold value for G_{frac}/G_{rock} exceeds one half. By considering the fact that cements are usually weaker than matrix, it implies that natural fracture most probably will divert fractures from the in-situ maximum horizontal stress direction when they are not aligned parallel to the in-situ minimum horizontal stress (Figures 3.14 and 3.15). The threshold value for G_{frac}/G_{rock} for different intersection angles is plotted in Figure 3.14c. It shows that at low intersection angles, there is a small chance that the advancing hydraulic fracture will cross over an existing natural fracture. This could be the case when the orientation of the principle tectonic stresses during the formation of natural fractures is not the same as today's orientation (e.g. Laubach et al. 2004). In this case, if the treatment pressure is not large enough to overcome the exerted stresses (which has a value between S_h and S_H), then the crack tip might be arrested. Subsequently, fractures may resume propagation from any other possible weak position along the already developed fracture, which is similar to the scenario depicted in Figure 3.11. This could be one of the possible cases that lead to the formation of multi-branched fractures.

Based on the algorithm shown in Figure 3.13, several examples will now be solved to show the potency of the technique.
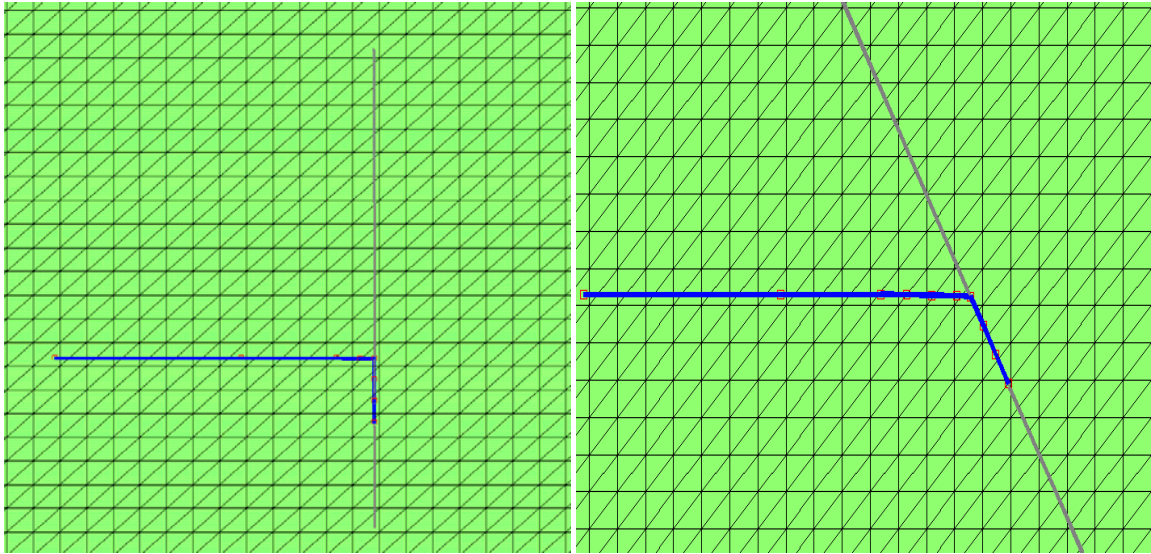
(a)

(b)
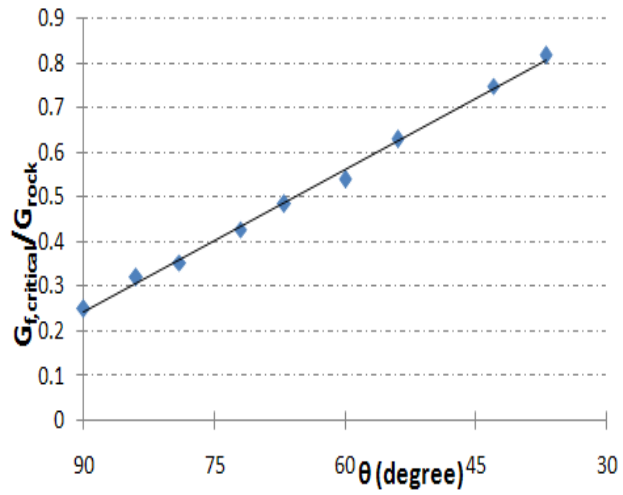
(c)

Figure 3.14: Hydraulic fracture diverted at (a) normal and (b) oblique 60 degrees natural fracture. In part (c), critical values for fracture energy of cements for hydraulic fracture deflection are shown for different orientation of natural fractures.

97
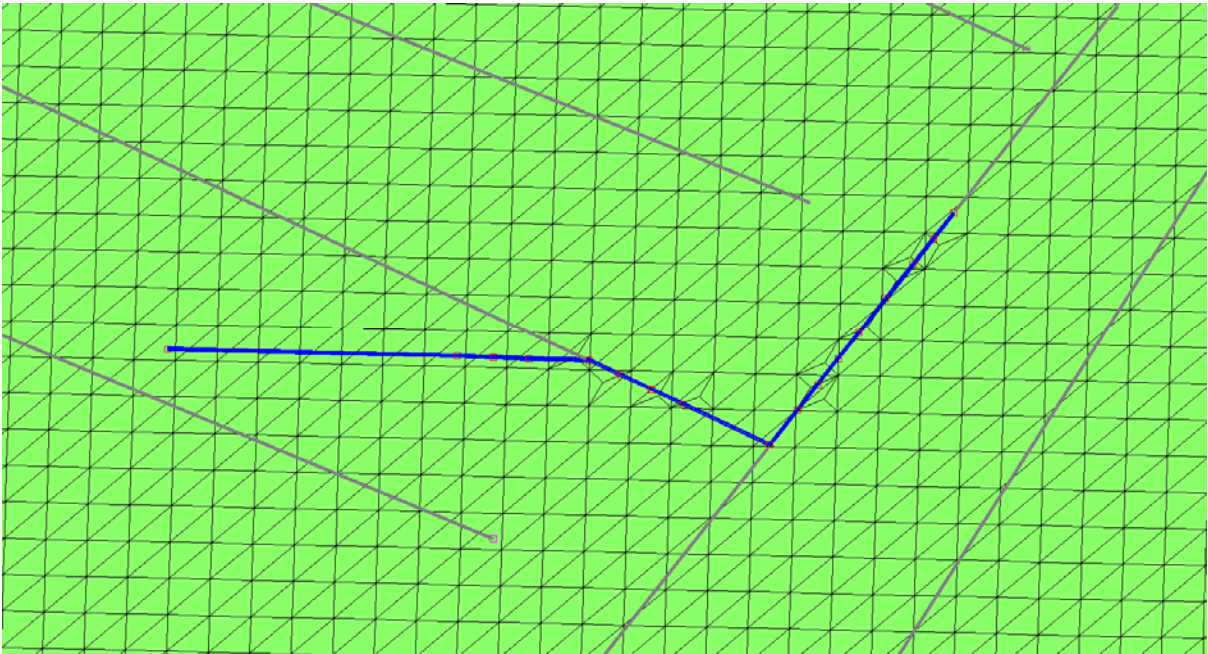
Figure 3.15: Complex geometry of the fracture growth. Natural fractures are depicted with thinner lines.

Subsequently, the induced debonded area may also change the stress intensity factor at the tip of the hydraulic fracture, these changes will be discussed later (figures 3.21-3.23). The opening and sliding displacements along the debonded crack is shown in Figure 3.18. It is remarkable that the debonding length and the stress intensity factors at the tips of the primary fracture or new initiated fracture are independent of the rock stiffness, because the stress field of the growing fracture is independent of rock elastic properties.
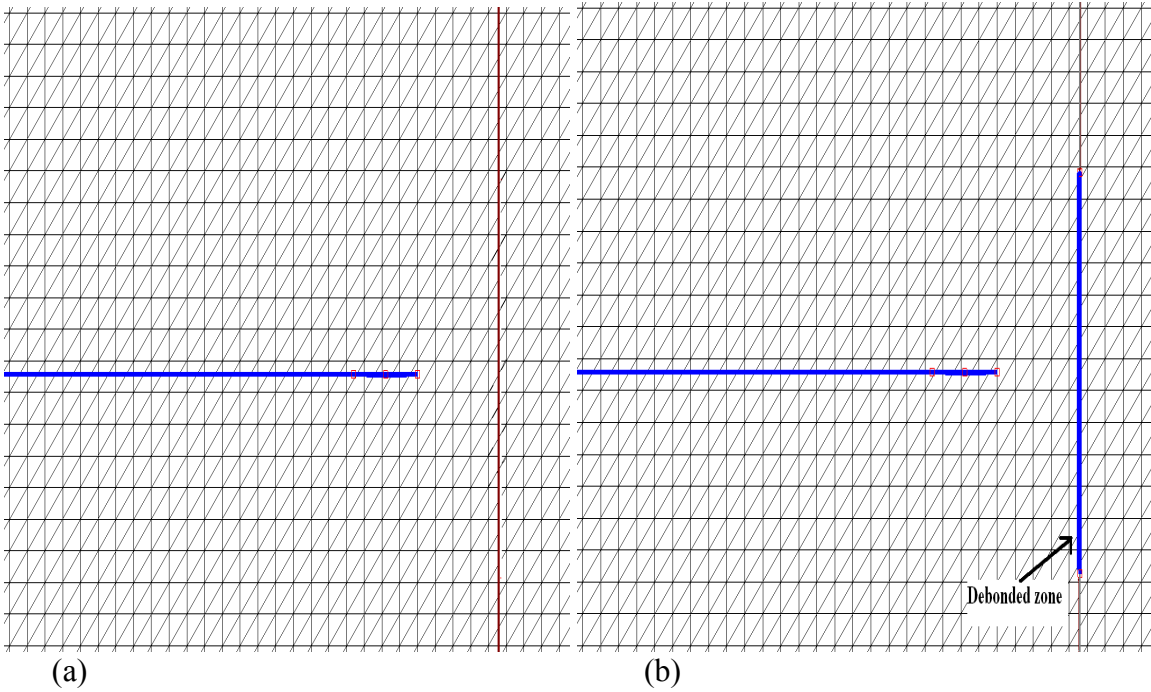
3.16: Symmetric debonding of the sealed crack by a perpendicular primary hydraulic fracture, Parts (a) and (b) show the configuration before and after debonding, respectively.
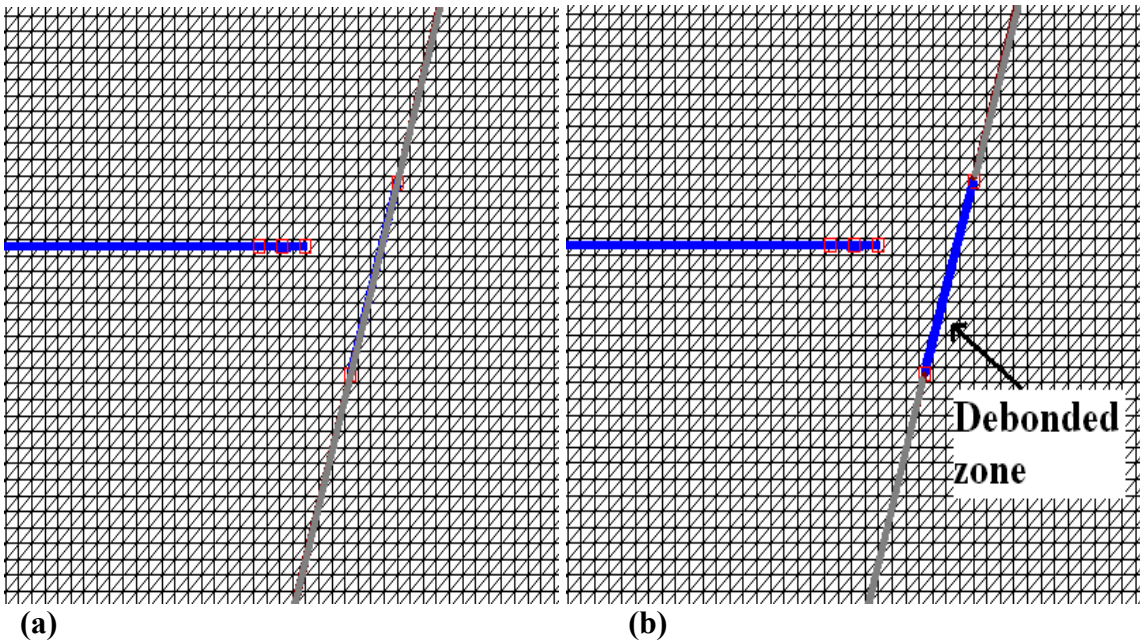
Figure 3.17: Asymmetric debonding of the sealed crack by a non-perpendicular fracture. Part (a) shows the position of the hydraulic fracture before debonding and part (b) shows the configuration after debonding.
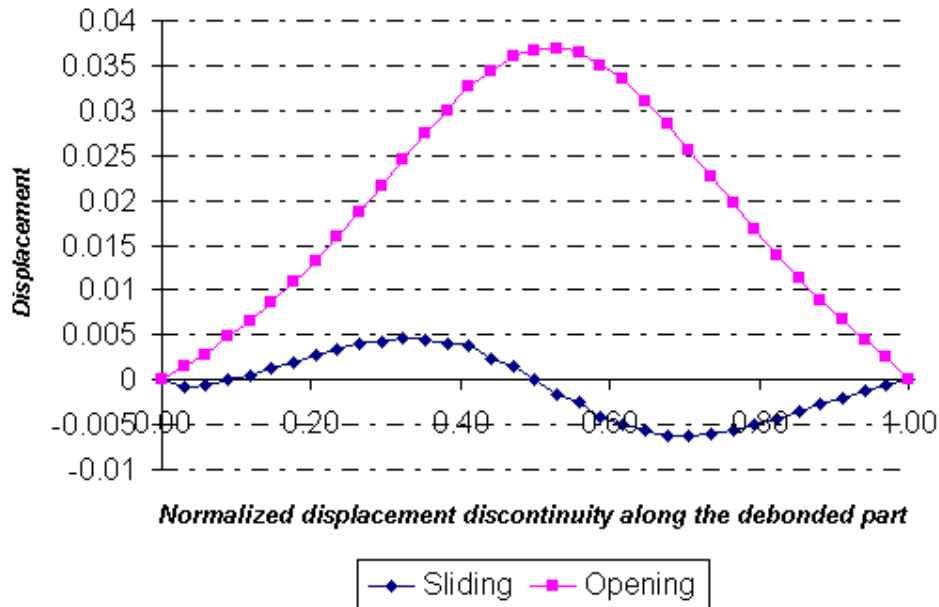
Figure 3.18: The opening and sliding displacements along the debonded zone of Figure 3.16. The opening displacement of the debonded part is not a quadratic function of the position along the crack but the forth order polynomial. It is notable that there is no pressure inside the debonded zone.

For the case of non-normal intersection, the induced debonding is asymmetric with respect to the approaching crack and may possibly become partly closed under the effect of the approaching fracture. In non-normal cases, shear failure plays a significant rule in activating the fractures (Figure 3.19) and forming asymmetric debonding with respect to the approaching crack. This observation can be justified by comparing figure 3.8 and 3.9, where non-normality amplifies the shear traction exerted on the natural fracture. Shear induced debonded zones (such as Figure 3.19) are not necessarily intersected by the advancing hydraulic fracture.

100

The fracture deflected by non-normal intersection have an asymmetric opening which directs the fluid toward the direction going farther from the primary fracture so double-deflected fracture will tend to propagate on just one-side (Figure 3.20).

The next stages of fracture propagation after debonding is complicated as the fracture propagation will be dominated by many factors such as anisotropy of tectonic stresses and the size and orientation of the debonded length with respect to the tip of hydraulic fracture.

Shum and Hutchinson (1990) and Hutchison (1987) studied the crack tip shielding and anti-shielding by parallel en echelon offsetting cracks. However their analyses were limited to uniform far-field loading which is not the case for hydraulic fracture but it may represent high permeability reservoirs case, where both fractures could be pressurized.
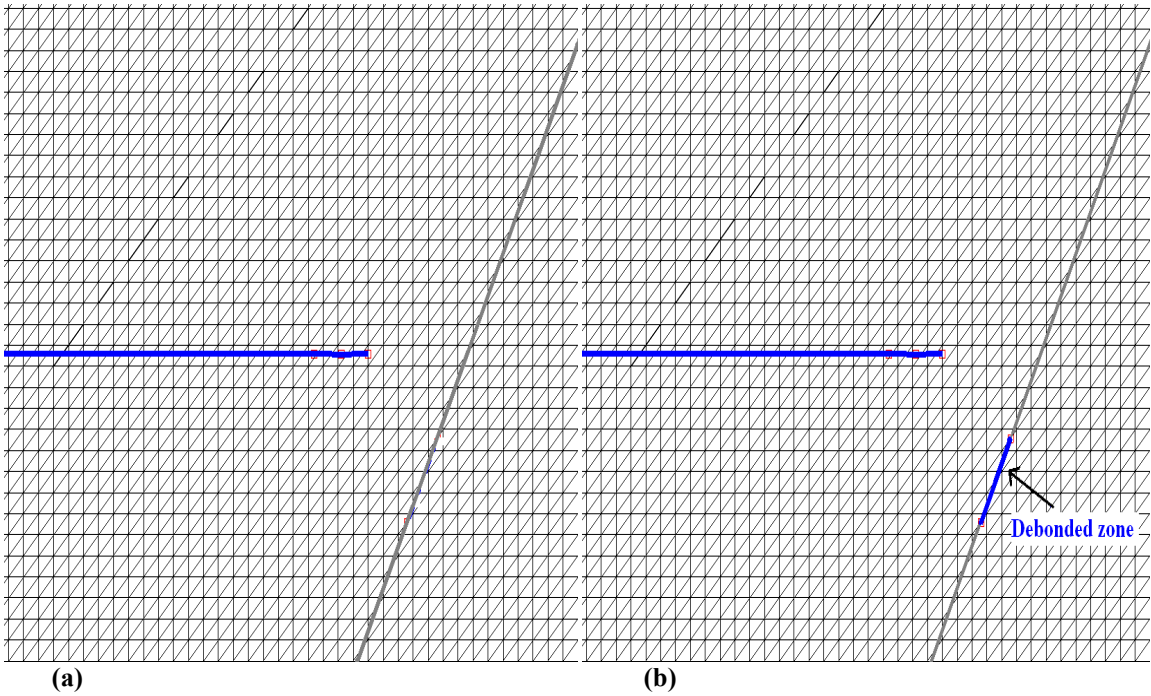
Figure 3.19: Debonding zone (right side) is caused by shear failure. Cemented natural fracture is demonstrated in gray.
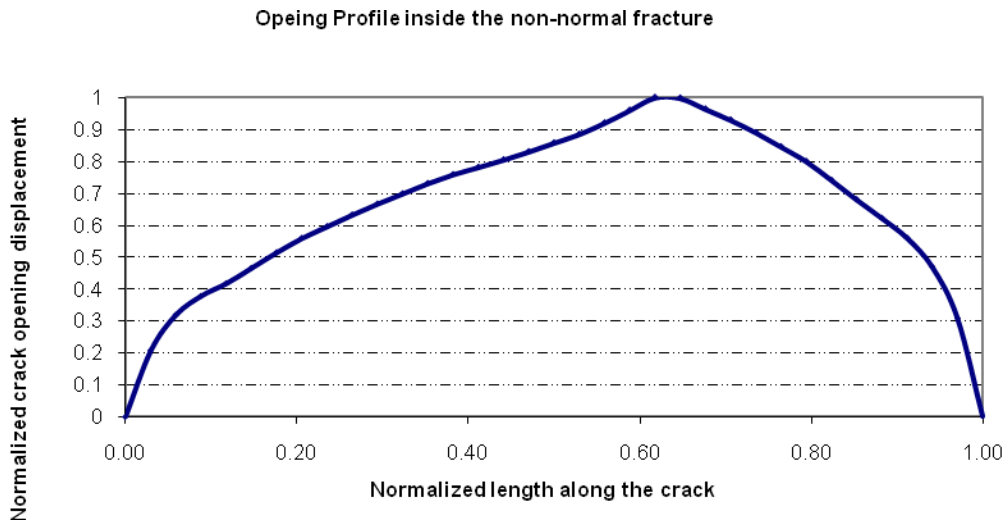
Figure 3.20: Asymmetric crack opening displacements along the non-normal double-deflected fracture.

The crack debonding phenomena may also occur in parallel (and subparallel) fractures as well. In such situations, the effect of the re-opened fractures is complicated. In next stages of hydraulic fracture growth, the debonded zone of natural fracture might be closed or partly closed under the compression of the growing pressurized hydraulic fracture. Depending on the position of the natural fracture with respect to the hydraulic fracture, stress intensity factor at the tip of hydraulic fracture might be greater or less than the case of a single fracture (Figure 3.21). So in some cases, the pre-existing fractures may virtually increase rock toughness and consequently requires higher pressure for further fracturing of the reservoir. All previous works in this field have considered the effect of farfield mode I or mode II boundary conditions. However, for the hydraulic fracturing problem, different boundary conditions have to be considered, which leads to different stress field distributions. In Figures 3.22 and 3.23, changes of stress intensity factor at the tip of hydraulic fracture due to the presence of surrounding open natural fracture is compared for the case of farfield boundary condition and hydraulic fracturing problem boundary conditions.

In Figure 3.22, the effect of non-aligned reactivated fractures is shown. The amplification of stress intensity factor at the tip of the hydraulic fracture is also plotted. It is assumed that a/b = 0.20. For large values of angle α (demonstrated in Figure 3.22), the natural fracture might be closed, but sliding along the sides of natural fractures become a mechanism for deformation relaxation and amplification of the stress intensity factor at the tip of the hydraulic fracture. Therefore, by maintaining constant fluid pressure in the primary crack, it will be accelerated toward the debonded crack. It is notable that no fluid

pressure is assumed inside the debonded crack before the intersection with the primary hydraulic fracture.
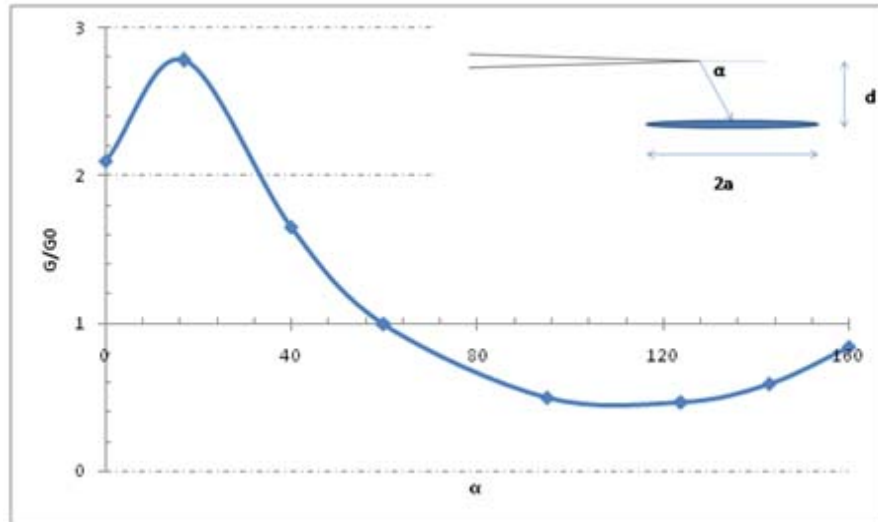
Figure 3.21: Normalized energy release rate at the tip of a growing hydraulic fracture which is under the influence a parallel fracture.

Weertman (1984), Shum and Hutchinson (1990) and Hutchison (1987) studied the crack tip shielding and anti-shielding by parallel en echelon offsetting cracks. However their analyses were limited to uniform far-field loading which is not the case for hydraulic fracturing problem. The difference between two regimes of loading is evident in Figure 3.22b. The amplification of energy release rate in case that only hydraulic fracture is pressurized, is larger than the case were both fractures are pressurized.

Figure 3.23 and its associated plot show that hydraulic fracture would be attracted toward the debonded zone especially at low angles, α. However, this tendency depends on the orientation of the debonded zone with respect to the hydraulic fracture.

104

Based on the previous examples, one may conclude that if debonding or cement failure happens due to the tensile failure (Figure 3.16) there is more chance for fracture coalescence, rather than the case where cements inside the fracture failed under the effect of shear stresses (Figure 3.19). Because tensile-induced debonded zones (Figure 3.23) attract the advancing hydraulic fracture, but Shear-induced debonded zones are not necessarily intersected by the advancing hydraulic fracture. Fracture coalescence is very important because isolated debonded zones will not contribute to flow inside the hydraulic fracture, hence they will not enhance well performance. However, isolated reopened fractures may generate some microseismic activities and contribute to the scattered cloud of epicenters.
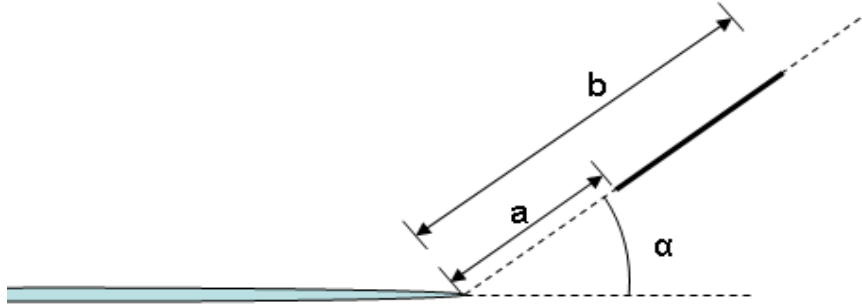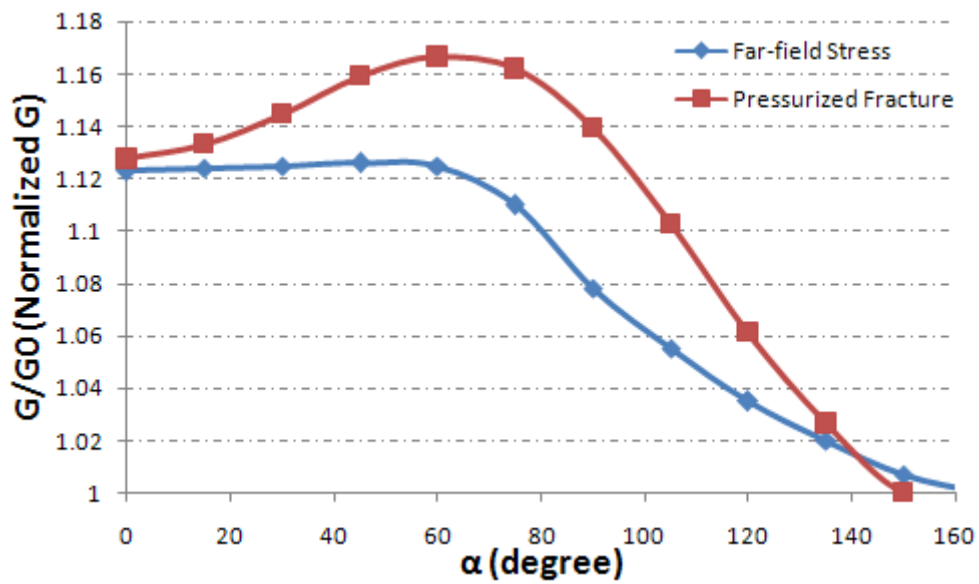
Figure 3.22: (a) The position of natural fracture (with length b-a) is shown with respect to approaching hydraulic fracture (a/b =0.20). (b) Normalized energy release rate for the hydraulic fracture tip for two situations are plotted, first, only the hydraulic fracture is pressurized. In the second case, both fractures have the same pressure.
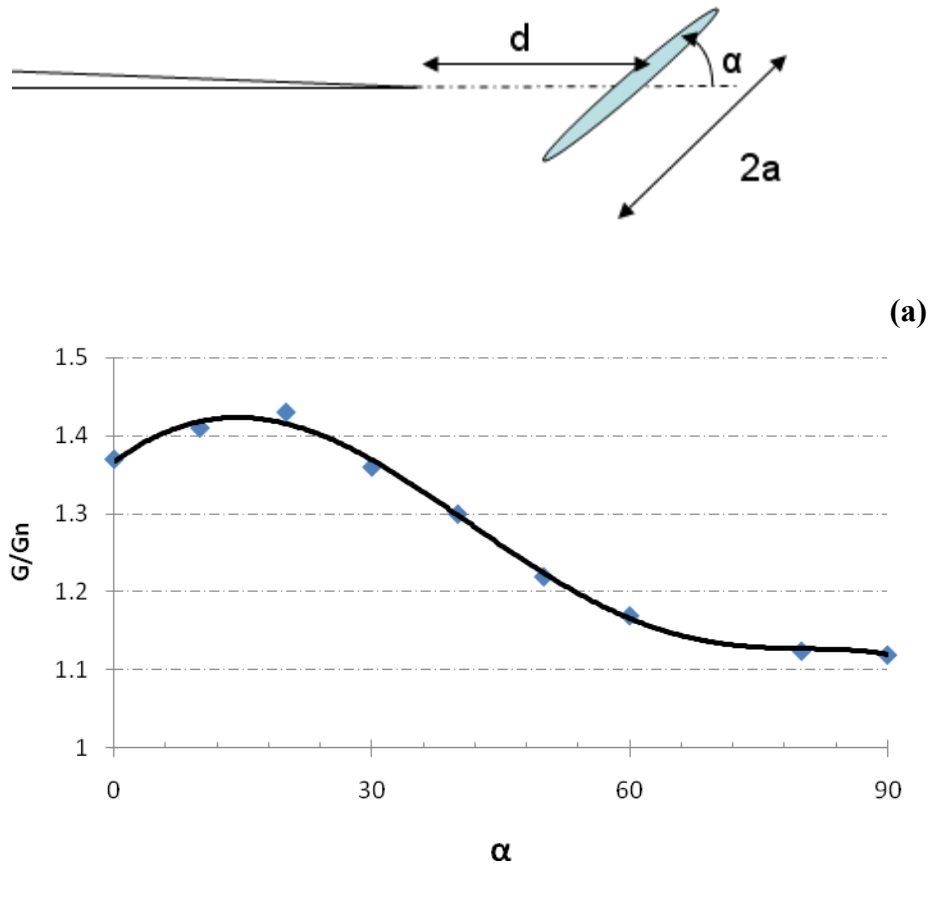
Figure 3.23: (a) The schematic picture of hydraulic fracture (left) in interaction with a debonded natural crack (right). (b) Normalize energy release rate at the tip of the hydraulic fracture is plotted for different natural fracture orientation. For calculations, it is assumed that $d/a=1.50$.

In some cases because of the specific geological structures like the existence of a major fault or sagging structures near the fracturing zone, there may not be an isotropic in-situ stresses. Under such conditions, crack deflection will not be affected by the anisotropic tectonic stresses. However, stress anisotropy may affect the growth rate of the deflected fracture in the new direction or even shield it, but it will not govern the

107

intersection scenario. Nevertheless, anisotropy of in-situ stresses may impede or facilitate debonding in front of the growing fracture.

In case of anisotropic in situ stresses, the required stress for debonding the parallel natural fractures ($S_{h,min}$-P_p-$\sigma_{t,cement}$, where P_p is the pore pressure and $\sigma_{t,cement}$ is the tensile strength of the cement) is less that the required stress for debonding orthogonal natural fractures ($S_{H,max}$-P_p-$\sigma_{t,cement}$). Therefore, it is more likely to reactivate parallel natural fractures by hydraulic fracturing in anisotropic reservoirs.

The path followed by the fracture in the presence of the parallel debonded area is sensitive to the tectonic stress anisotropy (Figure 3.24). In case of isotropic or low anisotropic in-situ stresses, the hydraulic fracture is advancing toward the natural fracture with a high angle. But as the differential stress increases, the hydraulic fracture will have lower tendency for coalescence into the parallel natural fractures. It can be concluded that high anisotropic in situ stress state facilitates reopening of parallel natural fracture, but since they cannot coalesce with the main hydraulic fracture, they will not contribute to the wellbore production enhancement.

The curvature of the miss-aligned section of the hydraulic fracture depends on the stress anisotropy (compared in Figure 3.24) and the length of debonded zone. The extra curvature will reduce fracture effective length and increase pressure drop along the fracture. Both of these issues will not improve the efficiency of the fracturing treatment.
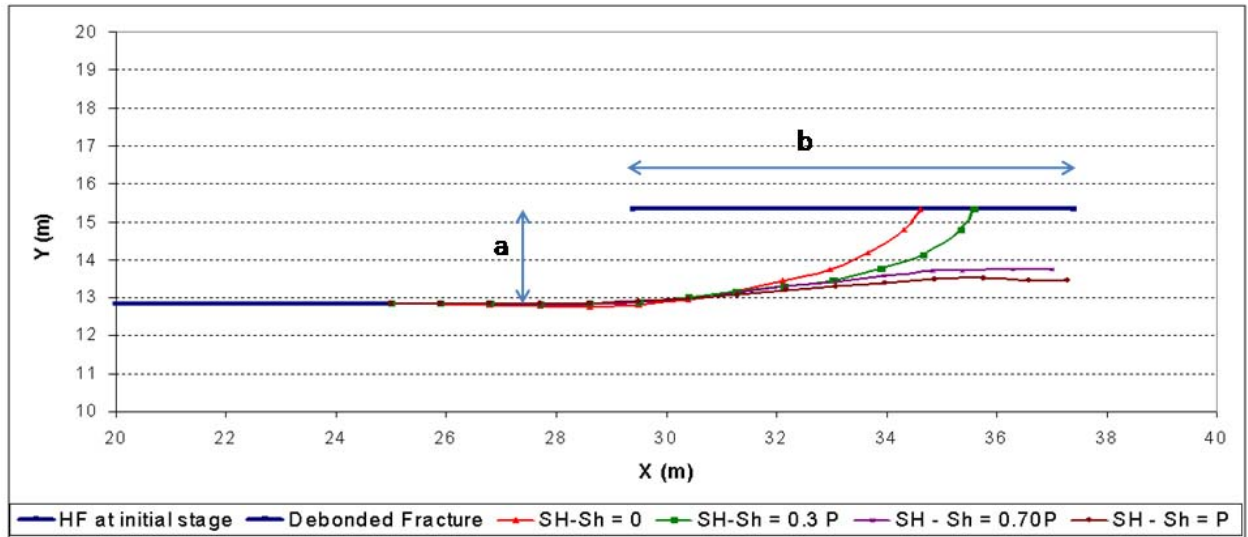
Figure 3.24. The effect of anisotropy of in-situ stresses on the interaction between a growing hydraulic fracture (from left to right) and a debonded natural fracture. Thick blue lines show the initial fractures. The effect of stress anisotropy is demonstrated in the associated plots for a/b = 0.30.

In the last couple examples, the interaction between an advancing hydraulic fracture and surrounding open natural fractures before their coalescence was discussed. Depending on the size of the open part of the natural fracture, fractures coalescence could affect the fracturing job. As the primary hydraulic fracture reaches an open natural fracture, due to the strain relaxation at the tip of the approaching fracture, extra volume will be provided inside the fracture. As an example, consider that the length of natural fracture is about 40% of the hydraulic fracture length and horizontal in-situ stresses are isotropic. Figure 3.25 shows the opening profile of the primary hydraulic fracture before crack intersection (geometry of Figure 3.2.a), at the time of the intersection and at the time when enough pressure build-up for further propagation (geometry shown in Figure 3.2.c). Immediately after the intersection, 16.7% in this case is added to the initial

109

fracture volume. To be able to maintain enough pressure for fracture propagation, it is necessary to pump almost the same amount of fluid as was inside the non-intersected fracture (102.2% of initial fluid volume). It is noticeable that major part of the excessive volume is provided inside the primary fracture (about 85%).

This observation may explain the high leakoff rates and the large amount screenouts reported in the field during hydraulic fracturing in the fractured reservoirs (e.g. Nolte and Smith 1979, Warpinski, 1990).
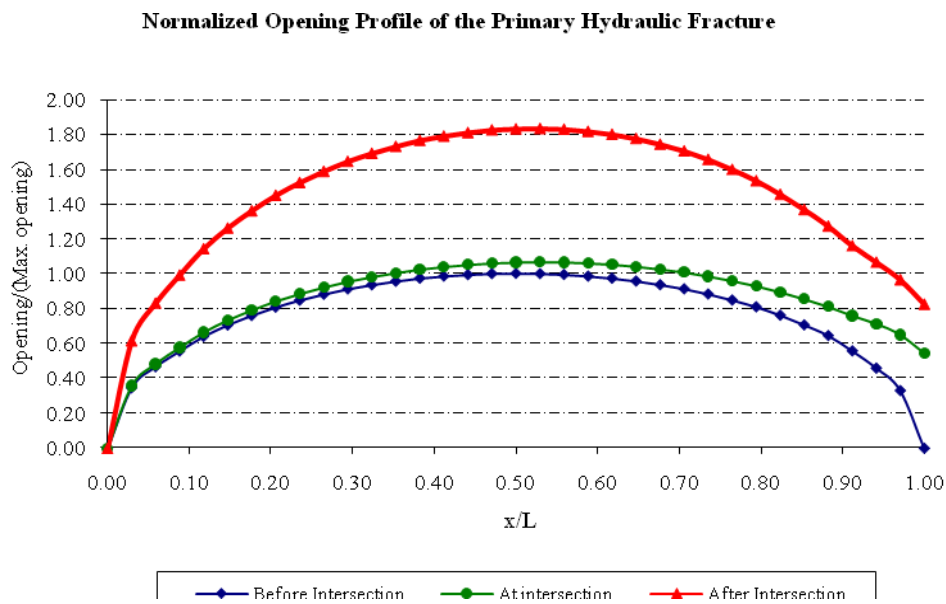
Figure 3.25. Fracture profile before, at and after intersection with an un-cemented (or activated fracture).

3.8. Conclusion

The interaction between a growing hydraulic fracture and surrounding natural fractures were studied in this chapter. New energy criterion was proposed to determine

the orientation of fracture propagation. Generally, three possibilities might occur while fracturing a fractured reservoir. First, the natural fractures may have no influence and the hydraulic fracture will propagate in the direction normal to the minimum horizontal stress. In this case, the cement bond strength is greater than or close to the matrix rock strength and natural fractures are orthogonal or close to orthogonal to the direction of the maximum horizontal stress. In the second scenario, the system of natural fractures will divert the advancing hydraulic fracture, and natural fractures are ultimately extended by the intersected hydraulic fractures. The dominant factor on fracture behavior in this case is the ratio G_{frac}/G_{rock} that depends on the cement toughness and natural fractures orientation angles with respect to the primary hydraulic fracture. Therefore, the orientation of the present-day in-situ stresses with respect to the natural fractures set is another major factor that dominates the efficiency of the hydraulic fracturing treatment. In the third scenario, the growing hydraulic fracture exerts large enough tractions on the surrounding natural fractures, which may re-activate natural fractures even without intersection and lead to the formation of double-deflected fractures after primary fracture reaches the debonded zone. It was shown that when natural fractures are perpendicular to the direction of the hydraulic fracture growth, the largest possible debonded zone may form, which is equivalent to the most optimum case to stimulate a reservoir.

The effect of in situ stress anisotropy on natural fractures reactivation was also discussed. In situ stress anisotropy may increase the possibility of debonding parallel natural fractures, but stress anisotropy prevents the debonded zones to coalesce with the hydraulic fracture, so they will not enhance well performance. The new induced parallel

open natural fractures increase the apparent toughness of the earth. Simillar increase in apparent toughness has been observed in natural fracture swarms by Olson (2004).

The coalescence of the hydraulic fracture with open natural fractures causes strain relaxation at the reaching tip, which provides larger volumes mainly inside the primary hydraulic fracture and then the connected natural fracture. It was shown in an example that after intersecting open natural fractures, it might be needed to inject several times larger than amount of already pumped fluid into the system to be able to maintain enough pressure for continuing fracturing job. These episodes may be observed as high screenouts for operators on the surface.

The fracture propagation modeling demonstrated using Extended Finite Element and propagation models for cemented fractures are keys to enable proper hydraulic fracture design analysis by considering prescribed fractures geometry. However, modeling the reactivation of open mode fractures in naturally fractured reservoirs requires to have the natural fracture system characterized. There exist some integrated models in the literature that can be utilized for this purpose (e.g. Laubach et al. 2000). By combining the knowledge of natural fracture patterns, cement properties and today's in-situ stresses, it is possible to build a model to make a realistic prediction about the hydraulic fracturing efficiency.

To investigate other aspects of this problem like gel damage to the reservoir due to the incomplete washout processes and other complicated behavior of the interaction between hydraulic fracture and natural fractures requires including coupling the fluid

flow, proppant transpost and rock deformation which could be a subject for further studies.

Chapter 4. Coupled Modeling of Hydraulic Fracture Propagation

In the previous chapters, the role of the fluid flow component of the hydraulic fracturing problem was neglected. As discussed before, uniform pressure assumption was used for fracture networks, which is equivalent to a zero viscosity assumption for the fracturing fluid. There are some aspects of the problems hidden in the fluid flow part of the problem, such as issues raised by pressure changes along the fracture length. It would be of great importance to solve the fluid flow equation and elasticity equations simultaneously.

This chapter begins with an introduction to the problem and derivation of the governing equations. Issues such as boundary conditions and their consequent effects is studied in detail. Then appropriate numerical schemes to solve this problem in the framework of Extended Finite Element Methods (XFEM) will be established. A few examples will be considered. Their results will be compared with solutions available in the literature to validate the model. After fractures coalesce, the hydraulic fracture mode may change from pure mode one to mixed modes one and two. It will be shown how this change may contribute to difficulties in fracturing fluid penetration and to a reduction in fracture width.

4.1. Coupled Hydraulic Fracturing Model

Mathematical modeling of fluid-driven fractures has attracted many contributions, which are aimed at predicting the evolution of treatment pressure, induced fracture length and width, and geometry of the fracture system. The fluid injection rate, in situ stresses, fluid rheology and rock mechanical properties are input data for such models. Classical papers on this subject have used simplified assumptions about the fracture geometry (Khristianovic and Zheltov, 1955, Barenblatt, 1962, Geertsma and de Klerk 1969, Weertman, 1971, Spence and Turcotte 1985).

In general, solutions for fluid-driven fractures are tremendously difficult to construct even for simple geometries. This difficulty is due to moving boundary conditions, non-linearity of the governing equation for fluid flow in fractures, the high gradient of displacement near the fracture tip, and non-locality of the solution. Non-linearity comes from the fact that fracture permeability is a cubic function of the fracture width. Non-locality means that the fracture opening at one point is a function of fluid pressure at another point along the fracture (Detournay, 2004). Despite the previous uncoupled simulations, the process leads to a time dependent varying pressure distribution. Additionally, the fracture grows with an unknown speed, which may also vary with time.

The hydraulic fracturing model simulates the manner in which fracture length, width and frac-fluid pressure distribution evolve with time. This procedure required consideration of three issues: (1) Fracture fluid pressure build-up in a partially filled

stationary fracture; (2) Fracture fluid front advancement inside the crack; and (3) Crack propagation with moving fluid.

A typical cross section of a hydraulic fracture is shown in Figure 4.1. The governing equations are those of elasticity, mass conservation, fluid rheology and fluid leak-off, as well as crack propagation criteria. Here, the effect of fluid leak-off was neglected without a loss of generality as the incorporation of leakoff does not involve a new conceptual complexity. It should be noted that these governing equations are coupled to each other and hence need to be solved simultaneously as the system evolves with time.
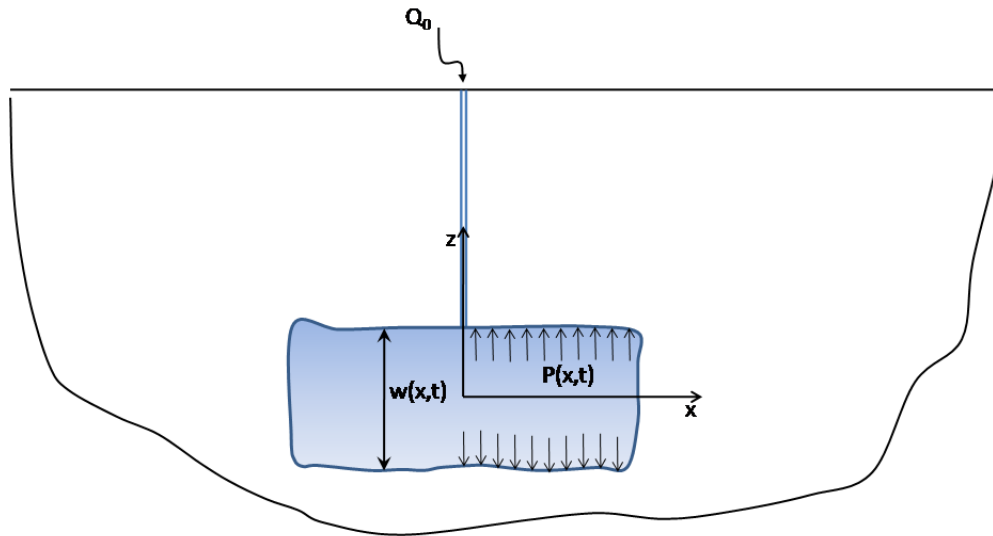
Figure 4.1: Schematic geometry of the hydraulic fracturing treatment.

This research is focused on understanding and modeling the possible effect of pre-existing fractures on the propagation of hydraulic fractures. In naturally fractured

reservoirs, a hydraulic fracture can be arrested or decelerated as a result of diversion and frictional sliding along the pre-existing fractures, because fluid penetration through frictionally pre-existing fractures is difficult. A competition between crack propagation from secondary flaws and debonding of the natural fracture plays an important role in determining the direction of the hydraulic fracture growth. Before going into further detail, the governing equations of this process are reviewed.

4.2. Governing Equations

For the sake of simplicity, it is assumed that fractures are propagating in an isotropic, impermeable linear elastic medium under plane strain conditions, and that the fracture is driven by an incompressible Newtonian fluid from a source located somewhere along the fracture (i.e. the wellbore). Crack propagation is always assumed to be quasi-static. Given that fluid is injected into the fracture at a constant volumetric rate Q_0, the goal is to determine the fracture length as a function of time, and the fracture opening and fluid pressure as functions of time t and location (x,y).

For an incompressible Newtonian fluid, neglecting gravitational forces, the equations of motions can be written as (Currie, 2003)

$$\rho(\frac{\partial u}{\partial t} + u\frac{\partial u}{\partial x} + v\frac{\partial u}{\partial y}) = -\frac{\partial P}{\partial x} + \mu(\frac{\partial^2 u}{\partial x^2} + \frac{\partial^2 u}{\partial y^2}) \qquad (4.1)$$

$$\rho(\frac{\partial v}{\partial t} + u\frac{\partial v}{\partial x} + v\frac{\partial v}{\partial y}) = -\frac{\partial P}{\partial y} + \mu(\frac{\partial^2 v}{\partial x^2} + \frac{\partial^2 v}{\partial y^2}) , \qquad (4.2)$$

117

where x and y are local coordinate system in the fracture (y-direction refers to the width direction and x-direction refers to the direction along the fracture.), ρ is the density of the fluid, $u(x,y,t)$ and $v(x,y,t)$ are the components of the velocity in the x and y direction, $P(x,y,t)$ is the net pressure distribution within the fluid and μ is the viscosity of the fluid. For a crack whose length is aligned with the x-axis, the y-dimension is so small compared to the **x**-dimension that the net pressure can be considered uniform i.e. $\partial P/\partial y = 0$. Therefore, P is only a function of x and t. Away from the crack tip the fluid velocity along the crack, u, is orders of magnitudes larger than the fluid velocity normal to the plane, v, and can be neglected. This is equivalent to the laminar flow assumption for fluid flow inside the fracture. By using dimensional analysis, it is possible to show that for a low Reynolds number and for a small inertia term, the above equations reduce to

$$\frac{\partial P}{\partial x} = \mu \frac{\partial^2 u}{\partial y^2}, \tag{4.3}$$

and the average velocity, $\underline{u}$, can be calculated from

$$\underline{u} = -\frac{w^2}{12\mu} \frac{\partial P}{\partial s}. \tag{4.4}$$

Consequently, the fluid flow part of the problem is reduced to a one dimensional problem. Hereafter, s is used rather than x for the dimension along the crack. Therefore, the fracture is not required to be a straight fracture. Justification for this argument is given in Appendix A.

By considering the same assumptions considered for the equations of motion, the mass conservation equation can be written for an infinitesimal element of fluid and then simplified to

$$\frac{\partial w(s,t)}{\partial t} + \frac{\partial q(s,t)}{\partial s} = Q_0 \delta(s),$$ (4.5)

where $\delta(s)$ is the Dirac delta function. It is remarkable that equation (4.5) is a local continuity condition. By substituting the mass conservation equation into the equation of motion, the lubrication equation (Batchelor, 1967) can be obtained

$$\frac{\partial w(s,t)}{\partial t} = \frac{1}{12\mu} \frac{\partial}{\partial s} (w^3(s,t) \frac{\partial P(x,t)}{\partial s}),$$ (4.6)

which is true whenever $(\frac{\rho q}{\mu}) \frac{w}{h} \lll 1,$ where h is the fracture height. Additionally, $w(s,t)$ is the fracture width at point s and time t; ρ is the fluid density, q is the flux per unit height and μ is the fluid viscosity. Nilson (1981, 1988) and Spence and Sharp (1985) discussed the validity and limits of the lubrication approximation for the fluid flow description inside the fractures (cavities). Based on their analysis, fluid flow should be laminar, and the width of the fracture should be small in comparison to the other dimensions of the fracture.

The boundary conditions at the wellbore are that the fluid flux is equal to the injection rate,

$$q(0) = Q_0.$$ (4.7)

At the fracture tip, the fracture opening displacement is zero *w(l)=0*. In addition, it is assumed that there is no flow at the fracture tip so $q(l) = 0$. Substituting this condition in equation (4.3), zero flux at the tip can be interpreted as

$$w^3(t)\frac{\partial P(t)}{\partial x} = 0, \qquad \text{at } x = l. \tag{4.8}$$

A primary difficulty of hydraulic fracturing problems comes from the coupling of the fluid flow inside the fracture and the equation governing the opening of the fracture. To address this problem, an iterative process is designed to obtain the solution.

At the beginning of each time step, the net pressure distribution is assumed to be known (which is usually the net pressure distribution of the previous time step). For the first time step, a uniform net pressure distribution is assumed. The width distribution along the fracture is calculated using the quadratic extended finite element method (XFEM). A new fluid net pressure distribution, *P*, is determined by solving equation (4.6) using the calculated width and boundary conditions (4.7) and (4.8). This process is repeated until reaching the convergent solution.

4.3. Discretization of the Flow Equation

The standard Galerkin finite element method is utilized to solve equation (4.6). The fluid net pressure inside the fracture is approximated by

$$p(s) = \sum_{i-1}^{\hat{N}}\varphi_i(s)p_i, \tag{4.9}$$

where $\varphi_i(s)$ is the shape function for node i, and P_i is the corresponding nodal value for the net pressure at node i. In the case of linear elements, the pressure gradient will be constant within each element; however, the precision of fluid pressure gradient is important because it determines the fluid flux inside the fracture. Thus a lack of precision in the calculation of the pressure will have a domino effect on the accuracy of the results. Quadratic elements are used for fluid flow to improve the numerical accuracy of the results. The variational (weak) form of the equation (4.6) is

$$\int_L \frac{\Delta w}{\Delta t} \varphi_i(s)ds + \int_L q_L(t)\varphi_i(s)ds = \frac{1}{12\mu}\int_0^L \frac{\partial}{\partial s}(w^3 \frac{\partial P}{\partial s})\varphi_i(s)ds , \qquad (4.10)$$

where q_L is the flux rate of the fluid loss to the formation. Fluid-loss is not considered in this research but it is included in the formulation to include a more general case. Integrating the right hand side of equation (4.10) by parts results in

$$\frac{1}{12\mu}\int_{-L_1}^{L_2} \frac{\partial}{\partial s}(w^3 \frac{\partial P}{\partial s})\varphi_i(s)ds = \frac{1}{12\mu}w^3 \frac{\partial P}{\partial s}\varphi_i(s)\Big|_{-L_1}^{L_2} - \frac{1}{12\mu}\sum_{j-1}^{\hat{N}}\int_{-L_1}^{L_2} P_j w^3 \frac{\partial \varphi_i}{\partial s}\frac{\partial \varphi_j}{\partial s}ds . \quad (4.11)$$

The flux rate specified at the wellbore implies the following boundary condition,

$$\frac{1}{12\mu}w^3 \frac{\partial P}{\partial s}\varphi_i(s)\Big|_0 = Q_0\varphi_1(0) . \qquad (4.12)$$

Considering zero opening at the fracture tip implies that

$$\frac{1}{12\mu}w^3 \frac{\partial P}{\partial s}\varphi_i(s)\Big|_{-L_1,L_2} = 0 , \qquad (4.13)$$

where L_1 and L_2 are the position of the fracture tips with respect to the wellbore located at $s = 0$. In cases where the position of the fluid front L_f is different from the fracture tip,

121

the condition $P = 0$ should be satisfied at the fluid front. One may assume that fluid lag may always exist behind the fracture tip but its length is sometimes negligible. This assumption implies using a zero boundary condition at the fracture tip. It is notable that the above boundary conditions are not sufficient at the crack intersections. For those situations, some modifications are applied. Based on the derived weak form, equation (4.11) can be rewritten as

$$C_{ij}P_j = f_i, \tag{4.14}$$

where

$$C_{ij} = \frac{1}{12\mu}\sum_{j-1}^{\hat{N}}\int_{L_1}^{L_2} w^3 \frac{\partial \varphi_i}{\partial s}\frac{\partial \varphi_j}{\partial s}ds \tag{4.15}$$

and

$$f_i = \int_L \frac{\Delta w}{\Delta t}\varphi_i(s)ds + \int_L q_L(t)\varphi_i(s)ds, \tag{4.16}$$

where the matrix C is indirectly dependent on P by its relation to w. Using the current values of P and w to evaluate C, the above equation is solved for a new net pressure P. Here, C is a function of width (w) only. In the case of more complicated fluid models such as power-law fluids, C depends on net pressure as well. The formulation for the power-law fluid is given in Appendix B.

The fluid flow elements are always treated as straight elements. Therefore, the element size should be small enough to accommodate the error caused by this smoothing process in curved fractures.

122

The lubrication equation (4.6) is a second order differential equation with respect to P and requires two boundary conditions to be solvable. Choosing the second boundary condition is crucial as it affects the strategy for solving coupled elasticity and fluid flow equations. Note that the zero-flux boundary condition is applicable if and only if the fluid occupies the whole fracture volume and no lag exists between the fluid front and fracture tip. In the case of fluid lag, net pressure in the lag zone will be zero, or more precisely, equal to the pore pressure in the formation. Later in this chapter, it will be shown that a pressure boundary condition at the tip will not affect fluid flow far from the tip.

From the lubrication equation (4.6), it can be seen that the pressure gradient becomes infinite as $s \to L$ because $w \to 0$. Based on the asymptotic solutions from linear fracture mechanics, fracture opening, w near the crack tip is proportional to the square root of the distance from the fracture tip

$$w \propto \sqrt{r} \; . \tag{4.17}$$

From the Poiseuille's flow equation, the fluid velocity near the tip is proportional to

$$u \propto w^2 \frac{\partial P}{\partial r} . \tag{4.18}$$

Since the velocity of the fluid is supposed to be constant in the steady state regime, then $\frac{\partial P}{\partial r} \propto \frac{1}{w^2}$. By substituting equation (4.18) for fracture opening into the previous equation and integrating, there will be

$$p \propto \ln(r) . \tag{4.19}$$

This means that net pressure has a singular logarithmic behavior near the fracture tip. The negative net pressure near the fracture tip provides a very small suction zone with pressure less than the reservoir pressure.

In the above asymptotic analysis, leakoff was not included. In the case of leakoff, equation (4.18) cannot be true. Therefore, the validity of equation (4.19) is limited to impermeable formations. Additionally, this analysis is for the cases where the LEFM assumptions of linear elasticity and small deformation/displacement near the crack tip can be used. It is possible that net pressure would be smaller than the closure stress in some parts of the fracture and still has positive opening displacements. Thus, it may be concluded that the zero net pressure boundary condition could not be a realistic assumption for near fracture tip studies, but the length of the zone with negative net pressure is very small compared to the fracture length. Thus, a zero net pressure boundary condition has been used by several authors (for instance Yew and Liu, 1993 and Siebrits and Peirce, 2000). The difficulties that exist in applying the zero flux boundary condition make this approach more attractive.

One of the complications of the zero flux or only Neumann boundary condition is that the stiffness matrix C introduced in (4.15) is not invertible and the solution for p is unique up to an arbitrary constant. To remove this indeterminacy, it is needed to add a constraint to equations by imposing the global conservation of mass into the problem

$$\int_L w\,dx = \int_t Q\,dt \,. \tag{4.20}$$

It is noteworthy that equation (4.5) is the local continuity condition, and the equation (4.20) is a global conservation of mass. The solvability condition (4.20) plays an important role in the design of efficient schemes to solve the coupled equations (4.14) and (4.20) because of the pressure indeterminacy of the fluid flow equation.

4.4. Coupling Fluid Flow and Rock Deformation

The elasticity, fluid flow and fracture growth equations should ideally be fully coupled in order to solve the system of equations correctly. In this part, an algorithm is introduced to solve the elasticity and fluid flow equations given by

$$\mathbf{K}d = P - \sigma_{in-situ} \text{ and} \tag{4.21}$$

$$\frac{\Delta w}{\Delta t} = CP + S, \tag{4.22}$$

for P and w. The variable d in equation (4.21) is the displacement vector, which is used for calculating the fracture opening Δw. The vector $\mathbf{S}$ in equation (4.22) is the source/sink vector associated with injection sources and probable leak-offs. $\mathbf{K}$ is the elastic stiffness matrix for fractured medium calculated and defined in the framework of Extended Finite Element Methods (X-FEM) as

$$\mathbf{K} = \int_{\Omega^h} \overline{\mathbf{B}}^{\mathrm{T}} D \overline{\mathbf{B}} \, d\Omega,$$

which is equation (2.25). To avoid confusion with matrix C in equation (4.22), the character D is used for the elastic property matrix. Further explanations about this

125

equation can be found in chapter 2. The coupled equations (4.21) and (4.22) are fully nonlinear due to the presence of the term w^3 in the flow equation.

In order to solve the system of equations (4.21) and (4.22), it is necessary to use an algorithm that involves the inversion of the global stiffness matrix. Given a trial solution (w_k, p_k), a fixed point strategy based on this approach involves solving the fluid flow equation for p_{k+1}, which is then used in equation (4.21) to determine w_{k+1}. In order to stabilize this process, the following sequence of Picard iterations is implemented

$$p_{k+1/2} = C(w_k)^{-1}\left(\frac{\Delta w_k}{\Delta t_k} - S\right), \qquad (4.23)$$

$$p_{k+1} = (1-\alpha)p_k + \alpha p_{k+1/2}, \qquad (4.24)$$

$$d_{k+1} = K^{-1}(p_{k+1} - \sigma_c) \text{ and} \qquad (4.25)$$

$$d_{k+1} \to w_{k+1} \qquad (4.26)$$

This approach is inspired by the methods built by Yew et al. (1988) and Adachi et al. (2007), which used Picard iteration to solve this coupled problem. They modify both net pressure and fracture width at each iteration, so that the fracture width used for fluid flow calculations is not exactly the width calculated by the fracture mechanics model. To avoid this discrepancy in the presented model, only net pressure (not fracture width) is modified using equation (4.24). Fracture width changes in this model are directly calculated based on the modified pressure from the previous iteration. To implement this procedure, it is necessary to make **C** invertible by imposing the global mass conservation condition (solvability condition). Using the fixed point theorem, this process can be

shown to converge for $0 < \alpha < 0.50$ provided the time steps are small enough (Liao et al. 2007). The validity of this analysis is not affected by only updating pressure.

The convergence of iterations is examined with the average error in the pressure distribution in all elements. This criterion is written as

$$\frac{\sum_{i=1}^{\hat{N}} \left| P_i^{(n)} - P_i^{(n-1)} \right|}{\sum_{i=1}^{\hat{N}} \left| P_i^{(n)} \right|} \leq \varepsilon, \tag{4.16}$$

where ε is the predetermined tolerance, and $P_i^{(n)}$ is pressure at node i in iteration n. The time step in the simulation is determined from the total mass balance

$$Q_0 = \int_0^L \frac{\Delta w}{\Delta t} ds + \int_0^L q_L ds. \tag{4.17}$$

The flowchart to implement the algorithm for zero pressure boundary condition at the fracture tip is shown in Figure 4.2. One limitation to the Picard iteration technique is that the initial value used in the iteration must be close to the correct answer. However, using the pressure from the previous step seems to be sufficient.

In this chapter, only the fluid flow boundary conditions are discussed. Additional boundary conditions for solid part of the problem are also required. Rollers were used to constrain normal deformations at the boundaries. For the propagation part of the problem, the stress intensity factors were used in Erdogan-Sih's (1963) criterion to determine the orientation of the hydraulic fracture propagation. It should be noted that in discretization of the problem, there is no need to have solid and fluid nodes to coincide on each other.

But to minimize the projection error between solid and fluid elements, it is better to choose elements of the same order.

The stiffness matrix calculated by XFEM is independent of loading and depends only on the fracture geometry. The XFEM stiffness matrix needs to be calculated once at the beginning of each time step. This leads to a significant saving in computation time.
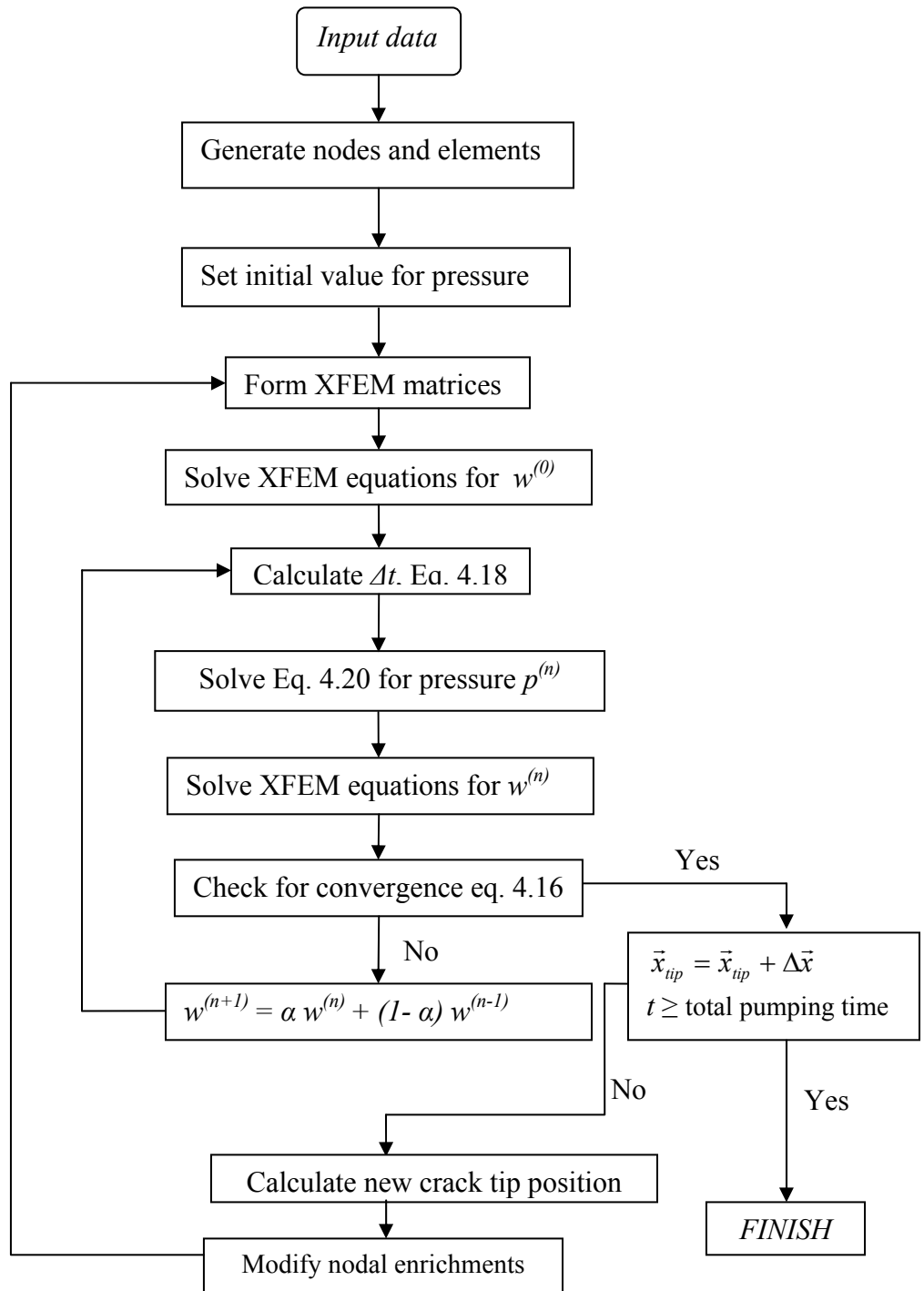
Figure 4.2: Flowchart for the numerical scheme to simulate hydraulic fractures propagation.

129

4.5. Numerical Examples and Discussion

A variety of numerical simulations have been carried out, and the results of these simulations indicate that the numerical strategy is well-behaved and possesses a rapid rate of convergence. Here, results for different cases are presented in order to illsutrate the power of the model.

Because of the complexity of the hydraulic fracturing problem, there is no exact solution for verification of the model accuracy beyond the simplest examples. For a two dimensional fracture with a Newtonian fluid, Geertsma and de Klerk (1969) obtained an approximate solution. The expression for fracture length, fracture opening at the wellbore, and net pressure-were derived as

$$L(t) = 2\left[\frac{16}{21\pi^3}\frac{E'q_0^3}{\mu}\right]^{\frac{1}{6}}t^{\frac{2}{3}} = 2.0*0.539\left[\frac{E'q_0^3}{\mu}\right]^{\frac{1}{6}}t^{\frac{2}{3}}, \qquad (4.18)$$

$$w_{well}(t) = \left[\frac{5376}{\pi^3}\frac{\mu q_0^3}{E'}\right]^{1/6}t^{\frac{1}{3}} = 2.36\left[\frac{\mu q_0^3}{E'}\right]^{1/6}t^{\frac{1}{3}} \text{ and} \qquad (4.19)$$

$$\Delta p_w = \left[\frac{21}{16}\mu E'^2\right]^{\frac{1}{3}}t^{-\frac{1}{3}} = 1.09\left[\mu E'^2\right]^{\frac{1}{3}}t^{-\frac{1}{3}}, \qquad (4.20)$$

where E' is plane-strain modulus of elasticity ($E' = \dfrac{2G}{1-\nu}$), and q_0 is the injection rate per unit height of the fracture ($q_0 = Q_0/h_f$). Geertsma's model uses the smooth closing surfaces assumption as the boundary condition at the crack tip ($\partial w(L,t)/\partial x = 0$), which is in accordance with Barenblatt's model for cohesive cracks. Therefore, results are not necessarily similar to the results of the model with the zero pressure boundary condition

130

at the tips. Geertsma also assumed that the flow rate is everywhere equal to the injection rate, so he neglects fluid storage in the fracture as the width changes with time. Since pressure in Geertsma's model is net pressure, no in situ stress was assumed in this model to make comparison easier. However, the presented model is capable of handling anisotropy of in situ stresses.

For a 12 minute constant rate injection of a Newtonian fluid (Table 4.1 has the details of the input), the XFEM numerical model shows good agreement with the analytical solution (Figures 4.3, 4.4 and 4.5). The fracture length and net pressure results are almost a perfect match, while the XFEM model predicts a slight higher width at later time than the Geertsma model. The reason that XFEM model predicts different width is probably due to neglecting the storage effect by the simplifying assumption that Geertsma's has made with constant flow rate inside the fracture. This discrepancy has also been reported in Yew et al. (1988). The execution time for this example is described in Appendix C.

Young's modulus (**E**)	4.0×10^6 psi
Shear modulus (**G**)	1.6×10^6 psi
Poisson's ratio (**v**)	0.25
Injection rate (**Q$_0$**)	5 bbl/min
Fracturing Fluid viscosity (μ)	100 cP
Fracture Height (**h**)	100 ft

Table 4.1: Details of input data for the first test case.

131

The bottomhole pressure, plotted in Figure 4.3, deserves further attention. It shows that the bottomhole pressure drops with time while the fracture width increases. This result is a consequence of assuming an infinite height for the fracture (KGD geometry), which implies that longer fractures require less pressure to maintain the same opening. In practice, however, the pressure is rarely decreasing because the length of the induced fracture is usually longer than the fracture height, so the fracture height restricts the fracture opening. In the KGD model, the net pressure gradient decreases rapidly with fracture length and reaches an almost constant value. The pressure profile and fracture width distribution along the hydraulic fracture are shown in Figures 4.6 and 4.7 respectively. Pressure drop rate, in both models, is slow near the wellbore, but increases rapidly near the fracture tip. Half of the pressure drop takes place in about 10% of the fracture length down the fracture tip. The large pressure drop at the tip is due to the zero net pressure boundary condition at the fracture tip.

It is important to note that the model has been tested with different initial guesses for the pressure distribution, but the solution converged rapidly to the accepted range. It is able to achieve results with less than 5% percent error in less than 10 iterations. The model is examined for different initial lengths for the hydraulic fracture to make sure that the results were insensitive to the initial length of the hydraulic fracture in the model or the location of the initial fracture with respect to the finite element mesh.
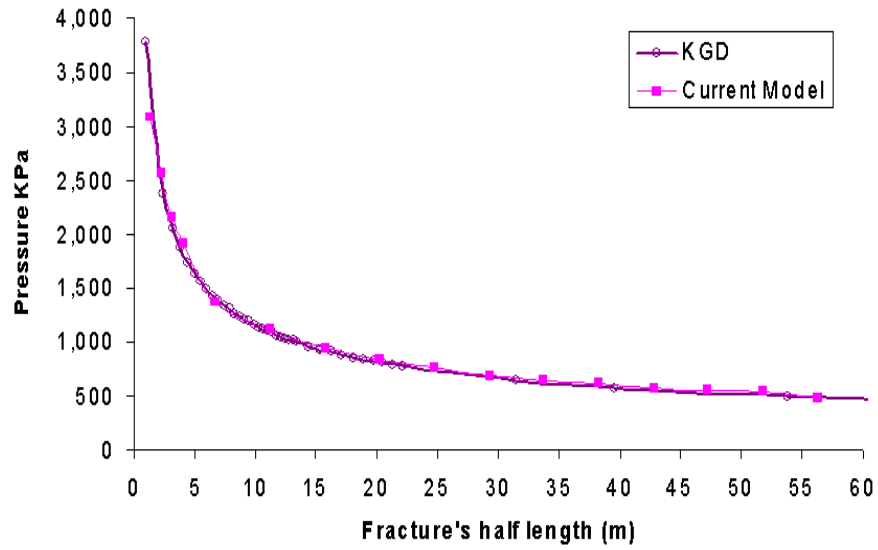
Figure 4.3: Fracture pressure at the wellbore for KGD and the current model.
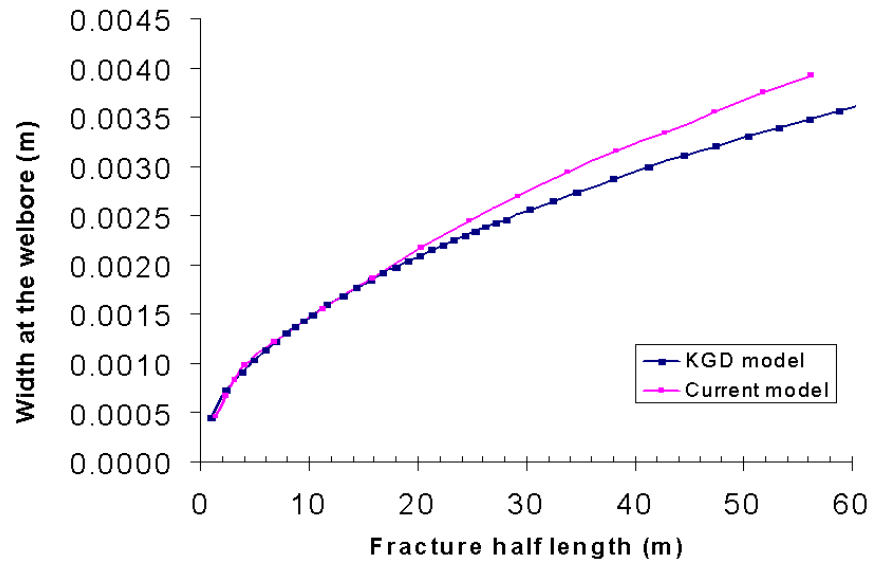
Figure 4.4: Fracture width at the wellbore for KGD and the current model.

133
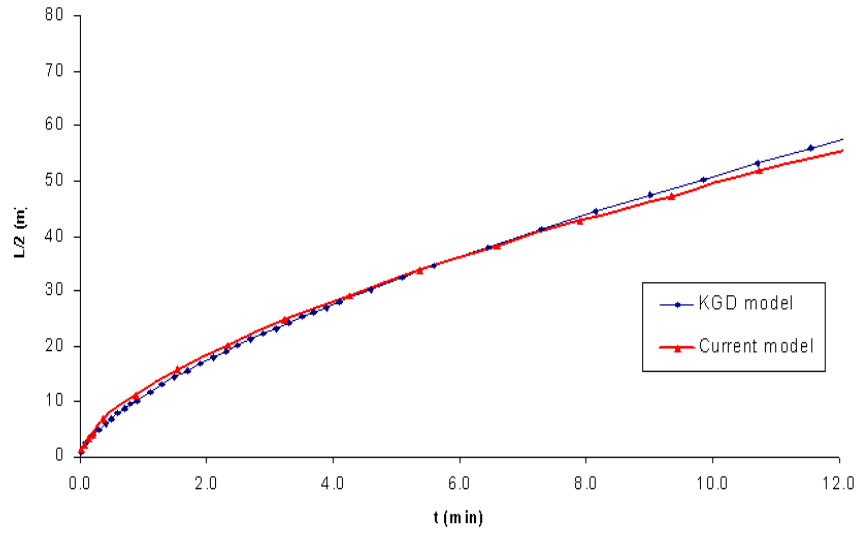
Figure 4.5: Fracture half length versus injection time, computed with current and KGD models.
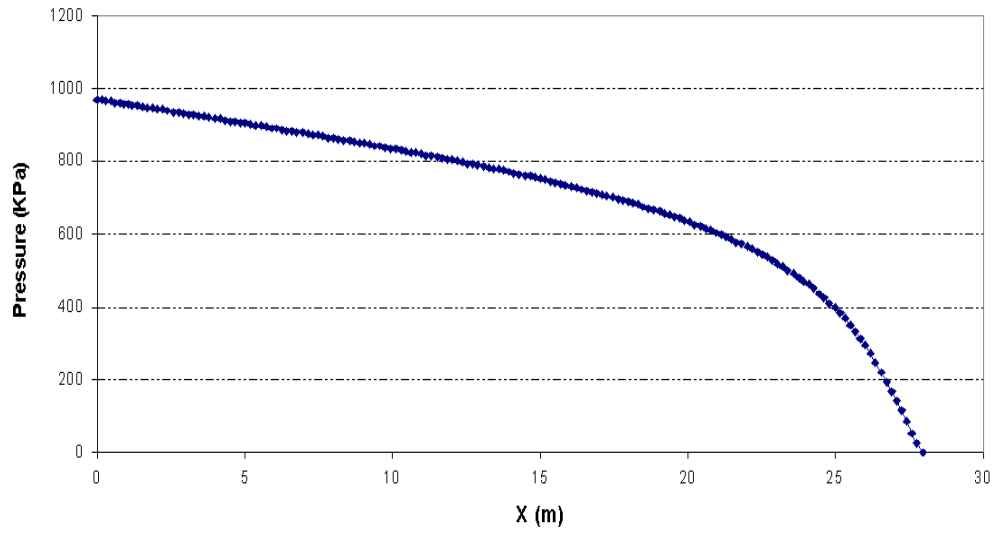
Figure 4.6: Pressure profile in the hydraulic fracture, computed with the presented model.

134
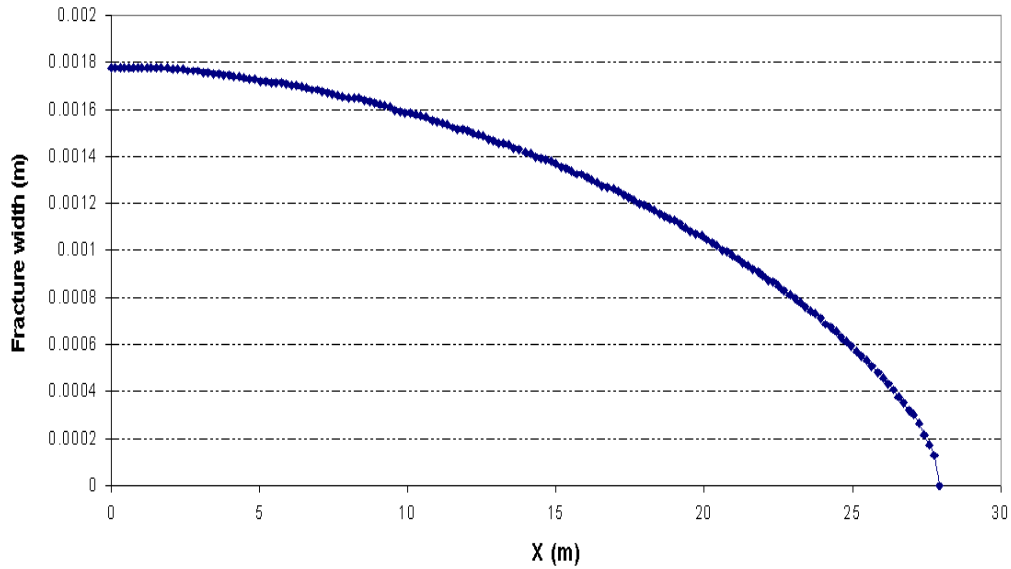
Figure 4.7: Fracture opening profile of the hydraulic fracture, computed with the presented model.

At the beginning of the pumping period, the stress intensity factor grows smoothly until it reaches a constant value (Figure 4.8). The magnitude of stress intensity factor (for instance when L = 19.50 m, $K_I = 4.33 \text{MPa-m}^{1/2}$) is much larger than the common values for rock toughness (for instance $1.00 \text{MPa-m}^{1/2}$ for most Shales (Zimmerman, 2005)). Therefore, it may be concluded that viscosity not toughness is the major dissipating mechanism in this treatment. This observation differentiates a coupled solid-fluid flow simulation from a zero-viscosity simulation presented in the previous chapter. In the case in which fluid flow was neglected, the stress intensity factor at the fracture tip increases with fracture length. In addition, the values for stress intensity

135

factors at the fracture tips were much larger than stress intensity factors calculated by incorporating the effect of fluid flow.
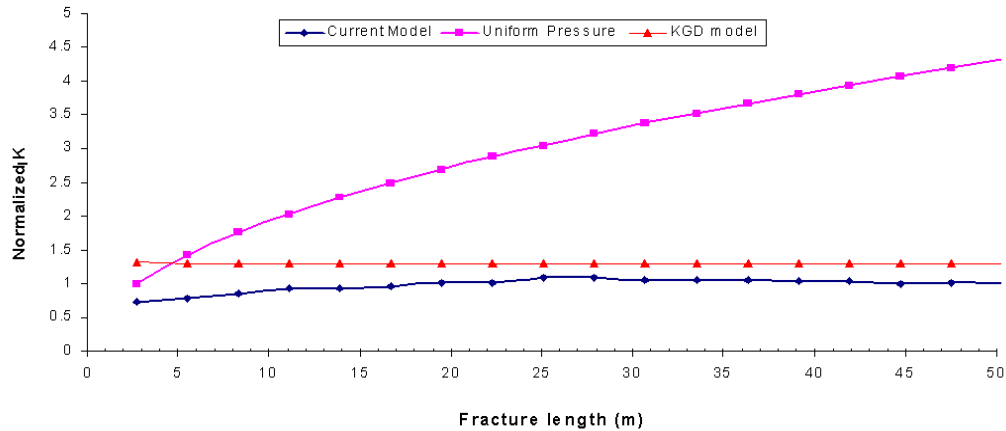
Figure 4.8: The stress intensity factor for current coupled simulation with uniform pressure fluid at different times during injection. The magnitudes are normalized to K_I for uniformly pressurized fracture, where pressure is equal to the wellbore pressure at the initial stage.

The same numerical experiment was repeated with different injection rates to assess its effects. The fracture opening and the pressure profile for these cases are compared in figures 4.9 and 4.10, respectively. A higher injection rate causes higher pressure drop along the fracture, resulting in an overall higher net pressure. And fracture width is greater for higher injection rate because of that higher net pressure. Since, there is a feedback between fracture width, injection rate and pressure, doubling the rate does not double the pressure.
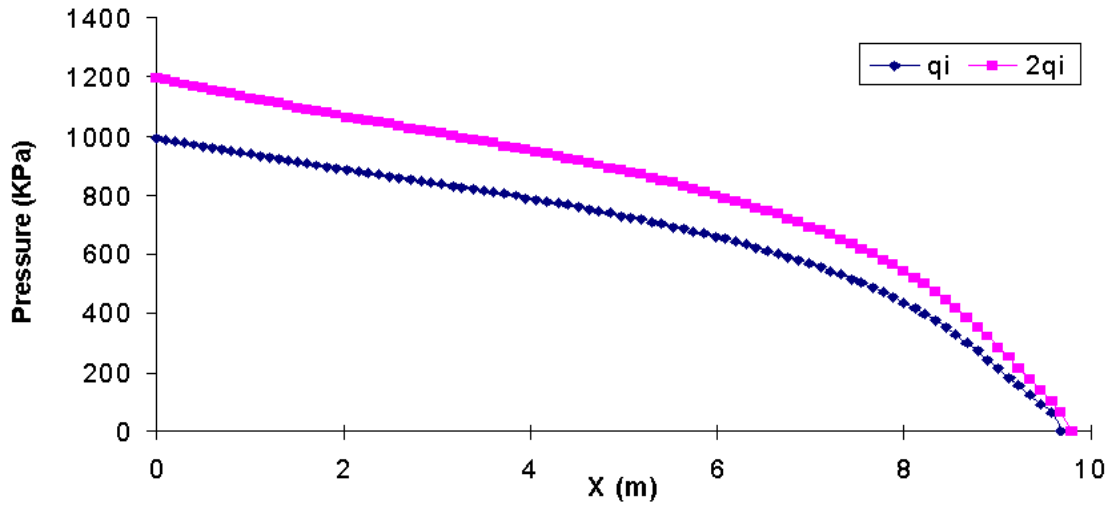
Figure 4.9: The effect of different fluid injection rate on the fracture opening profile.
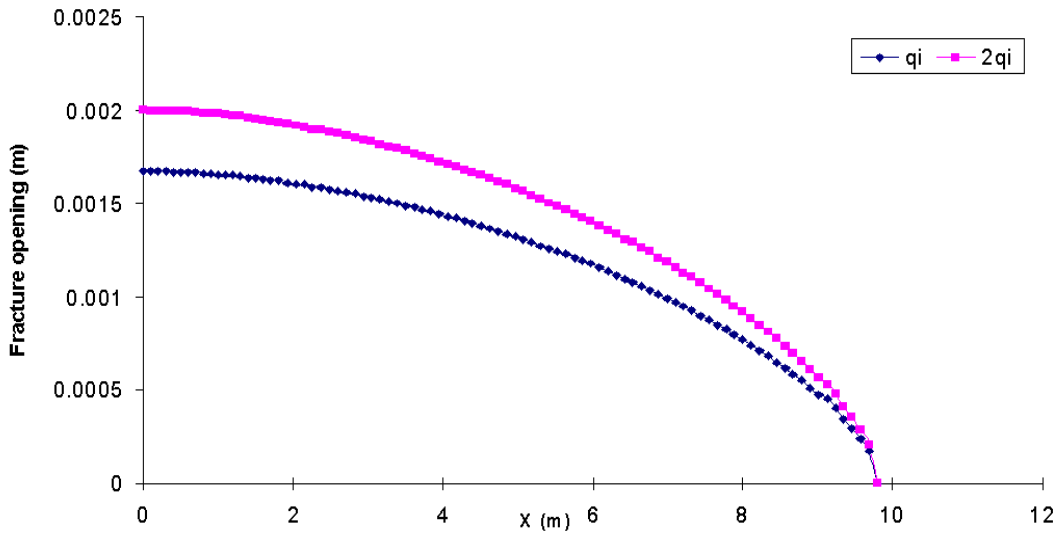
Figure 4.10: The effect of different fluid injection rates on the fracture pressure profile.

Figure 4.11 compares the effect of the fracturing fluid viscosity on the fracture pressure profile. Increasing viscosity will increase fracturing pressure, because of the added resistance to push the fluid down the fracture. However, increasing viscosity does

137

not show any big difference in the fracture pressure distribution near the fracture tip, but for the rest parts of the fracture, the results for fracture pressure are more sensitive to viscosity than to injection rate (Figure 4.10). The same change in response by increasing the viscosity by 50% is obtained as for increasing the rate by 100%. Therefore, it can be concluded that the viscosity should have a high value to induce a larger width, and consequently, better proppant transport during the fracture propagation stage. For this purpose, crosslinkers of the polymer chains have been employed in the industry to increase the viscosity substantially. On the other hand for an equal volume of injected fluid, the effect of increasing treatment-fluid viscosity is to increase the fracture width and decrease its length.
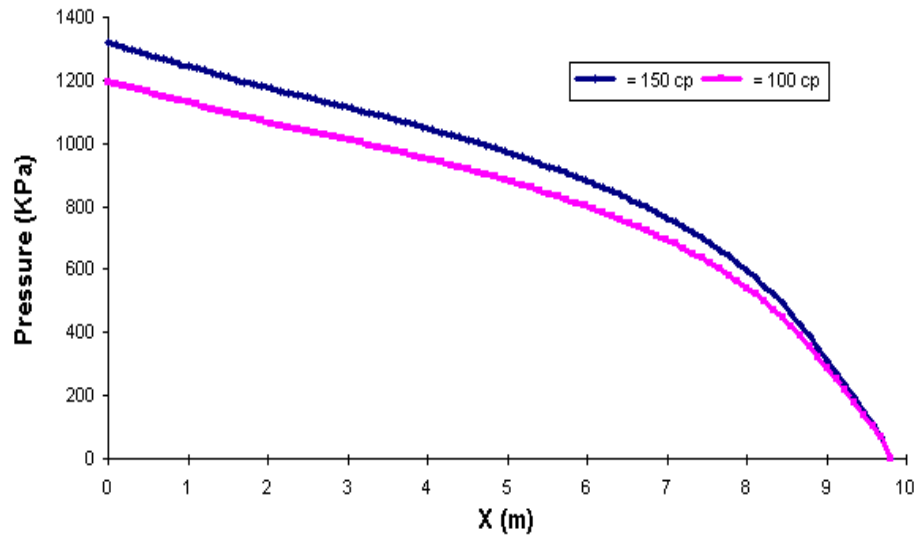
Figure 4.11: The effect of fracturing fluid viscosity on the fracture pressure profile.

This numerical experiment was repeated with a zero flux boundary condition at the fracture tip. The results are similar to the results of the zero net pressure boundary

condition model (Figure 4.12 and Figure 4.13). There are some discrepancies in pressure for early stages when the hydraulic fracture is short, because Geertsma and de Klerk (1969) use cohesive zone at the fracture. The cohesive zone could affect pressure at the wellbore in short fractures, but in longer fractures, the effect of cohesive zone will be limited to the near fracture tip zone.
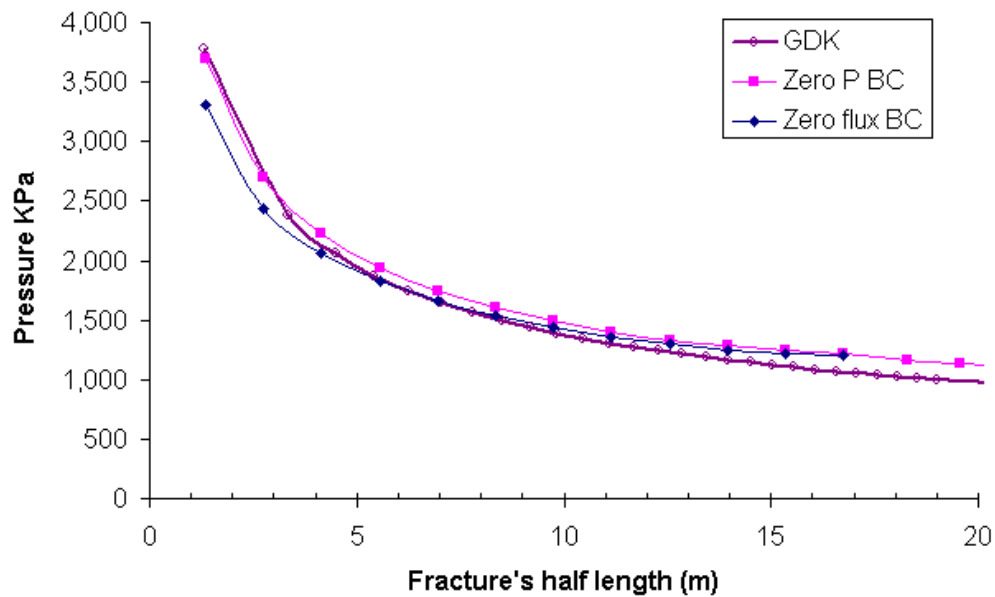
Figure 4.12: Comparison of bottomhole pressures in three models.
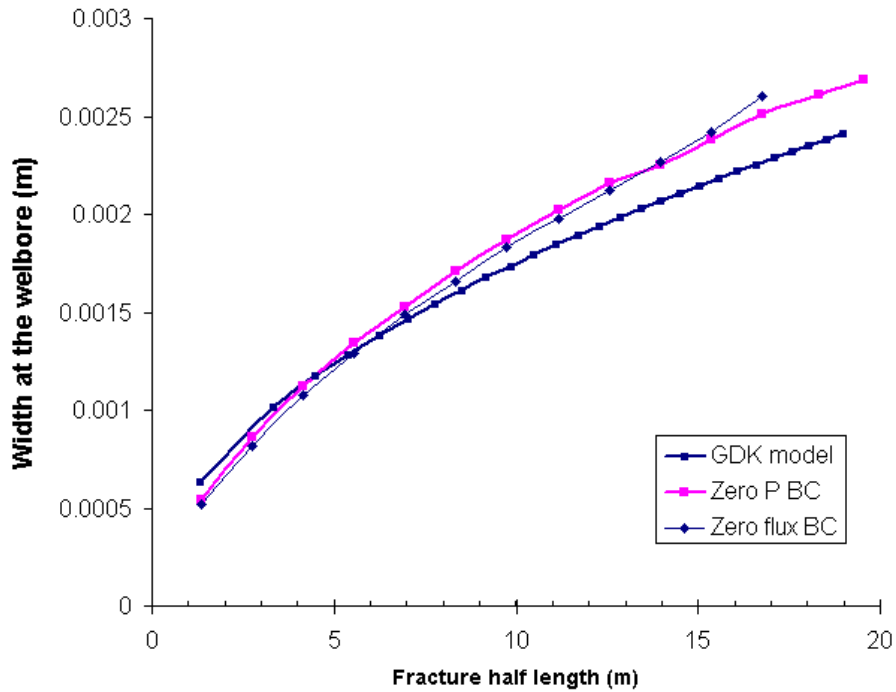
Figure 4.13: Fracture width distributions at the wellbore in three models.

Most of the fracturing fluids used in the oil industry fit better in the category of power-law fluids (Appendix B). Most fracturing fluids are characterized by power-law index n' between 0 and 1 (Cameron and Prud'homme 1989). This corresponds to the so-called shear thinning behavior, because at low Reynolds numbers, the stresses induced by shear thinning are large enough to move the particles away from the centerline and from the fracture walls. Hence, proppants can reach farther distances in the hydraulic fracture (Huang and Joseph, 2000). Accordingly, in the next example, a case of a power-law fluid is considered.

The formulation for power-law fluid is presented in appendix B. A power-law constitutive equation requires two parameters: the power-law index, n' and the

consistency index, K'. For the special case that $n' = 1.0$, equations B.1, B.2 and B.3 reduce to the corresponding equations for the Newtonian fluid. Here, a power-law fluid with 30lb cross-linked gel and $n' = 0.7$, $K' = 0.02 \, \text{lbf.sec}^{n'}/\text{ft}^2$ is considered. Other properties are shown in Table 4.2. The pressure profile in the fracture induced by this fluid is compared with a Newtonian fluid ($n' = 1.0$) in Figure 4.14a. It shows less net pressure at the wellbore for the shear thinning fluid, lower bottomhole pressure makes the fracturing job more feasible. The difference between pressure in two fluids decreases as one gets farther away from the wellbore.

Young's modulus (**E**)	4.0×10^6 psi
Shear modulus (**G**)	1.6×10^6 psi
Poisson's ratio (**v**)	0.25
Injection rate (**Q₀**)	10 bbl/min
Fracture Height (**H**)	100 ft

Table 4.2: Input data for the non-Newtonian fluid case.

Figure 4.14b shows fracture length versus injection time for different power-law indices. The tangent line at each point to this plot is the fracture propagation speed. At early stages, the fracture with shear thinning fluid propagates faster as expected. But for large enough time (after 260 sec here), the fracture driven by a power-law fluid with a given power-law index $n' = 1.0$ would propagate faster, compared to the case of a fluid with a lower power-law index. This counterintuitive result can be explained by the fact

141

that a fluid with lower power-law index is not necessarily less viscous than a fluid with higher power-law index. In general, if the rheological curves of two fluids with different n' and K intersect each other at a given reference value then the fluid with lower power-law index would actually have a higher apparent viscosity after the intersection point. Adachi and Detournay (2002) made a similar observation with their analytical solution.
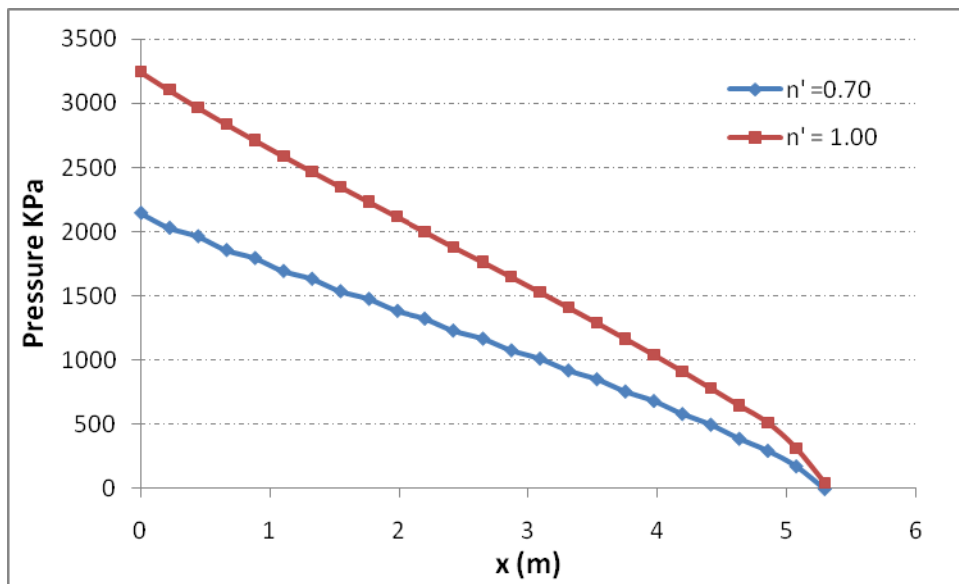
Figure 4.14a: The pressure profile in a wing of the hydraulic fracture.
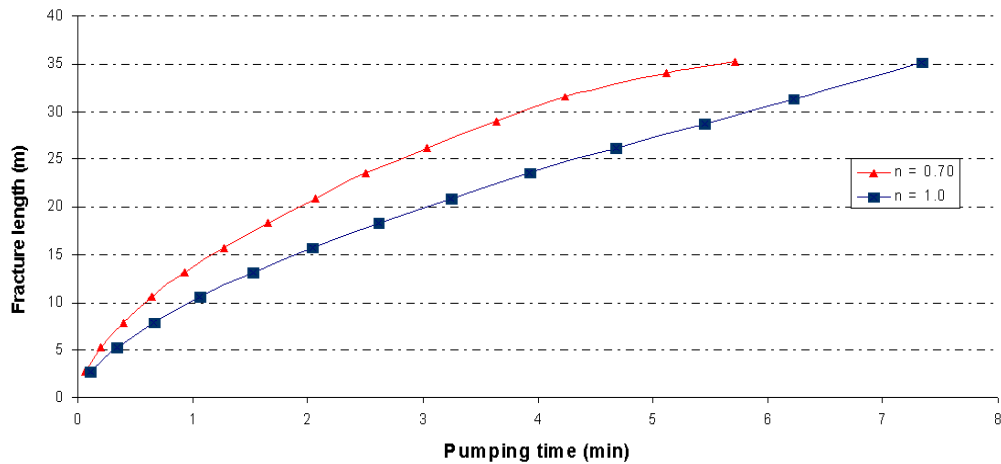
Figure 4.14b: Fracture length versus pumping time compared for different power-law index (Q = 2.00 bbl/min, the other specifications are simillar to Table 4.1).

4.6. Fracture Diversion

It has been demonstrated in Chapter 3 that the hydraulic fracturing of wells in naturally fractured reservoirs can differ significantly from hydraulic fracturing in conventional homogeneous isotropic reservoirs. In this section, the coupled-simulation technique developed earlier in this chapter is applied to study a situation where a hydraulic fracture intersects a natural fracture, and the fracture energy of the cement is low enough to divert the hydraulic fracture based on the maximum energy release rate criteria (see section 3.4).

The displacement of fracture surfaces in a kinked fracture are continuous functions. Therefore, the difference between displacements, which is the fracture opening in the global coordinate system, is also a continuous function. Because each side of any kinked point exists at two different local coordinate systems, the fracture width

143

distribution becomes discontinuous at each kink point. The fluid flow equations are usually solved using finite element, finite difference, or finite volume schemes. In methods such as finite difference method in where the problem is solved for nodal values, it is not possible to introduce fracture width discontinuity at the kink point. However, in finite element methods, the global stiffness matrix (equation 4.15) is constructed element by element. Therefore, it is possible to incorporate fracture width discontinuity into the model.

A simplified assumption can be made about the laminar flow at the kink points. This would not be an appropriate assumption for large Reynolds numbers. Up to this point, it has been assumed that flow in the fracture has a low Reynolds number. Based on this assumption, the lubrication equation could be utilized for modeling fluid flow inside the fracture. Therefore, the assumption for laminar flow at the kinked points does not add a new limitation to the analysis. By looking at the lubrication equation (equation 4.6), it can be seen that discontinuity of fracture width causes discontinuity of the fracture pressure gradient. It is notable that the pressure has a unique value at the kink point.

In the presence of natural fractures, the hydraulic fracture is not necessarily symmetric. Thus, the wellbore is not necessarily located in the middle of two fracture tips. Despite some models, such as those developed by Advani and Lee 1982, the model presented here can handle these cases without any issues. The only limitation is that the wellbore should be located on a node in order to obtain accurate results from the model.

Two cases are considered here: (1) a case where the hydraulic fracture forms a small-angle kink to follow the natural fracture path; and (2) the case for which the

hydraulic fracture forms a large-angle kink to follow the natural fracture path. In all the examples, the hydraulic fracture is growing in two wings, and the initial fracture length is 5.8m.

Table 4.3 contains the details of the input for Case 1. The fracture toughness of the cement is assumed to be as large as half of the toughness of the intact rock. A zero pressure boundary condition is assumed to exist at the tips. In situ stress is not considered for now. A lack of in situ stress is equivalent to the isotropic in situ stress field because the pressure is assumed to be the net pressure.

In the first example the natural fracture orientation (strike) is only 18 degrees away from the hydraulic fracture trend, and the wellbore is located at s = 0.0 (Figure 4.15). Figure 4.16 illustrates the pressure profile along a diverted hydraulic fracture. No noticeable change in pressure gradient exists after the intersection between the hydraulic fracture and the natural fracture, which is located at $s = 7.23 \text{ m}$. The small magnitude of the pressure gradient change is not surprising because of the small discontinuity in fracture width at the intersection point (Figure 4.17), which in turn is caused by the orientation changes of the hydraulic fracture. Due to the low angle of diversion, the fracture width has a small discontinuity. The issue of pressure gradient change after the intersection point requires further investigation to understand the possible effect of the intersection angle and in situ stress anisotropy.

Young's modulus (E)	3.5×10^6 psi
Poisson's ratio (v)	0.20
Injection rate (Q_0)	10 bbl/min
Fracturing fluid viscosity (μ)	100 cP
Fracture height	100 ft
Fracture toughness	1.50 MPa.m$^{1/2}$
Fracture cement toughness	0.75 MPa.m$^{1/2}$

Table 4.3: Input data for the fracture diversion simulation.

The pressure profile shows negative values in areas close to the tip of the short diverted fracture (Figure 4.16). The negative net pressure is characteristic behavior of the asymptotic solution near the fracture tip. In cases where the length of the dry zone is not considered explicitly in the model, negative net pressure appears near the fracture tip (Adachi and Detournay, 2008). However, the negative net pressure zone cannot be interpreted as a dry zone because the negative net pressure is not equivalent to negative absolute pressure. It only implies that a suction zone exists behind the hydraulic fracture tip. This phenomenon is expected because it is difficult for the fluid to penetrate into the newly induced section of the hydraulic fracture.
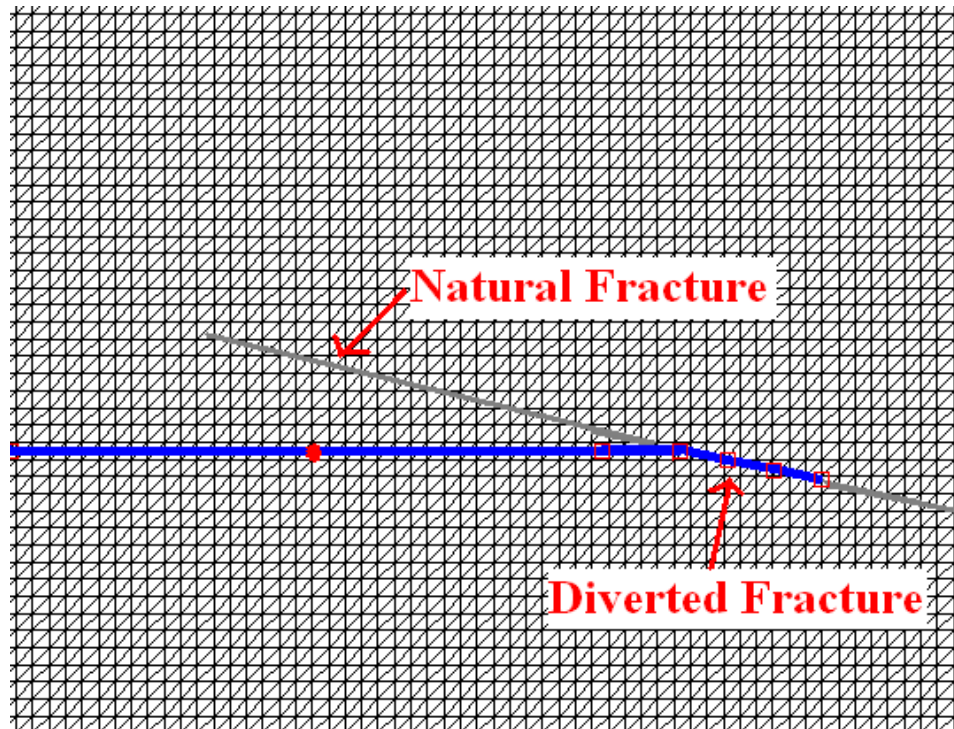
Figure 4.15: A schematic illustration of a low-angle fracture diversion (18 degrees). The cemented natural fracture is plotted in gray, and the hydraulic fracture is plotted in blue. The location of the wellbore is depicted by a red circle.
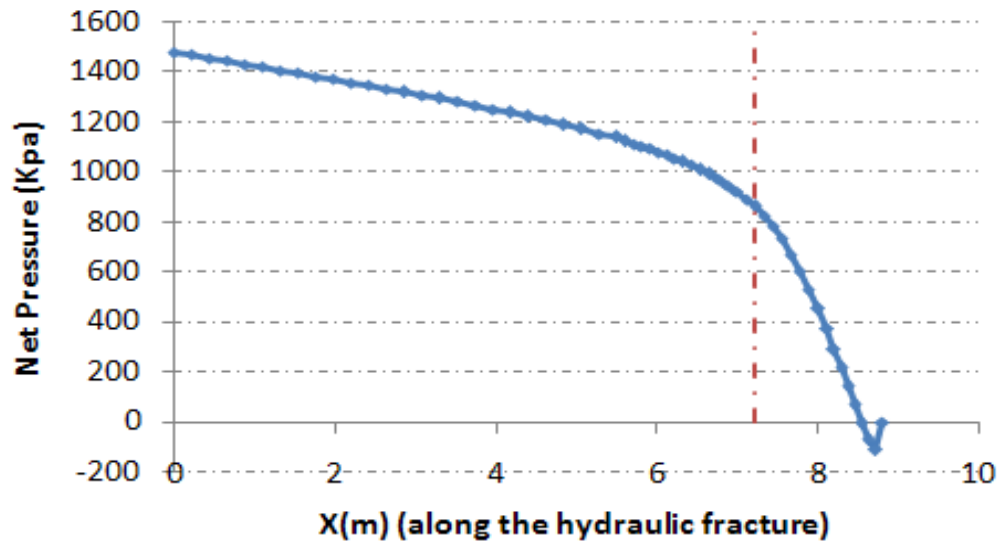
Figure 4.16: Pressure profile along a hydraulic fracture. The pressure gradient change due to the intersection point is not noticeable.
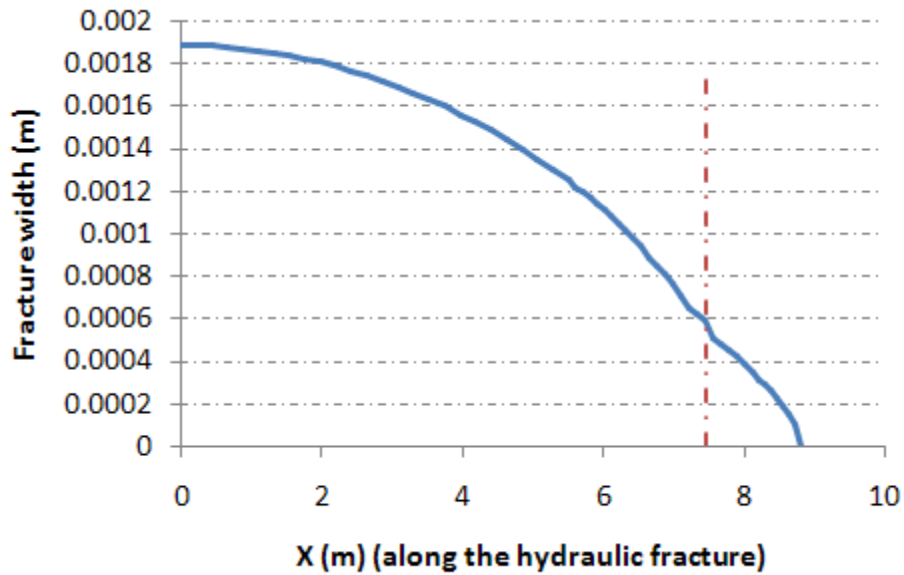
Figure 4.17: Shear and normal displacements of fracture faces with respect to each other.

In the second example, the hydraulic fracture approaches a natural fracture and makes a 60 degree angle with the natural fracture (Figure 4.18). This wellbore is located at $s = 0$. The hydraulic fracture tip diverts into the natural fracture at $s = 7.83\,\text{m}$. Fracture propagation in the new direction is slower than the other tip of the hydraulic fracture (Figure 4.18). It is remarkable that anisotropy of in situ stresses is not present to impede further fracture propagation at the intersection point. Therefore, it may be concluded that the hydraulic fracture decelerates in the natural fracture due to the abrupt change in its orientation. By pumping more fluid, fracture propagating from the other tip faster.

In the case of large kink-angle, the pressure builds up behind the fracture tip, and the pressure front becomes sharper to push fluid farther inside the diverted branch (Figure

148

4.19). When the fracture has not progressed enough inside the new fracture, the displacements of the induced fracture surface (the part located in the natural fracture) are more sliding rather than opening (Figure 4.20). This explains why the net pressure inside the branch near the fracture tip is zero or negative (see Figure 4.21). As the fracture propagates farther down inside the natural fracture, enough spacing is provided for fluid to flow, and the suction zone becomes smaller. A small abrupt change exists in the fracture width at the intersection point (Figure 4.20). Additionally, orientation changes causes some sliding, the magnitude of which is comparable to the fracture width magnitude. However, the induced sliding does not contribute to the fluid flow inside the fracture, but it can generate microseismic events.

Bottomhole pressure decreases as fracture propagates through the natural fracture (comparing Figure 4.22 with 4.21), but the pressure at the intersection point increases. Because the resistance against fracture growth increases as fracture propagates further. The change in pressure gradient enhances by further propagation. Additionally, fracture propagation increases the width at the intersection point (comparing Figure 4.23 with 4.20) but the magnitude of the fracture width drop at the intersection point increases as well. Therefore, the intersection point still works as a choke for fluid flow inside the fracture.

149
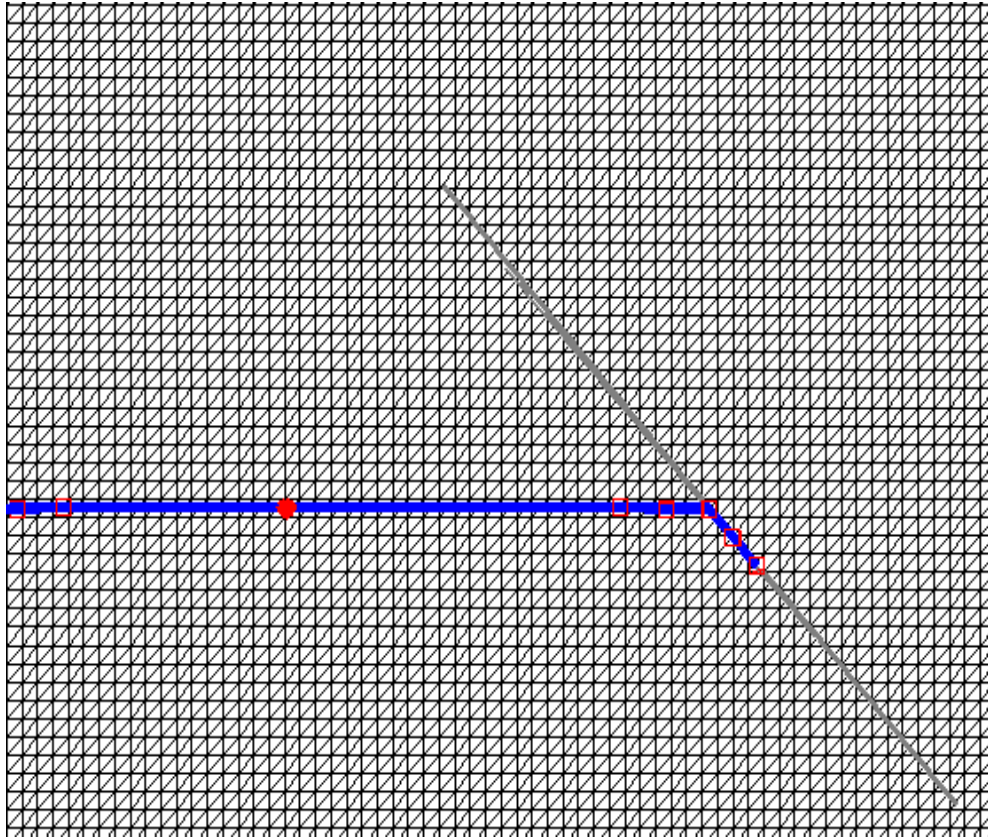
Figure 4.18: Geometry of a high angle fracture diversion. The left wing of the hydraulic fracture is not shown completely in this picture.

The bottomhole pressure during this fracture treatment is plotted in Figure 4.24. The fluctuation in net pressure gradient is associated with the direction changes in figure 4.18. The magnitude of the fluctuation in wellbore pressure is not large enough to be easily recognized at the weillbore. Therefore, pressure changes are probably not useful for diagnosing natural fracture intersections.

150
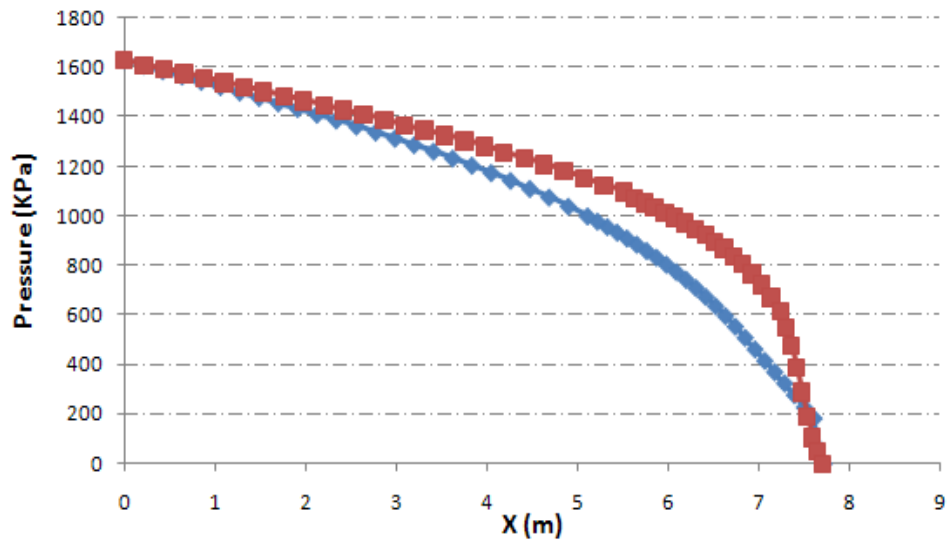
Figure 4.19: A comparison of the pressure profile of the fracture when the fracture tip has passed the intersection point (red line) to the pressure profile in the absence of natural fractures (blue line).
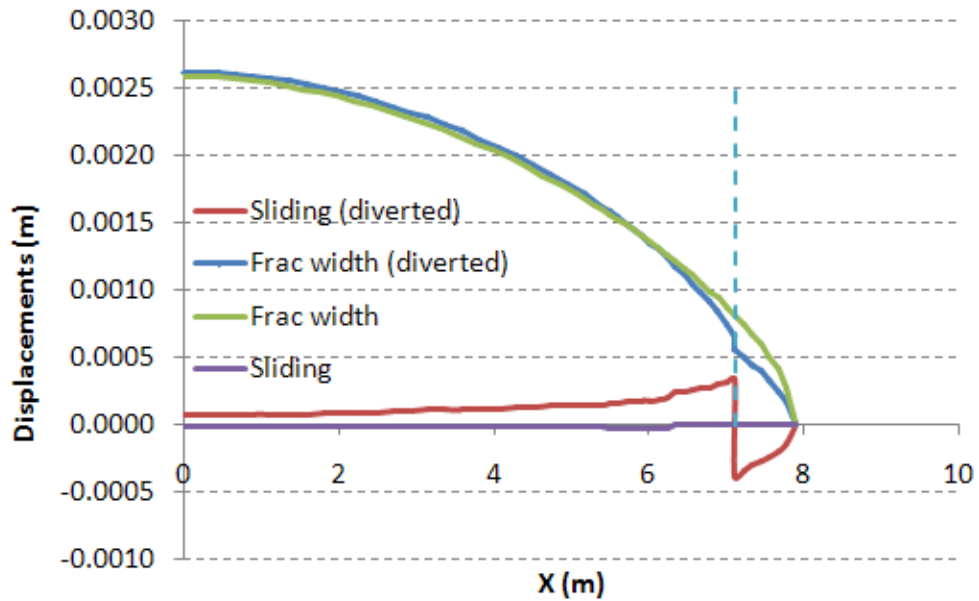
Figure 4.20: Fracture displacements in normal and tangential directions compared to a straight fracture and a diverted fracture. Abrupt changes in both components of displacement in the diverted case are noticeable.

151
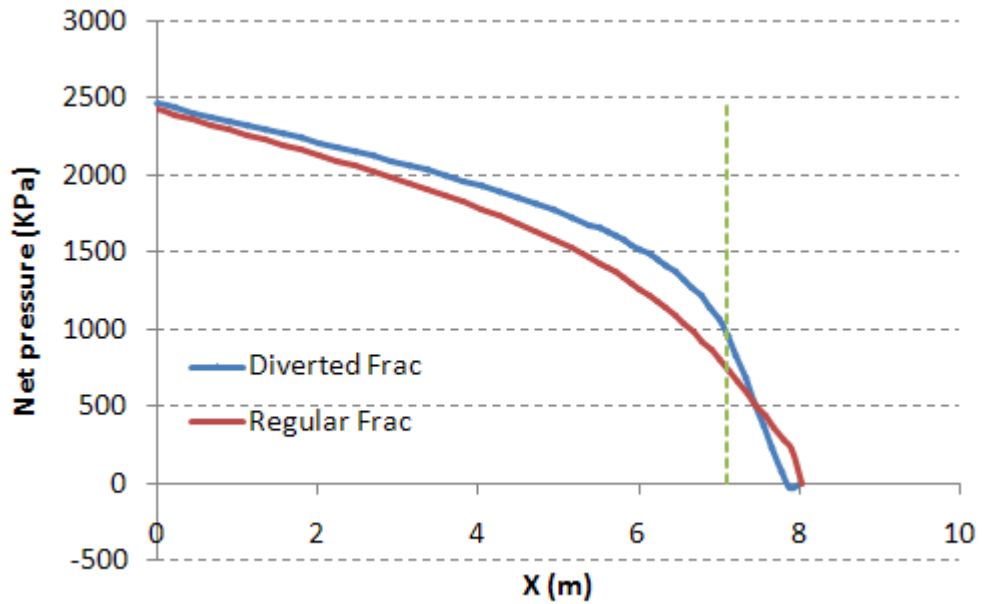
Figure 4.21: The net pressure profile of the fracture in the cemented natural fracture (blue line) compared to the pressure profile in the absence of natural fractures (red line).
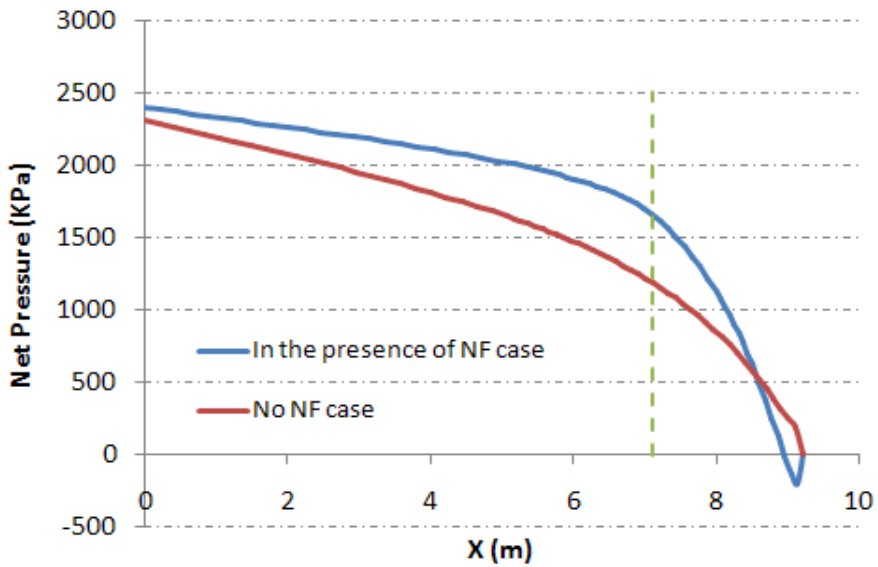
Figure 4.22: The net pressure profile inside the diverted hydraulic fracture compared with the straight hydraulic fracture.
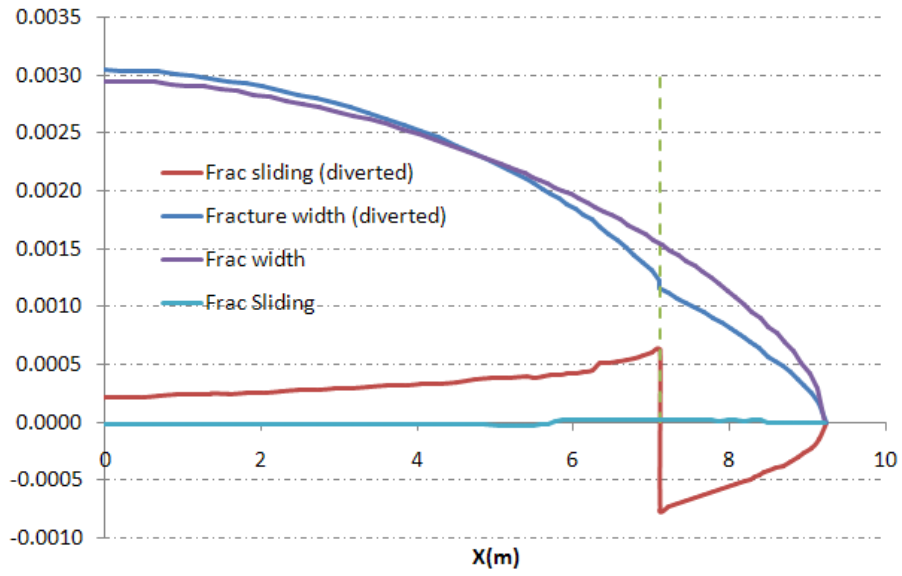
Figure 4.23: Opening and shearing displacements of the diverted hydraulic fracture compared with the straight hydraulic fracture.
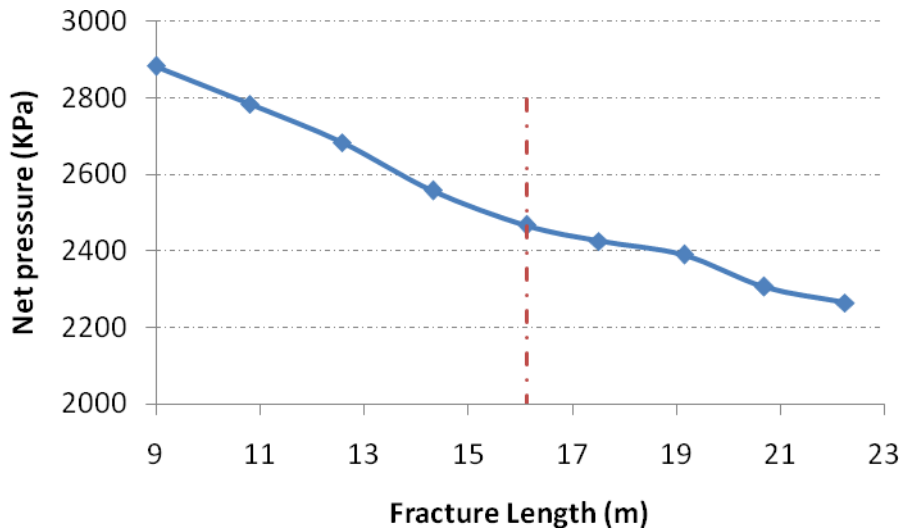
Figure 4.24: Bottomhole fracture pressure for the case of figure 4.18.

153

Figure 4.25 illustrates how mode I and II stress intensity factors change during the period that the hydraulic fracture diverts into the natural fracture. The mode II stress intensity factor increases and the mode I stress intensity factor drops as the fracture moves along the natural fracture (the path segment starts from s = 7.22 m, where s is the 1D coordinate system along the induced fracture). Because the critical energy release rate at the cemented path is lower, the change in stress intensity factors does not stop fracture from propagating. The mode II stress intensity factor is always much less than the mode I stress intensity factor and therefore cannot alter the fracture growth regime from mode I to pure mode II. It also shows that the mode I stress intensity factor increases as the hydraulic fracture propagates farther down in the cemented path.
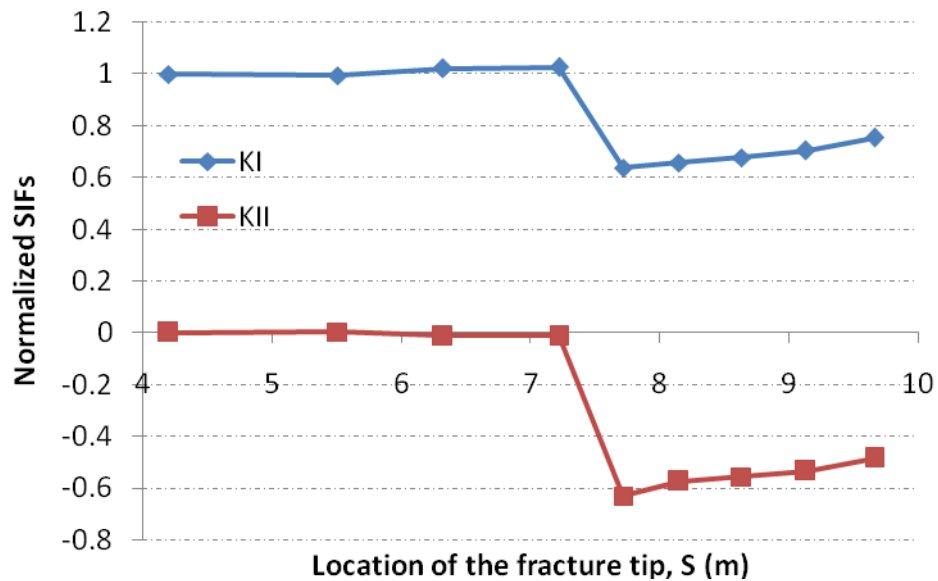
Figure 4.25: The changes of stress intensity factor during the growth of the hydraulic fracture through the natural fracture. SIFs were normalized K_I of a straight hydraulic fracture with similar conditions.

The contribution of the mode II stress intensity factor may insist for a period of time after the hydraulic fracture diverted into the natural fracture. Accordingly, the hydraulic fracture continues its propagation in mixed mode I and II. This is a combination of opening and sliding along the natural fracture rather than a pure opening of the natural fracture. At this point, the fracture width at the kink point increases, but the fracture opening inside the natural fracture is not large enough to facilitate fluid flow and subsequently to increase pressure. After the hydraulic fracture propagates for a period of time, the fracture gains a large enough opening in the natural fracture for fluid to flow; this is coincident with the smooth reduction of the mode II stress intensity factor and increase of mode one stress intensity factor at the growing tip of the hydraulic fracture.

In order to study the effect that in situ stress anisotropy has on the fracture diversion, the previous example was simulated for the case that principal horizontal stresses are not equal to each other. Table 4.4 contains input data related to this example. The hydraulic fracture intersects the natural fracture at $s = 7.18m$ (Origin of the coordinate system is located at the wellbore.) because the fracture does not have enough energy to further propogate in the new direction, the fracture tip freezes. It is remarkable that the stress anisotropy tries to impede further fracture propagation through the natural fracture. By pumping more fluid, the fracture continues propagating from the other tip (the other wing extends from $s = -7.18\,\mathrm{m}$ to $s = -11.34\,\mathrm{m}$). As the fracture propogates in the other tip, pressure will build up at the hydraulic fracture-natural fracture intersection. Consequently, the hydraulic fracture resumes its propagation in the natural fracture path. Figure 4.26 illustrates the pressure profile inside the hydraulic fracture as it

155

propagates through the sealed natural fracture. As the fracture propagates through the new path, the bottomhole pressure decreases slightly, but the pressure at the intersection point and inside the natural fracture increases.

Young's modulus (E)	4.0×10^6 psi
Shear modulus (G)	1.6×10^6 psi
Poisson's ratio (v)	0.25
Injection rate (Q_0)	10 bbl/min
Fracturing Fluid viscosity (μ)	500 cP
Fracture Height (H)	100 ft
Rock Fracture Toughness (K_{IC})	2.5 Mpa.m$^{1/2}$
Cement Toughness	0.30 K_{IC}
$S_{H,max} - S_{H,min}$	350 psi

Table 4.4: Input data for the fracture diversion simulation under anisotropic stress condition.
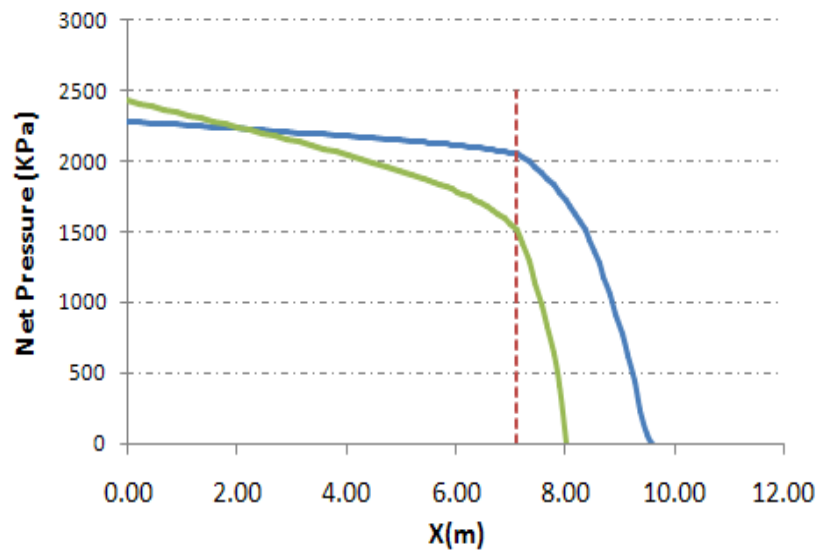
Figure 4.26: Pressure profile in diverted fracture as it grows through the natural fracture.

Despite isotropic stress state that no significant pressure gradient changes were observed in the diverted fracture (Figure 4.16), fracture gradient changes after intersection point is observable in this case (Figure 4.26). The pressure buildup or sharp pressure front in the diverted fracture is needed to overcome the unfavorable orientation of the natural fracture with respect to the principal in situ stresses.

The fracture width profile is shown in Figure 4.27. The change in fracture width at the intersection point is much more than the fracture width changes in the isotropic case (Figure 4.23). As fracture propagates farther into the natural fracture, fracture width changes at the intersection point increases. Therefore, it becomes harder for the fluid and proppants to flow into the natural fracture. This choke may cause early screenout at the hydraulic fracture-natural fracture intersection. The bottomhole pressure in this case (Figure 4.28) is about 400 KPa greater than the bottomhole pressure in the basic case with no natural fracture. The pressure difference due to the fracture diversion is not still high enough to be identified at the borehole.

Figure 4.29 compared fracture growth after diverting by the natural fracture with the growth of a straight hydraulic fracture. However, the other tip of the hydraulic fracture is not affected by the unfavorable direction of the natural fracture, the diverted hydraulic fracture grow slower than the straight non-diverted fracture. The reason behind this observation can be found in Figure 3.30, which shows large reduction in mode I stress intensity factor which provide energy to push fracture farther. It is noticeable that due to stress anisotropy, mode II has become the dominant mode after fracture diversion, which is in opposition with previous observation in isotropic reservoirs (Figure 4.25).
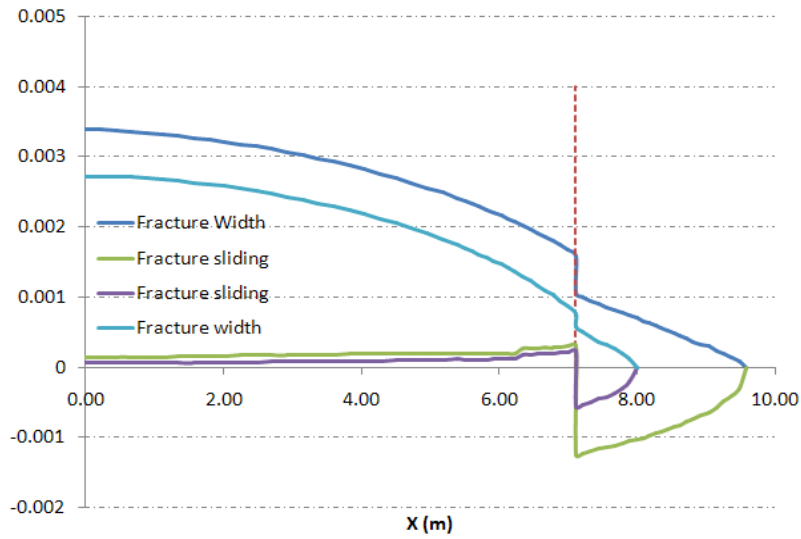
Figure 4.27: Fracture width profile in diverted fracture as it grows through the natural fracture.
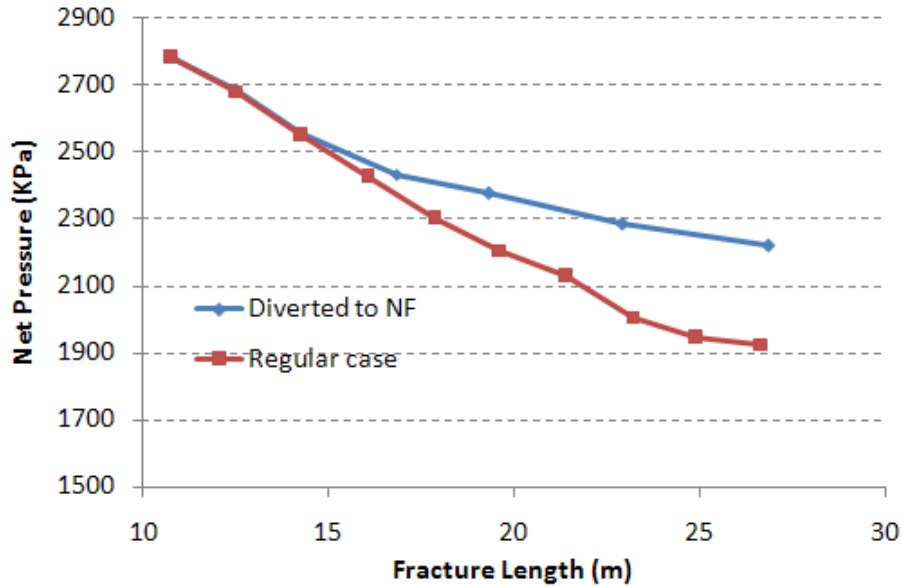
Figure 4.28: Bottomhole pressure in the presence of a high angle natural fracture and stress anisotropy compared to the case with no natural fractures.

158
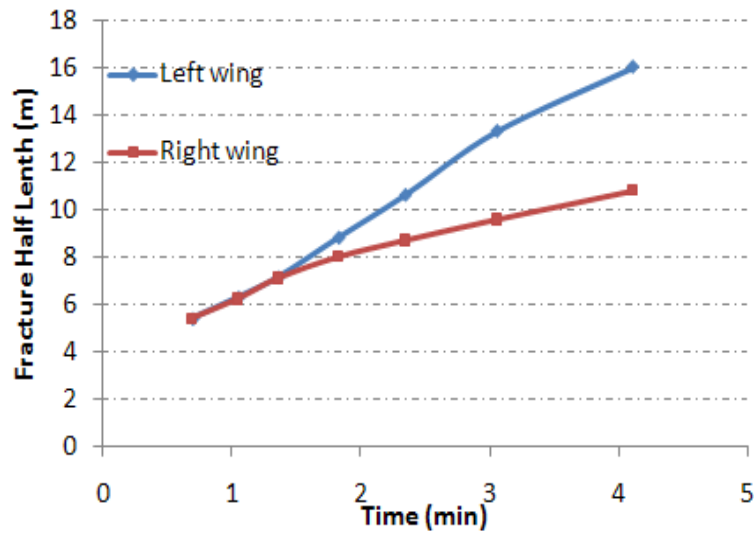
Figure 4.29: Growth of diverted fracture compared with the growth of the straight fracture.
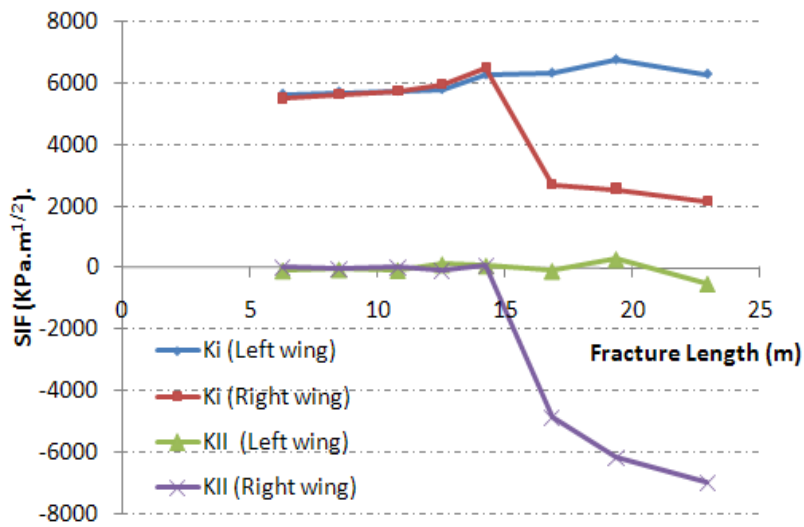
Figure 4.30: Stress intensity factor of diverted fracture compared with ones of the straight fracture.

The ability of the diverted hydraulic fracture to progress inside a natural fracture also depends on the distance from the wellbore to the intersection point. It is notable that the distance of the natural fracture to the wellbore is not a governing factor on fracture diversion or fracture crossover because stress intensity factor is almost constant at the tips of symmetric fractures. As shown in Figure 4.31 as a straight fracture propagates farther due to viscous dissipations, there is less pressure built up behind the fracture tip. Therefore, the growing fracture exerts less pressure on the part of the rock which is ahead of the hydraulic fracture. Therefore, in distances farther from the wellbore there is a smaller chance to re-open the cemented fractures.
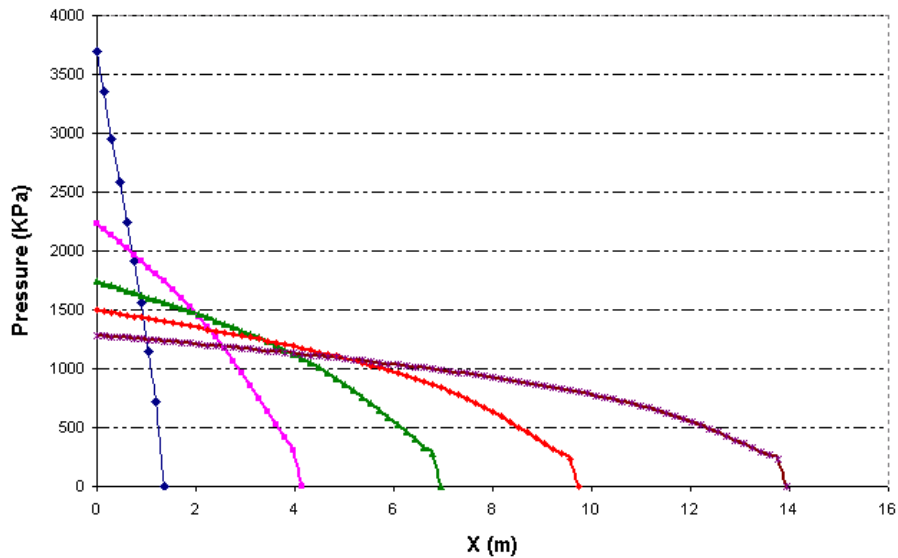
Figure 4.31: The pressure profile inside the hydraulic fracture at different injection times.

160

4.7. Conclusions

The coupled problem of fluid flow, fracture propagation and interaction with pre-existing fractures was solved numerically. The fluid flow part was solved using standard Galerkin finite element methods. A methodology is developed to couple the lubrication equation with the XFEM model to model the interaction between fluid flow inside the fracture with rock deformations. The XFEM model results show good agreement with KGD model for planar fractures. The effects of different boundary conditions at the fracture tip were also considered. It was found that zero net pressure at the tip and zero flux at tip do generate similar results for fluid flow far from the fracture tips.

Fracture diversions into the pre-existing natural fractures were also studied. The pressure gradient discontinuity at the intersection point of the hydraulic fracture with the natural fracture and its subsequent effects on the shape of pressure profile in the natural fracture has been discussed. The effects of the orientation of natural fractures, wellbore location and fracturing fluid viscosity and in situ stress anisotropy have been explored.

It was shown that the effect of stress anisotropy could magnify the effect of natural fractures on hydraulic fracturing propagation. In highly anisotropic cases, the diverted hydraulic fracture may arrest by the natural fracture. Additionally in these cases, fracture width reduction at the intersection point amplifies, so the likelihood of proppant bridging increases. Therefore, it may be predicted that hydraulic fracturing in isotropic fractured formations could be more successful in compare to fractured reservoir with high in situ stress anisotropy.

It is concluded that natural fractures may have a significant effect on hydraulic fracturing, specifically fracture pattern, length and width, and proppant transport. Non-planar geometry restricts fracture width, which increases fracture treating pressure near the intersection point. This phenomenon may cause screen-out during the proppant stages of a fracturing job. In the other hand, it was found that bottomhole pressure is not sensitive to fracture diversion. Therefore, it cannot be used for diagnosing fracture diversions. But the resultant reduction in fracture length can decrease expected well production enhancements and put at risk well economics. Therefore to predict fracture growth in natural fractures, spacing and orientation of natural fractures must be specified.

The optimum fracturing job would be the fracturing treatment that will cross and connect as much of the natural fracture system to the wellbore as possible. Based on what has been studied so far, this case may happen when the original direction of the hydraulic fracture is perpendicular to the orientation of natural fractures. In this situation, the hydraulic fracture open natural fractures or reactivate them, but it is less likely to divert into natural fracture, which reduces the fracture drainage radius. In case of diversion, it will resume its propagation in the original direction due to the unfavorable orientation of the natural fractures.

Chapter 5. Conclusions and Recommendations

5.1. Summary of the completed work

In this dissertation, the interactions between a growing hydraulic fracture and the surrounding natural fractures were studied. These interactions range from the intersection of natural fractures to the far-field reactivation of them. Three possibilities that might occur during the hydraulic fracturing of naturally fractured reservoirs were considered. First, the natural fractures may have no influence and the hydraulic fracture will propagate in a direction parallel to the maximum horizontal stress as expected in non-fractured reservoirs. This may be a result of high cement strength in the natural fractures (comparable to matrix strength), unfavorable natural fracture orientation, or a fracturing pressure that is not high enough to overcome the normal stress perpendicular to the natural fracture. In the second scenario, the hydraulic fracture intersects the natural fracture, and the hydraulic fracture is arrested. The fluid is completely diverted into the natural fracture system. The natural fractures will open if the energy of the growing hydraulic fracture is large enough to reopen fracture cements or if the shear stresses are large enough to overcome the friction between fracture surfaces. An energy criterion was proposed to predict fracture diversion based on fracture energy of cements, fracture

energy of rock and the orientation of natural fractures. This criterion includes interaction with both cemented and uncemented fractures. In the third scenario, debonding may take place ahead of the primary crack prior to the fractures' intersection. The growing fracture exerts large tensile and shear stresses ahead of and near the tip. These stresses can be large enough to debond or shear the sealed natural fractures. So in the first and second types of events, the hydraulic fracture propagates all the way into the natural fracture before the interaction occurs. In the third case, the natural fracture starts to open/shear or propagate before the hydraulic fracture arrives because of near-tip stress concentrations.

To be able to study more complex situations, an extended finite element (XFEM) code was developed. Fractures are allowed to propagate independently of the mesh configuration by permitting the fracture to cross the elements. Additionally, the symmetry and sparsity of the stiffness matrix is preserved. A new junction function was introduced to handle fracture intersections, and a new model for fracture propagation (based on energy release rate) was incorporated into the XFEM model. To improve the accuracy of partially enriched elements, a larger radius for crack tip enrichment was considered in the model. The CIM and CFM superconvergent methods are used for stress intensity factor calculations. It is the first time that these methods were applied in the XFEM framework. It was found that these methods give more accurate results in comparison to other common techniques in the literature.

The XFEM model provides an opportunity to consider more complicated configurations for fracture interaction. For instance, it was shown that under certain circumstances, the presence of debonded fractures surrounding the hydraulic fracture tip

may accelerate or decelerate growing fractures. In chapter three, different scenarios in reactivation of natural fractures were studied by using the developed XFEM model and governing factors in all of these scenarios were discussed.

In Chapter 4, the models developed in previous chapters were coupled with fluid flow in the hydraulic fracture. This coupling provided insight on pressure changes due to the interaction of a hydraulic fracture with natural fractures. The new model results show good agreement with KGD model for planar fractures. The effects of different boundary conditions at the fracture tip were also studied. It was found that zero net pressure at the tip and zero flux at tip generate similar results for fluid flow far from the fracture tips.

The pressure gradient discontinuity at the intersection point of the hydraulic fracture with the natural fracture and its subsequent effects on the shape of pressure profiles shows the greater amount of effort needed for fracture propagation through the natural fracture. The effects of the orientation of natural fractures, wellbore location and fracturing fluid viscosity and in situ stress anisotropy indicate their significant role in fracture propagation in the new direction. It was shown that the effect of stress anisotropy could magnify the effect of natural fractures on hydraulic fracturing propagation.

The findings in this research can be used to explain different observed behaviors of hydraulic fracturing in tight gas reservoirs. It gives the ability to predict the possible reactivations of natural fractures and the potential scenario of the reactivation process. Generally, these techniques can be utilized to modify pressure decline analysis and associated design and diagnostic techniques; for instance one method is proposed by Nolte (1988).

5.2 Possible lines for future research

The current model cannot incorporate the height effect into the equations. Therefore, it only represents KGD geometry, which is limited to short and tall fractures. The next step to complete this problem is to add the height constraint that is equivalent to PKN geometry shown in Chapter 1. In addition to that the model presented here is unable to incorporate multiple layers in the system. Since in most cases, fracturing treatments are done in multi-layered systems, a more realistic model needs to incorporate this aspect of the problem. To achieve this goal, one of the main possible lines for future research is to extend the current model to three dimensions. The three dimensional analysis can be done using brick elements to construct the finite element model. The height in the pseudo-3D models is a function of position along the fracture as well as time. The main assumption is that the fracture length is much greater than the height, and an important difference between the pseudo-3D and the 2D models is the addition of a vertical fluid flow component. A shear lag approximation is one of the techniques used in the literature to implement pseudo 3D geometry (Huang et al. 2004). The pseudo-3D models have been used to model fractures that cross multiple rock layers with differing stresses and properties. These models are simpler and faster than fully 3D models and are limited to vertical fractures.

In hydraulic fracturing jobs, the fracture is first initiated with a clean fluid and then followed with a slurry containing proppant. The proppant is introduced into the fracture for maintaining the fracture opening after the fracturing operation, and to ensure a good conductivity of the induced fracture. The results shown in previous chapters

166

demonstrate that when the induced fracture pattern is complex, there are some restrictions on fracture width at the intersection points that could have a considerable impact on the proppant transport. Consequently the resultant proppant bridging could affect the fracture network conductivity and well performance.

To address this issue, the proppant transport equations can be coupled to the current system of equations in a loose manner at the end of each time step. Using the calculated pressure distribution, it is possible to determine the velocity of proppants, v_p, and using that value to get the proppant concentration distribution c by solving the following equation,

$$\frac{\partial(cw)}{\partial t} + \nabla.\left(cwv_p\right) = 0 \,, \tag{5.1}$$

which describes the time dependent distribution of the concentration of proppant in the fracture. The proppant concentration calculated by equation (5.1) is used to adjust fluid density, ρ, and fluid viscosity in the lubrication equation (equation 4.6). It is notable that in the case of varying density the term $\partial P/\partial s$ is replaced by ($\partial P/\partial s - \rho g$). The volume of proppant, calculated using proppant concentration, is a design parameter that may affect treatment time and injection rate. Therefore, it is necessary to incorporate the proppant transport for practical purposes.

Despite the limitations noted, the model presented in this dissertation could successfully investigate characteristic behavior of fracture intersections and potential reactivation mechanisms of natural fractures. The developed model provides a framework for further development to address limitations such as height effect.

Appendix A: Validity of The Lubrication Equation

Since the width of the hydraulic fracture is much less than the other dimensions of the hydraulic fracture, the fluid motion inside the fracture can be assumed to be similar to fluid flow inside a narrow channel. In the model presented, the lubrication equation (equation 4.6) is used, this equation is derived for fluid flow inside two straight parallel plates. Field observations and outcrops show that fractures are not always planar. They may have non-planar geometry due the orientation of the tectonic stresses, heterogeneities such as joints or stress fields induced by local structures such as faults. Here, the authenticity of laminar Poiseuille flow for fluid inside the fractures is verified and its limitations are determined.

Following Wang (1980), the position vector for the center line of the fracture is give by

$$\vec{R} = X(s)\hat{i} + Y(s)\hat{j} .$$ (A.1)

The channel is defined by two surfaces at the distance *w/2* from the center line. The unit tangent vector $\hat{t}$ to the fracture center line is

$$\hat{t} = \frac{dx}{ds}\hat{i} + \frac{dy}{ds}\hat{j} .$$ (A.2)

From the Frenet formula,

$$\frac{d\hat{t}}{ds} = \kappa\hat{n}, \ \frac{d\hat{n}}{ds} = -\kappa\hat{t} ,$$ (A.3)

where $\kappa(s)$ is the curvature and $\hat{n}$ is a unit normal vector. The position of an arbitrary point inside the channel can be expressed by

$$\vec{x} = \vec{R}(s) + \eta \hat{n}(s), \tag{A.4}$$

where η is the distance from the center line, $-w/2 < \eta < w/2$.

The continuity equation for this coordinate system is

$$\frac{\partial u}{\partial s} + \frac{\partial}{\partial \eta}\left[(1-\kappa\eta)v\right] = 0, \tag{A.5}$$

where u and v are the velocity components in the s and η directions. By neglecting inertial forces, the Navier-Stokes equation (see, e.g., Batchelor, 1970) takes the form

$$\frac{1}{1-\kappa\eta}\frac{\partial p}{\partial s} = -\mu\frac{\partial}{\partial \eta}\left\{\frac{1}{1-\kappa\eta}\left[\frac{\partial v}{\partial s} - \frac{\partial}{\partial \eta}\left((1-\kappa\eta)u\right)\right]\right\}, \text{ and} \tag{A.6}$$

$$\frac{\partial p}{\partial \eta} = \frac{\mu}{1-\kappa\eta}\frac{\partial}{\partial s}\left\{\frac{1}{1-\kappa\eta}\left[\frac{\partial v}{\partial s} - \frac{\partial}{\partial \eta}\left((1-\kappa\eta)u\right)\right]\right\}, \tag{A.7}$$

where μ is the viscosity of the fluid and p is the net fluid pressure.

The solution for the equations (A.6) and (A.7) for constant curvature and linear pressure variation results along the fracture (channel) results in the following velocity distribution for the fluid

$$v(s,\eta) = 0, \tag{A.8}$$

$$u(s,\eta) = -\frac{1}{2\kappa^2}\frac{1}{\mu}\frac{\partial p}{\partial s}\left\{\frac{\left[\left(1-\left(\frac{\kappa w}{2}\right)^2\right)\right]^2}{2\kappa w}\ln\left(\frac{1-\frac{\kappa w}{2}}{1+\frac{\kappa w}{2}}\right)\frac{1}{1-\kappa\eta}-\right.$$

$$\left.\frac{1}{2\kappa w}\left[\left(1-\frac{\kappa w}{2}\right)^2\ln\left(1-\frac{\kappa w}{2}\right)-\left(1+\frac{\kappa w}{2}\right)^2\ln\left(1+\frac{\kappa w}{2}\right)\right](1-\kappa\eta)-(1-\kappa\eta)\ln(1-\kappa\eta)\right\}$$

.

(A.9)

The velocity distribution derived from the above equation can be plotted for different curvatures. The velocity is no longer parabolic for large curvatures. The flow rate along the fracture can be calculated by integrating the tangential velocity over the fracture width

$$Q = \frac{1}{4\kappa^4 w}\frac{1}{\mu}\frac{\partial p}{\partial s}\left\{\left(1-\left(\frac{\kappa w}{2}\right)^2\right)^2\left(\ln\left(\frac{1-\frac{\kappa w}{2}}{1+\frac{\kappa w}{2}}\right)\right)^2-\kappa^2 w^2\right\}.$$
(A.10)

In cases that κw is much less than one, the above equation reduces to the Poiseuille's equation

$$Q = -\frac{w^3}{12\mu}\frac{\partial p}{\partial s}.$$
(A.11)

This analysis cannot be extended for fluid flow at sharp corners such as kink points. But it guaranties the validity of lubrication equation for the curved path fractures.

Appendix B: Power-law Fluids Formulations

In this appendix, a formulation for non-Newtonian fluid flow in fractures is developed. Typical fracturing fluids fall in the category of power-law fluids (Ben-Naceur, 1989), in which

$$\tau = K' \dot{\gamma}^{n'}, \tag{B.1}$$

where τ is the shear stress, n' is the power-law index, $\dot{\gamma}$ is shear rate, and K' is the consistency index.

The pressure gradient for power-law fluids is

$$\frac{\partial P}{\partial s} = -\frac{2K'Q^{n'}}{w^{2n'+1}} \left(\frac{4n'+2}{n'} \right)^{n'}. \tag{B.2}$$

When $n'=1$, the fluid reduces to the Newtonian fluid (equation 4.4) with $K' = \mu$, the viscosity of the fluid. By rearranging the above equation, there will be

$$Q = \left(\frac{1}{2K'} \right)^{\frac{1}{n'}} w^{\frac{2n'+1}{n'}} \left(\frac{n'}{4n'+2} \right) \left(-\frac{\partial p}{\partial s} \right)^{\frac{1}{n'}}. \tag{B.3}$$

By substituting the above equation into the mass conservation equation (4.5), the governing equation for fluid flow inside the fracture will be obtained as

$$\frac{\partial}{\partial s} \left[\frac{n'}{4n'+2} \left(\frac{1}{2K'} \right)^{\frac{1}{n'}} w^{\frac{2n'+1}{n'}} \left(-\frac{\partial p}{\partial s} \right)^{\frac{1}{n'}} \right] = \frac{\partial w}{\partial t} + q_L. \tag{B.4}$$

One of the boundary condition of the above equation is constant flux rate at the wellbore,

$$Q|_{s=0} = \left(\frac{1}{2K'}\right)^{\frac{1}{n'}} w^{\frac{2n'+1}{n'}} \left(\frac{n'}{4n'+2}\right) \left(\frac{\partial p}{\partial s}\right)^{\frac{1}{n'}} \Bigg|_{s=0} = q_0 .$$ (B.5)

In a manner similar to Newtonian fluids, the standard Galerkin finite element method is used to solve the fluid flow equation. The fluid pressure is approximated by

$$p(s) = \sum_{i-1}^{\hat{N}} \varphi_i(s) p_i .$$

Where $\varphi_i(s)$ is the shape function for node i, P_i is the corresponding nodal value for the node i. The variational (weak) form of the equation (4.6) becomes

$$\int_L \frac{\Delta w}{\Delta t} \varphi_i(s) ds + \int_L q_L(t) \varphi_i(s) ds = \frac{1}{12\mu} \int_0^L \frac{\partial}{\partial s} \left[\frac{n'}{4n'+2} \left(\frac{1}{2K'}\right)^{\frac{1}{n'}} w^{\frac{2n'+1}{n'}} \left(-\frac{\partial p}{\partial s}\right)^{\frac{1}{n'}} \right] \varphi_i(s) ds .$$ (B.6)

After integration by parts, there will be

$$C_{ij} P_j = f_i ,$$ (B.7)

where

$$C_{ij} = \sum_{j=1}^{\bar{N}} \int_0^L \frac{n'}{4n'+2} \left(\frac{1}{2K'}\right)^{\frac{1}{n'}} w^{\frac{2n'+1}{n'}} \left(-\frac{\partial p}{\partial s}\right)^{\frac{1}{n'}-1} \frac{\partial \varphi_i}{\partial s} \frac{\partial \varphi_j}{\partial s} ds ,$$ (B.8)

and

$$f_i = \int_L \frac{\Delta w}{\Delta t} \varphi_i(s) ds + \int_L q_L(t) \varphi_i(s) ds ,$$ (B.9)

where the matrix C is also dependent on P as it affects w. Using the current values of P and w to evaluate C, the above equation can be solved for a new pressure P.

To simplify fluid flow calculations, net pressure rather than absolute pressure is always used here. In some rare cases, net pressure in non-planar fractures, due to anisotropic in situ stress state, may peak in a location different from wellbore. This may make the term $(-\partial P / \partial s)^{1/n'}$ in equation (B.8) imaginary. To avoid this issue, absolute pressure instead of net pressure can be used in calculations. Since, absolute pressure is always decreasing away from the wellbore, the term $-\partial P / \partial s$ will be always positive. In addition, the absolute pressure at the fracture tips will be set to be equal to the far field in situ stress to satisfy zero net pressure at the fracture tips.

Appendix C: Execution Time

The code for coupling fluid flow with XFEM is built in MATLAB. Since it is not compiled in a high-performance programming language such as FORTRAN, it is hard to judge the speed and robustness of the algorithms through the MATLAB code execution times. The code is implemented in a dual processor (GenuineIntel x86 Family 6 Model 15 Stepping 6 ~2394 Mhz) machine with 2GB memory. The acceptable convergence error for pressure was considered to be less than 0.5% in these calculations.

	No. of Elements	D.O.F	CPU Time
1 st Step	39000	157050	136.58
20th Step	39000	157701	3285.14

Table C.1: CPU time required for coupled simulation of KGD problem.

Nomenclature

b Body forces

B Strain displacement matrix

c Proppant concentration

C Fluid flow stiffness matrix

D Elasticity matrix

E Young's modulus of elasticity

E' Plane-strain modulus of elasticity

F^l F-enrichment terms

G Shear modulus

$\overline{G}$ Energy release rate

G_c^{frac} Cement fracture energy

G_c^{rock} Rock fracture energy

H Heaviside step function

h Fracture height

I Magnitude of interaction integral

J Magnitude of J-integral

$\overline{J}$ Enrichment function for open fracture intersections

K Stiffness matrix

K_I Mode I stress intensity factor

K_{II} Mode I stress intensity factor

175

K_{Ic} Fracture toughness

K' Consistency index

L Fracture length

n' Power-law index

n_{enr} Number of types of enrichments

N Number of elements

N_i Shape function at node i

$\widetilde{N}_i$ Shape function for enrichment at node i

N_{TIP} Set of nodes of all elements containing the crack tip

N_{cr} Set of nodes of all elements containing cracks but not crack tips.

P Fluid Pressure

Q Flux rate

Q_0 Injection rate

q_i J-integral weight function at node i

r Radial distance from the crack tip

r_f Radius of crack tip enrichment

S_h Minimum horizontal stress

S_H Maximum horizontal stress

t Time

T   Traction vector

u Displacements

u^C Continuous displacement field

u^D Discontinuous displacement field

V^{-I} Extraction function for mode I

V^{-II} Extraction function for mode I

v_p Velocity of proppants

w   Fracture width

W   Elastic energy

Z   Westergaard's stress function

Greek Symbols

Γ_{cr} Fracture surface

Γ_u Boundary with prescribed displacements

Γ_t Boundary with prescribed tractions

$\dot{\gamma}$ Shear rate

δ Kronecker delta function

ε Strain

κ Curvature

λ Order of singularity at the kink points

μ Fluid viscosity

ν Poisson's ratio

ρ Density

σ Stress

τ Shear stress

φ Shape function

Φ Cut-off function

Ψ Enrichment functions

Ω Elastic domain

References

Adachi, J.I. and E. Detournay, 2002, Self-similar solution of a plane-strain fracture driven by a power-law fluid, *International Journal for Numerical and Analytical Methods in Geomechanics* , Vol. 26, pp. 579-604.

Adachi, J., Siebrits, E., Peircec, A., and J. Desroches, 2007, Computer simulation of hydraulic fractures, *International Journal of Rock Mechanics & Mining Sciences* 44, pages: 739–757.

Adachi, J.I. and E. Detournay, 2007, Plane-strain propagation of a fluid-driven fracture: finite toughness self-similar solution, International Journal of Fracture, to be submitted.

Adachi, J.I. and E. Detournay, 2008, Plane strain propagation of a hydraulic fracture in a permeable rock, Engineering Fracture Mechanics 75 (2008) 4666–4694.

Advani, S.H., Lee, J.K., 1982, Finite element simulations associated with hydraulic fracturing, *SPE* 8941.

Advani, S.H., Lee, T.S. and J.K. Lee, 1990, Three-dimensional modeling of hydraulic fractures in layered media: part I—finite element formulations, *Journal of Energy Resources Technology* 112:1–9.

Advani, S., Lee, T., Dean, R., Park, C. and J. Avasthi, 1997, Consequences of fluid lag in three-dimensional hydraulic fractures, *International Journal for Numerical and Analytical Methods in Geomechanics*, 21, pages: 229–240.

Akulich, A.V. and A.V. Zvyagin, 2008, Interaction between hydraulic and natural fractures, Fluid Dynamics, Vol. 43, No. 3, pp. 428-435.

Aguilera, R, 2008, Role of natural fractures and slot porosity on Tight Gas Sands, *SPE* 114174.

Ali, W., Gale, J.F.W., Ruppel, S.C., and R.G. Loucks, 2008, Lithofacies, depositional environment and burial history of the Barnett Shale in the Delaware Basin, Pecos Co., West Texas, and comparison with the Barnett Shale in the Fort Worth Basin (abs.), *in* West Texas Geological Society Fall 2008 Symposium, WTGS digital publication #08-120, p. 48.

Aliabadi, M. H. and C. A. Brebbia, 1993, Advanced Formulations in Boundary Element Methods, Elsevier Applied Science.

Anderson, G.D., 1981, Effects of friction on hydraulic fracture growth near unbounded interfaces in rocks, *SPE Journal*, Feb. 1981, pages 21-29.

Andrson, T.L., 1994, Fracture Mechanics: Fundamentals and Applications, second edition, CRC.

Asferg, J.L., Poulsen, P.N. and Nielsen, L.O., 2007, A consistent partly cracked XFEM element for cohesive crack growth, *International Journal for Numerical Methods in Engineering*, Volume 72, Issue 4, Pages 464 - 485.

Atkinson, B. K., 1989, Fracture Mechanics of Rock, 1st edition, Academic Press.

Babuška, I., Miller, A., 1984, The post-processing approach in the finite element method. III- A posteriori error estimates and adaptive mesh selection, *International Journal for Numerical Methods in Engineering*, Vol. 20, page 2311.

Babuska, I., Melenk, JM., 1997, The partition of unity methods, *International Journal for Numerical Methods in Engineering*, Volume 40, Pages 727-758.

Barenblatt, G.I., 1956, On certain problems of elasticity arising in hydraulic fracture studies, *Prikl. Mat. Mekh.* 20(4), pages: 475–486.

Barenblatt, G.I., 1962. The mathematical theory of equilibrium crack in brittle fracture, *Advances in Applied Mechanics*, 7, 55.

Barree, R.D. and H. Mukherjee, 1996, Determination of pressure dependent leakoff and its effect on fracture geometry, *SPE* 36424.
Batchelor, G.K., 1967, *An introduction to fluid dynamics,* Cambridge University Press, Cambridge, UK.

Belytschko, T. and T. Black, 1999, Elastic crack growth in finite elements with minimal remeshing, *International Journal for Numerical Methods in Engineerin*g, Volume 45, Pages 601-620.

Ben-Naceur, K., 1989, Reservoir stimulation, Edited by Economides, M.J. and Nolte, K.G., Prentice Hall, Englewood Cliffs, New Jersey.

Berumen, S., Tiab, D. and F. Rodriguez, 2000, Constant rate solutions for a fractured well with an asymmetric fracture, *Journal of Petroleum Science and Engineering*, 25, pages: 49-58.

Beugelsdijk, L.J.L., de Pater, C.J. and K. Sato, 2000, Experimental Hydraulic Fracture Propagation in a Multi-Fractured Medium, SPE 59419, *Proceedings of SPE Asia Pacific Conference on Integrated Modeling for Asset Management*, Yokohama.

Blanton, T.L., 1982, An experimental study of interaction between hydraulically induced and pre-existing fractures. SPE 10847, presented at the SPE/DOE unconventional gas recovery symposium, Pittsburgh, 16–18 May 1982.

Blanton, T.L., 1986, Propagation of hydraulically and dynamically induced fractures in naturally fractured reservoirs, SPE 15261, presented at the SPE/DOE unconventional gas technology symposium, Louisville, 18–21 May 1986.

Board, M., Rorke, T., Williams, G. and N. Gay, 1992, Fluid injection for rock burst control in deep mining. In: Tillerson JR, Wawersik WR, editors. In: Proceedings of the 33rd U.S. symposium on rock mechanics. Rotterdam: Balkema, pages: 111–20.

Bouchard P.O., Bay F, Chastel Y, Tovena I., 2000, Crack propagation modelling using an advanced remeshing technique, *Computer Methods in Applied Mechanics and Engineering,* 189, pages 723–742.

Bouchard, P.O., Bay, F., Chastel, Y., 2003, Numerical modeling of crack propagation: automatic remeshing and comparison of different criteria, *Computer Methods in Applied Mechanics and Engineering*; 192: 3887-3908.

Budyn, E., Zi, G., Moës, N., Belytschko T., 2004, A method for multiple crack growth in brittle materials without remeshing, *International Journal for Numerical Methods in Engineering*, Vol. 61, pages 1741-1770.

Bunger, A., 2005, Near-surface hydraulic fracture, PhD thesis, University of Minnesota, Minneapolis.

Branagan, P.T., Cipolla, C.L., Lee, S.J., Yan, L., 1987, Case History of Hydraulic Fracture Performance in the Naturally Fractured Paludal Zone: The Transitory Effects of Damage, SPE 16397-MS.

Britt, L.K. and C.J. Hager, 1994, Hydraulic fracturing in a naturally fractured reservoir, SPE 28717, presented at the SPE international petroleum conference and exhibition, Veracruz, Mexico, 10–13 October 1994.

Buchsteiner, H., Warpinski, N.R. and Economides, M.J., 1993, Stress-induced permeability reduction in fissured reservoirs, *SPE* 26513.

Cameron, J.R. and Prud'homme, R.K., 1989, Fracturing-fluid flow behavior, In Recent advances in Hydraulic fracturing, Gidley, J.L., Holditch, S.A., Nierode, D.E., Society of Petroleum Engineers: Richardson, pp 177-209.

Carbonell, R., 1996, Self-similar solution of a fluid-driven fracture, PhD thesis, University of Minnesota, Minneapolis.

Carter B.J., Wawrzynek, P.A., Ingraffea, A.R., 2000, Automated 3-d crack growth simulation, *International Journal for Numerical Methods in Engineering*, Volume 47 Issue 1-3, Pages 229 – 253.

Chessa, J., Smolinski, P., Belytschko, T., 2002, The extended finite element method (X-FEM) for solidification problems, *International Journal for Numerical Methods in Engineering*, Volume 53, Pages 1959-1977.

Chessa, J., Wang, H., Belytschko, T., 2003, On the construction of blending elements for local partition of unity enriched finite elements, *International Journal for Numerical Methods in Engineering*, Volume 57, Pages 1015-1038.

Cipolla, C.L., Warpinski, N.R., Mayerhofer, M.J., Lolon, E.P. and Vincent, M.C., 2008, The Relationship Between Fracture Complexity, Reservoir Properties, and Fracture Treatment Design, SPE 115769.

Cleary, M., Wong, S., 1985, Numerical simulation of unsteady fluid flow and propagation of a circular hydraulic fracture, *International Journal of Numerical and Analytical Methods in Geomechanics*, vol. 9, issue 1, pp. 1-14.

Cleary, M.P., 1994, Critical issues in hydraulic fracturing of high-permeability reservoirs, In: *Proceedings of Soc. Petr. Eng. European Production Operations Conference and Exhibition, Aberdeen, Scotland*, pp. 223–238.

Cleary, M.P., Wright, C.A. and Wright, T.B., 1991, Experimental and modeling evidence for major changes in hydraulic fracturing design and field procedures, In: *Proceedings Soc. Petr. Eng. Gas Technology Symposium, Houston, TX*, pp. 131–146.

Cook, J., Gordon, J.E., 1964, A mechanism for the control of crack propagation in all brittle systems, *Proceedings of the Royal Society of London* 282A, 508–520.

Cotterell, B., Rice, J.R., 1980, Slightly curved or kinked cracks, *International Journal of Fracture*, Volume 16, Pages 155-169.

Crittendon, B.C., 1959, The mechanics of design and interpretation of hydraulic fracture treatments, *Journal of Petroleum Technology,* (October), pages: 21–9.

182

Currie, I.G., 2003, *Fundamental mechanics of fluids*, third edition, McGraw-Hill, New York.

Curtin, W.A. and H. Scher, 1990, Mechanics modeling using a spring network, Journal of Materials Research; 5(3):554 –562.

Daneshy, A.A., 1973, On the design of vertical hydraulic fractures, *Journal of Petroleum Technology*, (January), pages: 83–97, *SPE* 3654.

Daneshy, A.A., 1974, Hydraulic fracture propagation in the presence of planes of weakness, *SPE* 4852.

Daveies, D.H., Faivre, O., Gounot, M.T., Trouiller, J.C., Benimeli, D.F.A., Pittman, D.J., Smitts, J.W., Lovell, J., Azimuthal Resistivity Imaging: A New-Generation Laterolog, *SPE* 24676.

Daux, C., Moës, N., Dolbow, J., Sukumar, N. and T. Belytschko, 2000, Arbitrary branched and intersecting cracks with the extended finite element method, *International Journal for Numerical Methods in Engineering*, Volume 48, Pages 1741-60.

Delaney, P.T., Pollard, D.D., 1981, Deformation of host rocks and flow of magma during growth of minette dikes and breccia-bearing intrusions near Ship Rock, NM. USGS Professional Paper 1202, p. 1 – 13.

Delaney, P.T., Pollard, D.D., Ziony, J.I. and E. H. McKee, 1986, Field relations between Dikes and Joints: Emplacement processes and Paleostress analysis, *Journal of Geophysical Research*, 91(B5), 4920–4938.

De Pater, C.J. and L.J.L. Beugelsdijk, 2005, Experiments and numerical simulation of hydraulic fracturing in naturally fractured rock, ARMA/USRMS 05-780.

Detournay, E., Cheng, A.H., McLennan, J.D., 1990, A Poroelastic PKN Hydraulic Fracture Model Based on an Explicit Moving Mesh Algorithm, *Journal of Energy Resources Technology*, Vol. 112 (4), pp. 224-230.

Desroches, J., Thiercelin, M., 1993, Modeling propagation and closure of micro-hydraulic fracturing, *International Journal of Rock Mechanics and Mining Sciences,* 30: 1231–4.

Desroches J, Detournay E, Lenoach B, Papanastasiou P, Pearson, JRA, Thiercelin M, 1994, The crack tip region in hydraulic fracturing. Proc R Soc London A 1994;447:39–48.

Detournay, E., Garagash, D., 2003, The tip region of a fluid-driven fracture in a permeable elastic solid, *Journal of Fluid Mechanics*, 494:1–32.

Detournay, E., 2004, Propagation regimes of fluid-driven fractures in impermeable rocks, *International Journal of Geomechanics*, 4:1–11.

Dolbow, J., Moës, N., Belytschko, T., 2000, Modelling fracture in Mindlin-Reissner plates with the extended finite element method, *International Journal of Solids and Structures*, Volume 37, Pages 7161-83.

Dolbow, J.E., Devan, A., 2004, Enrichment of enhanced assumed strain approximations for representing strong discontinuities: addressing volumetric incompressibility and the discontinuous patch test, *International Journal for Numerical Methods in Engineering*, Volume 59, Pages 47-67.

Duarte, C.A., Babuška, I., Oden, J.T., 2000, Generalized finite element methods for three dimensional structural mechanics problems, *Computers and Structures*, Volume 77, Pages 215-32.

Duarte, C.A., Hamzeh, O.N., Liszka, T.J. and Tworzydlo, W.W., 2001, A generalized finite element method for the simulation of three-dimensional dynamic crack propagation, *Computer Methods in Applied Mechanics and Engineering*, Volume 190, Pages 2227-62.

Erdogan, F. and Sih, G.C., 1963, On the crack extension in plates under loading and transverse shear*, Journal of Basic Engineering* 85, 519-527.

Fineberg J. and Marder, M., 1999, Instability in dynamic fracture, *Physics Reports*, vol. 313, pp. 1-108.

Fleming, M., Chu, Y.A., Moran, B., Belytschko, T., 1997, Enriched element-free Galerkin methods for crack tip fields, *International journal for numerical methods in engineering* 40:88, 1483-1504.

Freund, L.B., 1990, Dynamic fracture mechanics, Cambridge University Press.

Freund, L.B., Suresh, S., 2003, Thin Film Materials: Stress, Defect Formation, and Surface Evolution, Cambridge University Press.

Gale, J.F.W., Laubach, S. E., Marrett, R.A., Olson, J. E., Holder, J. and R.M. Reed, 2004, Predicting and characterizing fractures in dolostone reservoirs: using the link between diagenesis and fracturing. In: Braithwaite, C.J.R., Rizzi, G. and Darke, G., The Geometry

and Petrogenesis of Dolomite Hydrocarbon Reservoirs. Geological Society, London, Special Publications, 235, Pages 177-192.

Gale, J.F.W., Reed, R.M. and Holder, J., 2007, Natural fractures in the Barnett Shale and their importance for hydraulic fracture treatments, *AAPG Bulletin*; v. 91; no. 4; p. 603-622.

Gale, J. F., and Holder, Jon, 2008, Natural fractures in shales: origins, characteristics and relevance for hydraulic fracture treatments, *AAPG 2008 Annual Convention and Exhibition* Abstracts Volume, v. 17, p. 63.

Geertsma, J., de Klerk, F., 1969, A rapid method of predicting width and extent of hydraulically induced fractures, *Journal of Petroleum Technology,* Vol. 21, pages: 1571–81 [SPE 2458].

Geertsma, J. and Haafkens, R., 1979, A comparison of the theories for predicting width and extent of vertical hydraulically induced fractures, *Journal of Energy research and technology* Vol. 101, pages: 8-19.

Geyer, J.F. and S. Nemat-Nasser, 1982, Experimental investigation of thermally induced cracks in brittle solids, *International Journal of Solids and Structures*, Vol. 18, pages 349-356.

Gonzalez, O., Stuart, A.M., 2008, A first course in continuum mechanics, Cambridge University Press.

Gracie, R., Ventura, G., and Belytschko, T., 2007, A new fast method for dislocations based on interior discontinuities, *International Journal for Numerical Methods in Engineering*, Volume 69, Pages 423-441.

Gracie, R., Wang, H.W. and T. Belytschko, 2008, Blending in the eXtended Finite Element Method by Discontinuous Galerkin and Assumed Strain Methods, *International Journal for Numerical Methods in Engineering*, 74(11), page 1645-1669.

Grebe, J.J. and Stoesser, M., 1935, Increasing crude production 20,000,000 bbl. from established fields, *World Petroleum J*, (August), pages: 473–82.

Griffith, A.A., 1921, The phenomena of rupture and flow in solids, *Phil. Trans. R. Soc. A,* 221, pages 163–198.

Hainey, B.W., R.G. Keck, M.B. Smith, K.W. Lynch, and J.W. Barth, 1999, On-site fracturing disposal of oilfield-waste solids in Wilmington field, California, *SPE PRODUCTION & FACILITIES*, Volume *14*, pages: 88-93.

Hallam, S.D. and Last, N.C., 1991, Geometry of hydraulic fractures from modestly deviated wellbores, *Journal of Petroleum Technology*, volume *43*, pages: 742-748.

Harrison, E., Kieschnick, W.F., McGuire, W.J., 1954, The mechanics of fracture induction and extension, *Petroleum Trans AIME*, Vol. 201 pages: 252–63.

Hayashi, K., A. Sato, and T. Ito, 1997, In situ stress measurements by hydraulic fracturing for a rock mass with many planes of weakness, *International Journal of Rock Mechanics & Mining Sciences*, *34*, pages: 45-58.

He, M.Y. and J.W. Hutchinson, 1989, Crack Deflection at an Interface Between Dissimilar Elastic Materials, *International journal of solids and structures* Volume 25, No. 9, 1053-1067.

Hill, R. E., 1992, Analysis of natural fractures in the Barnett Shale, Mitchell Energy Corporation T. P. Sims no. 2, Wise County, Texas: Topical report, GRI-92/0094, February 1992, Chicago, Illinois, Gas Research Institute, 50 p.

Hopkins, C.W., Frantz, J.H., Hill, D.G. and F. Zamora, 1995, Estimating fracture geometry in the naturally fractured Antrim Shale, SPE 30483.

Hopkins, C.W., Rosen, R.L., and D.G. Hill, 1998, Characterization of an induced hydraulic fracture completion in a naturally fractured Antrim shale reservoir: Paper 51068 *SPE*, Eastern Regional Mtg., Pittsburgh, Pennsylvania.

Hsia, K. J. and Xu, Z., 1996, The mathematical framework and an approximate solution of surface crack propagation under hydraulic pressure loading, *International Journal of Fracture* 78, pages 363-378.

Huang , P.Y. and Joseph, D.D., 2000, Effects of shear thinning on migration of neutrally buoyant particles in pressure driven flow of Newtonian and viscoelastic fluids, *Journal of Non-Newtonian Fluid Mechanics*, 90, pp 159–185.

Huang, R., Prevost, J.H., and Z. Suo, 2002, Loss of constraint on fracture in thin film structures due to creep, *Acta Materialia*, Volume 50, Pages 4137-4148.

Huang, R., Sukumar, N. and Prevost, J.H., 2003, Modeling quasi-static crack growth with the extended finite element method -Part II: Numerical Applications, *International Journal of Solids and Structures*, Volume 40, Pages 7539-7552.

186

Huang, R., Prevost, J.H., Huang, Z.Y. and Z. Suo, 2003, Channel-cracking of thin films with the extended finite element method, *Engineering Fracture Mechanics* 70, 2513-2526.

Hubbert, M.K., Willis, D.G., 1957, Mechanics of hydraulic fracturing, *Journal of Petroleum Technology*, 9(6), pages: 153–68.

Hunt, J.L., K. Frazier, Pendergraft, B.P. and Soliman, M.Y., 1994, Evaluation and 13 completion procedures for produced brine and waste-water disposal wells, *Journal of Petroleum Science and Engineering*, *11*, pages: 51-60.

Hutchinson, J.W., 1987, Crack tip shielding by micro-cracking in brittle solids, *Acta Metallurgica*, Vol. 35, No. 7, pp. 1605-1619.

Jeffrey, R.G., Vandamme, L. and J.C. Roegiers, 1987, Mechanical Interactions in Branched or Subparallel Hydraulic Fractures, SPE 16422.

Jeffrey, R.G., Settari, A., Smith, N.P., 1995, A comparison of hydraulic fracture field experiments, including mineback geometry data, with numerical fracture model simulations. In: Proceedings of the Society of Petroleum Engineers Annual Technical Conference and Exhibition, Dallas, 1995. pages: 591–606.

Jiang, T., Zhang, Y., Wang, Y., Ding, Y., Luo, N., Xu, Z. and Feng, X., 2006, The Study and Field Applications of Hydraulic Fracturing Technology In Clay-Carbonate Reservoirs With High Temperature, Deep Well Depth and densely distributed Natural Fractures, SPE99387.

Jin, Z.H. and Johnson, S.E., 2008, Primary oil migration through buoyancy-driven multiple fracture propagation: oil velocity and flux, *Geophysical Research Letters*, Vol. 35, L09303.

Johnson, R.L., Dunn, K.P., Hopkins, C.W., Conway, M.W., The Pressure-Dependence Ratio: A Bottomhole Treating Pressure Diagnostic Tool for Hydraulic Fracturing Treatments in Tight, Naturally Fractured Reservoirs, paper *SPE* 51364, presented at the 1998 Annual Technical Conference and Exhibition, New Orleans, LO, Sept. 27-30.

Khristianovic S.A., Zheltov, Y.P., 1955, Formation of vertical fractures by means of highly viscous liquid. In: *Proceedings of the fourth world petroleum congress*, Rome, pages: 579–86.

Lacazette, A., and T. Engelder, 1992, Fluid-driven cyclic propagation of a joint in the Ithaca siltstone, Appalachian Basin, New York, in *Fluid Mechanics and Transport*

Properties of Rocks, B. Evans and T-F. Wong eds, Academic Press Ltd., London, pages: 297-324.

Lam, K.Y. and M.P. Cleary, 1984, Slippage and re-initiation of (hydraulic) fractures at frictional interfaces, International Journal for Numerical and Analytical Methods in Geomechanics, Vol. 8, 589-604.

Lamont, N. and Jessen, F., 1963, The effects of existing fractures in rocks on the extension of hydraulic fractures, *Journal of Petroleum Technology,* February (1963), pages: 203–209.

Lancaster, D.E., McKetta, S.F., Hill, R.E., Guidry, F.K., Jochen, J.E., 1992, Reservoir Evaluation, Completion Techniques, and Recent Results From Barnett Shale Development in the Fort Worth Basin, *SPE* 24884-MS.

Laubach, S., Marrett, R., and Olson, J., 2000, New directions in fracture characterization, *The Leading Edge*, pages 704-711.

Laubach, S. E., 2003, Practical approaches to identifying sealed and open fractures, *AAPG Bulletin*, April 2003, v. 87, no. 4, p. 561-579.

Laubach, S. E., Olson, J. E., and Gale, J., 2004, Are open fractures necessarily aligned with maximum horizontal stress?, *Earth & Planetary Science Letters*, v. 222 (1), p. 191-195.

Lawn, B., Fracture of Brittle Solids, Cambridge University Press, 2004.

Leguillon, D., Lacroix, C., Martin, E., 2000, Interface debonding ahead of a primary crack, *Journal of the Mechanics and Physics of Solids,* 48, 2137–2161.

Liao, X., Wang, L.Q. and Yu, P., 2007, Stability of Dynamical Systems, Volume 5 (Monograph Series on Nonlinear Science and Complexity)**,** Elsevier Science.

Li, Y., Cheng, C.H., Toksöz, M.N., 1998, Seismic monitoring of the growth of a hydraulic fracture zone at Fenton Hill, New Mexico, *Geophysics*, Volume 63, Issue 1, pp. 120-131.

Li, J., 2004, Debonding of the interface as 'crack arrestor', International Journal of Fracture, Volume 105, Issue 1, pp. 57-79.

Lenoach B., 1995, The crack tip solution for hydraulic fracturing in a permeable solid, *Journal of Mechanics of Physics and Solids*, 43(7):1025–43.

Loucks, R. G., and S.C. Ruppel, 2007, Mississippian Barnett Shale: Lithofacies and depositional setting of a deep-water shale-gas succession in the Forth Worth Basin, Texas: *AAPG Bulletin*, Vol. 91, No. 4, pages 579–601.

Majumdar, B.S., Gundel, D.B., Dutton, R.E., Warrier, S.G., Pagano, N.J., 1998, Evaluation of the tensile interface strength in brittle matrix composite systems, *Journal of the American Ceramic Society*, Vol. 81, pages 1600–1610.

Martin, E., Leguillon, D., 2004, Energetic conditions for interfacial failure in the vicinity of a matrix crack in brittle matrix composites, International Journal of Solids and Structures 41 (2004) 6937–6948.

Martha, L.F., P.A. Wawrzynek and A.R. Ingraffea, 1993, Arbitrary crack representation using solid modeling. *Eng. Comp.* 9, pages 63–82.

Melenk J.M. and I. Babuška, 1996, The partition of unity finite element method: Basic theory and applications, *Computer Methods in Applied Mechanics and Engineering*, Volume 139, Issues 1-4, Pages 289-314.

Moës, N., Dolbow, J. and T. Belytschko, 1999, A finite element method for crack growth without remeshing, *International Journal for Numerical Methods in Engineering*, Volume 46, Pages 131-150.

Moës, N., Belytschko, T., 2002, Extended finite element method for cohesive crack growth, *Engineering Fracture Mechanics*, Volume 69, Pages 813-33.

Moës, N., Gravouil, A., and Belytschko, T., 2002, Non-planar 3D crack growth by the extended finite element and level sets-Part I: Mechanical model, *International Journal for Numerical Methods in Engineering*, Volume 53, Pages 2549-2568.

Moës, N., Béchet, E., Tourbier, M., 2006, Imposing essential boundary conditions in the extended finite element method, *International Journal for Numerical Methods in Engineering*, Volume 67 (12), Pages 1641–1669.

Montgomery, S. L., D.M. Jarvie, K. A. Bowker, and R. M. Pollastro, 2005, Mississippian Barnett Shale, Fort Worth Basin, northcentral Texas: Gas-shale play with multi–trillion cubic foot potential: *AAPG Bulletin*, v. 89, pages 155–175.

Murdoch, L.C., and W.W. Slack, 2002, Forms of hydraulic fractures in shallow fine grained formations, *Journal of Geotechnical and Geoenvironmental Engineering, 128*, pages: 479-487.

Murphy, H.D. and Fehler, M.C., 1986, Hydraulic fracturing of jointed formations, *SPE* 14088.

Nilson, R.H., 1981, Gas driven fracture propagation, *ASME Journal of Applied Mechanics* 48, pp. 757–762.

Nilson, R.H. and Griffiths, S.K., 1986, Similarity analysis of energy transport in gas-driven fractures, *International Journal of Fracture,* Vol. 30, pages: 115-134.

Nilson, R.H., 1988, Similarity solutions for wedge-shaped hydraulic fracture driven into a permeable medium by a constant inlet pressure, *International Journal for Numerical and Analytical Methods in Geomechanics* 12, pages 477–495.

Nolte, K. G. and M.B. Smith, 1979, Interpretation of fracturing pressure, *SPE* 8297.

Nolte, K.G., 1987, Discussion of influence of geologic discontinuities on hydraulic fracture propagation, *Journal of. Petroleum Technology*, page 998.

Nordgren, R.P., 1972, Propagation of a vertical hydraulic fracture, *SPE Journal*, 12(8), pages: 306–14, *SPE* 7834.

Nuismer, R., 1975, An energy release rate criterion for mixed mode fracture, *International Journal of Fracture* 11, pages 245-250.

Olson, J.E. and D.D. Pollard, 1991, The initiation and growth of en echelon veins, *Journal of Structural Geology*, Vol. 13, No. 5, pages 595-608.

Olson, J.E., 1993, Joint pattern development: effect of subcritical crack growth and mechanical crack interaction, *Journal of geophysical research*, 98, pages: 12251-12265.

Olson, J.E., 1995, Fracturing from highly deviated and horizontal wells: numerical analysis of non-planar fracture propagation, *SPE* 29573.

Olson, Jon E., 2003, Sublinear scaling of fracture aperture versus length: an exception or the rule?, *Journal of Geophysical Research*, v. 108(B9), Art. No. 2413.

Olson, J.E., 2004, Predicting fracture swarms – the influence of subcritical crack growth and the crack-tip process zone on joint spacing in rocks, in" initiation, propagation and arrest of joints and other fractures", Geological society of London Special publication 231, pages: 73-87.

Olson, J. E., Laubach, S. E. and Lander, R. H., 2006, Combining diagenesis and mechanics to quantify fracture aperture distributions and fracture pattern permeability, In:

Fractured Reservoirs (edited by Lonergan, L., Rawnsley, K. and Sanderson, D. J.). Geological Society of London, Special Publications.

Palmer, I.D., Fryar, R.T., Tumino, K.A., Puri, R., 1991, Comparison between Gel-Fracture and Water-Fracture Stimulations in Black Warrior Basin, *SPE* 23415.

Palmer, I.D., 1993, Induced Stresses Due to Propped Hydraulic Fracture in Coalbed Methane Wells, *SPE* 25861.

Patzák B, Jirásek M., 2004, Adaptive resolution of localized damage in quasi-brittle materials. *Journal of Engineering Mechanics*; 130:720–732.

Perkins, T.K., Kern, L.R., 1961, Widths of hydraulic fractures, *Journal of Petroleum Technology*, 13(9), pages: 937–49 [*SPE* 89].

Pollard, D.D., Muller, O.H. and Dockstader, D.R., 1975, The form and growth of fingered sheet intrusions, *Geological Society of America Bulletin*, 86, pages: 351-363.

Pollard, D.D., 1981, Elementary fracture mechanics applied to the structural interpretation of dykes; in Mafic dyke swarms, Editors: Halls, H.C. and Fahrig, W.F., Geological Association of Canada Special Paper 34, p. 5-24.

Pollard, D.D., Segall, P. and P.T. Delaney, 1982, Formation and interpretation of dilatant echelon cracks, *Geological Society of America Bulletin*, Dec 1982; 93: 1291-1303.

Pollard, D.D., 1987, Elementary fracture mechanics applied to the structural interpretation of dykes, in *Mafic Dyke Swarms*, edited by H.C. Halls and W.F. Fahrig, *Geological Association of Canada Special Paper 34*, pages: 5-24.

Pollard, D.D., and A. Aydin, 1988, Progress in understanding jointing over the past century, *Geological Society of America Bulletin*, 100, pages: 1181-1204.

Pereira, J.P. and C.A. Duarte ,2006, The contour integral method for loaded cracks, *Communications in numerical methods in engineering*, Vol. 22, page 421-432.

Raaen, A.M., Skomedal, E., Kjorholt, H., Markestad, P. and Okland, D., 2001, Stress determination from hydraulic fracturing tests: The system stiffness approach, *International Journal of Rock Mechanics and Mining Sciences*, 38, pages: 529-541.

Rethoré, J., Gravouil, A. and A. Combescure, 2005, An energy-conserving scheme for dynamic crack growth using the extended finite element method, *International Journal for Numerical Methods in Engineering*, 63, Pages 631–659.

Rice, J.R., 1968, A Path Independent Integral and the Approximate Analysis of Strain Concentration by Notches and Cracks, *Journal of Applied Mechanics*, 35, pp. 379-386.

Rodgerson, J.L., 2000, Impact of natural fractures in hydraulic fracturing of tight gas sands. SPE 59540, presented at the SPE Permian basin oil and gas recovery conference, Midland, TX, 21–23 March 2000.

Rubin, A.M., 1995, Propagation of magma-filled cracks, *Annual Review of Earth and Planetary Sciences*, 23, pages: 287–336.

Rungamornrat, J., Mear, M., and Wheeler, M. F., 2005, A Numerical Technique for Simulation Non-planar Evolution of Hydraulic Fractures, 2005 *SPE* Annual Technical Conference, Dallas, Texas, *SPE* 96968.

Rutledge, J.T. and W.S. Phillips, 2003, Hydraulic stimulation of natural fractures as revealed by induced microearthquakes, Carthage Cotton Valley gas field, east Texas, *Geophysics*, Vol. 68, NO. 2, pages 441–452.

Sasaki, S., 1998, Characteristics of microseismic events induced during hydraulic fracturing experiments at the Hijiori hot dry rock geothermal energy site, Yamagata, Japan, *Tectonophysics*, 289, pages: 171-188.

Sato, K., Wright, C.A. and Ichikawa, M., 1999, Post-Frac Analyses Indicating Multiple Fractures Created in a Volcanic Formation, *SPE Prod. & Facilities*, 14(4), *SPE* 39513.

Schoenberg, M., Sayers, C.M., 1995, Seismic anisotropy of fractured rock, *Geophysics* 60:11, 204-211

Shum, D.K.M. and J. Hutchinson, 1990, On toughening by microcracks, *Mechanics of Materials*, Vol. 9, pages 83-91.

Sih, G.C., 1974, Strain energy density factor applied to mixed mode problems, *International Journal of Fracture* 10, Pages 305-321.

Simone, A., Duarte, C.A. and Van der Giessen, E., 2006, A Generalized Finite Element Method for polycrystals with discontinuous grain boundaries, *International Journal for Numerical Methods in Engineering*, Volume 67, Pages 1122-1145.

Sinha, B.K., Vissapragada, B., Wendt, A.S., Kongslien, M. and Eser, H., Skomedal, E., Renlie, L. and Pedersen, E.S., 2007, Estimation of Formation Stresses Using Radial Variation of Three Shear Moduli—A Case Study From a High-Pressure and High-Temperature Reservoir in a Norwegian Continental Shelf, *SPE* 109842.

Sneddon, I.N., Elliot, H.A., 1946, The opening of a Griffith crack under internal pressure, Quarterly of Applied Mathematics, Volume 4, pages: 262–7.

Sousa, J.L.S., Carter, B.J. and Ingraffea, A.R., 1993, Numerical simulation of 3D hydraulic fracture using Newtonian and power-law fluids, *International Journal of Rock Mechanics and Mining Science & Geomechanics Abstracts*, Volume 30, No 7, pages: 1265-1271, presented at the 34th U.S. Rock Mechanics Symposium, Madison, Wisconsin.

Song, J.H., Areias, P.M.A., and Belytschko, T., 2006, A method for dynamic crack and shear band propagatin with phantom nodes, *International Journal for Numerical Methods in Engineering*, Volume 67, Issue6, Pages 868-893.

Spence, D. and Turcotte, D., 1985, Magma-driven propagation crack, *Journal of Geophysical Research*, Volume 90, pages 575–580.

Spence, D.A. and Sharp, P.W., 1985, Self-similar solution for elastohydrodynamic cavity flow, *Proceedings of the Royal society of London. Series A* (400), pp. 289–313.

Srivastava, D.C. and T. Engelder, 1991, Fluid evolution history of brittle-ductile shear zones on the hanging wall of Yellow Spring Thrust, Valley and Ridge Province, Pennsylvania, USA, *Tectonophysics*, 198, pages: 23-34.

Stadulis, J.M., 1995, Development of a Completion Design to Control Screenouts Caused by Multiple Near-Wellbore Fractures, SPE 29549 presented at the 1995 Rocky Mountain Regional/Low Permeability Reservoirs Symposium and Exhibition, Denver, Colorado, 20–22 March.

Stazi, F.L., Budyn, E., Chessa, J. and Belytschko, T., 2002, An extended finite element method with higher-order elements for curved cracks, *Computational Mechanics*, Volume 31, Pages 38- 48.

Stolarska, M., Chopp, D.L., Moës, N., and Belytschko, T., 2001, Modelling crack growth by level sets in the extended finite element method, *International Journal for Numerical Methods in Engineering*, Volume 51, Pages 943-960.

Strouboulis, T., Babûska, I., Copps, K., 2000, The design and analysis of the Generalized Finite Element Method, *Computer Methods in Applied Mechanics and Engineering*, Volume 181, Pages 43-69.

Strouboulis, T., Copps, K., Babûska, I., 2001, The generalized finite element method, *Computer Methods in Applied Mechanics and Engineering*, Volume 190, Pages 4081-4193.

Sukumar, N., Chopp, D.L., Moës, N., and Belytschko, T., 2001, Modeling holes and inclusions by level sets in the extended Finite-element method, *Computer Methods in Applied Mechanics and Engineering*, Volume 190, Pages 6183-6200.

Sukumar, N., Moës, N., Moran, B. and Belytschko, T., 2000, Extended finite element method for three-dimensional crack modeling, *International Journal for Numerical Methods in Engineering*, Volume 48, Pages 1549-1570.

Szabó, B.A. and I. Babuška, Finite Element Analysis, John Wiley and Sons, New York, 1991.

Valkó, P. and M.J. Economides, 1995**,** Hydraulic Fracture Mechanics, Wiley.

Van Batendburg, D.W., Hellman, T.J., 2002, Guidelines for the Design of Fracturing Treatments for Naturally Fractured Formations, SPE 78320.

Van Dyke, M., 1983, Laminar Flow in a Meandering Channel, *SIAM Journal on Applied Mathematics*, Vol. 43, No. 4 (Aug., 1983), pp. 696-702

Veatch, R.W., Moschovidis, Z.A., Fast, C.R., 1989, An overview of hydraulic fracturing. In: Gidley, Holditch, Nierode, Veatch, editors. Recent advances in hydraulic fracturing. Monograph, Vol. 12, Richardson: Society of Petroleum Engineers, p. 1–38.

Ventura, G., Moran, B., and Belytschko, T., 2005, Dislocations by partition of unity, *International Journal for Numerical Methods in Engineering*, Volume 62, Issue 11, Pages 1463-1487.

Walsh, J.B., 1981, Effect of pore pressure and confining pressure on fracture permeability, *International Journal of Rock Mechanics, Mining sciences and Geomechanics* 18, pp 429-35.

Wang, C.Y., 1980, Flow in narrow curved channels, *Journal of Applied Mechanics*, 47, 7-10.

Warpinski, N.R., Schmidt, R.A., Northrop, D.A., 1982, In-Situ Stresses: The Predominant Influence on Hydraulic Fracture Containment, *Journal of Petroleum Technology*, Vol. 34 Issue 3.

Warpinski, N.R., Clark J.A., Schmidt R.A., CW Huddle, 1982, Laboratory investigation on the effect of in-situ stresses on hydraulic fracture containment, *SPE Journal*, Soc. Pet. Eng. J., Vol. 22, Issue 3.

Warpinski, N.R. and Teufel, L.W., 1987, Influence of geologic discontinuities on hydraulic fracture propagation, *Journal of Petroleum Technology*, page: 209–220.

Warpinski, N.R., 1990, Dual leakoff behavior in hydraulic fracturing of tight lenticular gas sands, *SPE* 18259.

Warpinski, N.R., 1991, Hydraulic fracturing in tight, fissured media, *Journal of Petroleum Technology*, pages: 146-209.

Warpinski, N.R., Lorenz, J.C., Branagan, P.T., Myal, F.R., Gall, B.L., 1993, Examination of a Cored Hydraulic Fracture in a Deep Gas Well, SPE 22876.

Warpinski, N. R., R. C. Kramm, J. R. Heinze, and C. K. Waltman, 2005, Comparison of single- and dual array microseismic mapping techniques in the Barnett Shale, Proceedings of Society of Petroleum Engineers Annual Technical Conference, Dallas, Texas, SPE Paper 95568, 10 p.

Waters, G., Heinze, J., Jackson, R., Ketter, A., Daniels, J. and D. Bentley, 2006, Use of Horizontal Well Image Tools to Optimize Barnett Shale Reservoir Exploitation, *SPE* 103202, presented at the SPE Annual Technical Conference.

Weertman, J., 1971, Theory of Water-Filled Crevasses in Glaciers Applied to Vertical Magma Transport beneath Oceanic Ridge, *Journal of Geophysical Research*, vol. 76, issue 5, pp. 1171-1183.

Weertman, J., 1984, Crack tip stress intensity factor of the double slip plane crack model: shortcracks and short short-cracks, *International Journal of Fracture*, 26 pages 31-42.

Weijers, L., 1995, The near-wellbore geometry of hydraulic fractures initiated from horizontal and deviated wells, Ph.D. Dissertation, Delft University of Technology.

Yew, C.H., Liu, G.F., 1993, Fracture tip and critical stress intensity factor of a hydraulically induced fracture, *SPE Production and Facilities*, Vol./Issue: 8:3 Pages: 171-177.

Yew, C.H., 1997, *Mechanics of hydraulic fracturing*, Gulf Publishing Company, Houston, Texas.

Zhang, X., Sanderson, D.J., 2002, Numerical modeling and analysis of fluid flow and deformation of fractured rock masses, Pergamon press.

Zhang, X., Jeffrey, R.G. and M. Thiercelin, 2007, Deflection and propagation of fluid-driven fractures at frictional bedding interfaces: A numerical investigation, *Journal of Structural Geology* Vol. 29, pages 396-410.

Zimmerman, M.N., 2005, Host rock fracture analysis: applying the deformation mechanics associated with shallow igneous intrusion to the fracture bridging theory, Master thesis, Texas Tech University.

VITA

Arash Dahi Taleghani attended Danesh High School, Tehran, Iran. In 1997, he entered the Civil Engineering program of the Sharif University of Technology, Tehran, Iran. He got his Bachelor of Science in 2001. After that he was admitted to the graduate program in Structural Mechanics and Materials in Civil Engineering department of the Sharif University of Technology, where he got his Master of Science in October 2003. His master thesis was on the multi-scale simulation of dynamic crack propagation in heterogeneous materials. In summer 2004, he entered the PhD program of the Department of Petroleum and Geosystems Engineering of the University of Texas at Austin. During the summers 2006 and 2007, he was an intern at the Geomechanics group of Schlumberger studying the reservoir compaction and the seismic responses of the cemented fractures.

Permanent Address: 150 Africa Ave., Tehran, Iran 19177

This manuscript was typed by the author.